SATELLITE MAPPING AND AUTOMATED FEATURE EXTRACTION: GEOGRAPHIC INFORMATION SYSTEM-BASED CHANGE DETECTION OF THE ANTARCTIC COAST

DISSERTATION

Presented in Partial Fulfillment of the Requirement for

The Degree Doctor of Philosophy in the

Graduate School of The Ohio State University

By

Kee-Tae Kim, B.S., M.S.

* * * * *

The Ohio State University

2004

Dissertation Committee:

Dr. Rongxing Li, Adviser

Dr. Kenneth C. Jezek

Dr. Alan J. Saalfeld

Approved by:

____

Adviser

Graduate Program in Geodetic Science and Surveying

ABSTRACT

Declassified Intelligence Satellite Photograph (DISP) data are important resources for measuring the geometry of the coastline of Antarctica. By using the state-of-art digital imaging technology, bundle block triangulation based on tie points and control points derived from a RADARSAT-1 Synthetic Aperture Radar (SAR) image mosaic and Ohio State University (OSU) Antarctic digital elevation model (DEM), the individual DISP images were accurately assembled into a map quality mosaic of Antarctica as it appeared in 1963. The new map is one of important benchmarks for gauging the response of the Antarctic coastline to changing climate.

Automated coastline extraction algorithm design is the second theme of this dissertation. At the pre-processing stage, an adaptive neighborhood filtering was used to remove the film-grain noise while preserving edge features. At the segmentation stage, an adaptive Bayesian approach to image segmentation was used to split the DISP imagery into its homogenous regions, in which the fuzzy c-means clustering (FCM) technique and Gibbs random field (GRF) model were introduced to estimate the conditional and prior probability density functions. A Gaussian mixture model was used to estimate the reliable initial values for the FCM technique. At the post-processing stage, image object formation and labeling, removal of noisy image objects, and vectorization algorithms were sequentially applied to segmented images for extracting a vector representation of coastlines. Results were presented that demonstrate the effectiveness of the algorithm in segmenting the DISP data. In the cases of cloud cover and little contrast scenes, manual editing was carried out based on intermediate image processing and visual inspection in comparison of old paper maps.

Through a geographic information system (GIS), the derived DISP coastline data were integrated with earlier and later data to assess continental scale changes in the Antarctic coast. Computing the area of major Antarctic ice shelves between 1963 and 1997, we found that the net loss was approximately 0.8% and ice shelves retreated mostly between DISP and Scientific Committee Antarctic Research (SCAR) Antarctic Digital Database (ADD). In addition, over the 56-years (1947-present) observations on Pine Island Glacier, we found that the retreat rate has been approximately -10 ± 65 m/yr.

Dedicated to my parents

ACKNOWLEDGEMENTS

I would like to express my sincere thanks to Dr. Rongxing Li and Dr. Kenneth C. Jezek for their help and support during this study; Dr. Alan J. Saalfeld for his participation as a committee member; and my colleagues in the Remote Sensing Lab at the Byrd Polar Research Center for their friendship and cheers during my research work.

Thanks are also due to my friends who have strived to entertain ideas of our study and research over the years.

I would also like to express my deepest thanks to my wife, Dr. Eun-Kyoung Yang for taking care of our precious daughter, Cherri and her support and love without which this study could never have been completed.

Finally, I am deeply indebted to my parents, who through their efforts and dedication instilled in me a respect for learning without which I would never have reached Columbus.

VITA

July, 1964	Born – Seoul, Korea
1993	B.S., Civil Engineering, Dankook University, Seoul, Korea
1996	M.S., Civil Engineering, Yonsei University, Seoul, Korea
1999	Graduate Research Associate, M.S., Geodetic Science and Surveying, The Ohio State University, Columbus, USA
1999–Present	Graduate Research Associate, The Ohio State University, Columbus, USA

PUBLICATIONS

Sohn, H., G. Kim, and K. Kim, 2002, Change detection study of Seoul using CORONA project, KSCE, 22(4-D): 757-765.

Kim, K., K. C. Jezek, and H. Sohn, 2001, Ice shelf advance and retreat rates along the coast of Queen Maud Land, Antarctica, J. Geophysical Research, 106(C4): 7097-7106.

Sohn, H. and K. Kim, 2000, Horizontal positional accuracy assessment of historical ARGON satellite photography, KSCE, 4:59-65.

Kim, K., 1999, Application of time series satellite data to Earth science problems, M.S. Thesis, The Ohio State University, Columbus, 69 pp.

FIELDS OF STUDY

Major Field: Geodetic Science and Surveying

Remote Sensing & Geographic Information Systems

Image Analysis and Pattern Recognition

Geospatial Data Analysis

TABLE OF CONTENTS

LIST OF FIGURES

LIST OF TABLES

CHAPTER 1

INTRODUCTION

1.1 General Overview

Remote sensing acquires information about an object without physical contact (Rencz and Ryerson, 1998). Information about Earth's surface can be recorded on aerial or space photography, or satellite digital imagery. Aerial and space photography records an image on photographic emulsions that are sensitive to energy in or near the visible portion of the electromagnetic spectrum. Satellite digital imagery records an image over a broad range of the electromagnetic spectrum.

The role played by this remote sensing technology in the systematic monitoring of polar ice sheet characteristics, which is essential in the early detection of global warming trends, is very important. More than 70% of Earth's fresh water is bound up in the Antarctic ice sheet; if it all melted, global sea level would rise some 73 meters (Williams, Jr. et al., 1995).

Antarctica has remained one of the most poorly mapped parts of our planet because it is the coldest, windiest and on average, highest of all continents. Since the early 1970s remotely sensed data have provided an opportunity for scientists to overcome some environmental obstacles of Antarctica and conduct large scale analysis of the

Antarctic coastal regions. An extensive archive of early 1970s LANDSAT 1, 2 and 3 Multi-Spectral Scanner (MSS) images was the first impetus to map the Antarctic from space (Swithinbank, 1973; Swithinbank and Lucchita, 1986). The maps were later modified to include analysis of coastal change using the late 1980s and early 1990s LANDSAT 4 and 5 MSS and Thematic Mapper (TM) images and 1992 and 1995 European Space Agency's Earth Remote-Sensing Satellite radar images (Williams, Jr., 1995). In 1997, RADARSAT-1 Synthetic Aperture Radar (SAR) data were successfully acquired over the entirety of Antarctica by the Canadian Space Agency's RADARSAT mission, which National Aeronautics and Space Administration (NASA) launched in November 1995. The coverage is complete and has been used to create the first, high-resolution (25-m), radar image mosaic of Antarctica (Jezek, 1999).

Antarctic scientists were restricted to airborne data as a source for high-resolution broad-scale coverage for the era preceding LANDSAT. Now more extensive coverage at high-resolution has become available through declassification of early satellite reconnaissance photographs (McDonald, 1995; Wheelon, 1997; and Peebles, 1997) known as Declassified Intelligence Satellite Photographs (DISP), which were taken by a series of reconnaissance satellites called Corona, Lanyard, and Argon, launched in the early 1960s in polar orbits to monitor Soviet military activities. While the northern hemisphere was their primary target, the opportunity was also taken to obtain images of Antarctica.

This study includes orthorectification and mosaicking of the Argon DISP data along the entire coast of Antarctica, extraction of the Antarctic coastline, and comparison of the extracted coastline and more recent coastline data. The results were used for investigating whether the entirety of the Antarctic coastline is behaving in a manner consistent with global warming.

1.2 Thesis Overview

Chapter 2 explains data sets used in this study. 1963 Argon DISP photographs, 1997 RADARSAT-1 SAR image mosaic (Jezek, 1999), and Ohio State University Antarctic digital elevation model (DEM) (Liu et al., 1999) were used to create a seamless, complete image mosaic of Antarctic coastal regions in order to identify and analyze changes in the Antarctic coastlines in comparison of the Scott Committee on Antarctic Research (SCAR) Antarctic Digital Database (ADD) coastline (1968 - 1991) (ADD Consortium, 2000) and 1997 RADARSAT-1 SAR coastline data (Liu and Jezek, 2003) over the past three decades.

Chapter 3 presents the second large body of study concerning orthorectification and mosaicking of Argon DISP data. Bundle block triangulation and orthorectification using a DEM were applied to Argon DISP data, and the orthorectified images were mosaicked to create a map-quality image mosaic of the Antarctic coastal regions.

Chapter 4 describes an adaptive Bayesian approach to image segmentation. Two important elements make up a Bayesian segmentation formula, namely, the prior and conditional probability density functions. By combining these functions, a segmentation can be expressed in terms of maximum a posterior (MAP) criteria. This approach is a two-step segmentation algorithm. First, the fuzzy c-means clustering (FCM) technique (Bezdek et al., 1984) is used to model the conditional energy function $\Pr(y \mid x)$ of the observed image vectors y given the labels x based on initial values derived from the Gaussian mixture model (GMM). Second, the Gibbs random field (GRF) model is used to estimate the prior energy function $\Pr(x)$ of labels x. Using both the derived prior and conditional energy functions, the MAP estimates are established using a maximization algorithm known as maximizer of posterior marginals (MPM) (Marroquin et al., 1987).

Chapter 5 demonstrates the automated coastline extraction algorithm developed in Chapter 4. The software was applied to extract the entire coastline of Antarctica from the image mosaic produced in Chapter 3. For expediting of the processing, the image mosaic was first partitioned by a number of small image blocks (i.e., 1024×1024) along the entire coastline. Each of image blocks was then processed as described in Chapter 4. Five different types of image scenes, such as glacier and open water, light cloud cover, glacier and fast ice, mountainous coastline and mixture area, are demonstrated in this chapter. In this manner, the entire ice margin was extracted, assembled and compared with other time series data available from the literature.

In Chapter 6, through a geographic information system (GIS), the derived 1963 data were integrated with earlier and later data to assess continental scale changes in ice margin advance or retreat. Time series data presented in this chapter quantify changes in the Antarctic coastline using DISP, SCAR ADD, and SAR data. Additional Earth Observation System (EOS) data are also used in local studies of particular glaciers.

Chapter 7 concludes the thesis.

CHAPTER 2

DATA DESCRIPTIONS

1963 DISP, 1997 RADARSAT-1 SAR image mosaic, and OSU Antarctic digital elevation model (DEM) were used to produce a continuous, orthorectified DISP image mosaic of Antarctic coastal areas in order to identify and quantify changes in the Antarctic coastline in comparison of the SCAR ADD and RADARSAT-1 SAR coastline data over the past three decades.

2.1 Declassified Intelligence Satellite Photography (DISP)

2.1.1 Introduction

A few short years after the launch of the Russian Sputnik in October 1957, high-resolution spaceborne camera systems gathered photo reconnaissance imagery of the Earth surface between August 1960 and May1972 (Peebles, 1997). In February 1995, the President of the United States declassified historical intelligence photographs (DISP) from the early satellite systems known as the Corona, Argon, and Lanyard (McDonald, 1995). The addition of this early satellite reconnaissance imagery provides environmental scientists an expanded view of the world's land surface for the 12 years before the 1972 launch of Landsat. Because detecting environmental change is usually limited by the relatively short time period of available observations and by natural variability, it is expected that this DISP collection makes a significant contribution to efforts to identify and quantify global environmental change.

2.1.2 DISP: Corona, Argon, and Lanyard

Corona, Argon, and Lanyard were the first three operational imaging satellite reconnaissance systems. The Corona cameras were designated as the KH-1, KH-2, KH-3, and KH-4 missions; the Argon camera was designated as the KH-5 mission; and the Lanyard camera was known as the KH-6 mission (McDonald, 1995). These early reconnaissance satellites carried a single panoramic camera (KH-1, 2, 3, and 6), a single frame camera (KH-5), or two panoramic cameras (KH-4, 4A, and 4B).

The KH-1 camera had a nominal ground resolution of approximately 12 meters. By 1963 improvements to the original Corona had produced the KH-2 and KH-3, with cameras that achieved resolutions of approximately 3 meters. The first KH-4 mission was launched in 1962 and brought a major development in technology by using the MURAL camera to provide stereoscopic imagery (Ruffner, 1995). This meant that two cameras photographed each target from different angles, which allowed imagery analysts to look at KH-4 stereoscopic photos in three dimensions. Three camera models with different resolutions were the principal difference between the KH-4 versions, KH-4, KH-4A, and KH-4B. By 1967, the camera of KH-4B had entered service with a resolution of approximately 1.5 meters. This final version of Corona continued until 1972.

Two other systems, separate but closely allied with Corona, also operated during this time. The Argon program performed mapping services for the Army in a few missions in the early 1960s with mediocre results.

Of three programs of Corona, Argon and Lanyard, only the Argon program collected Antarctic data between February 1961 and August 1964 (Binschadler and Seider, 1998). It flew 12 missions over time. The purpose of this system was to be a reconnaissance satellite that could obtain precise geodetic data of the Soviet Union for pinpointing strategic targets. The camera had 76.2-mm focal length and the film had resolution of 30 line-pair/mm. Every photograph has dimensions of approximately 11.43 × 11.43-cm and swath coverage of approximately 540 × 540 km. The estimated ground resolution is approximately 140-m, which is useful for a long-term change detection application of the Antarctic coast in continental scales. Camera information for Corona, Argon, and Lanyard is shown in Table 2.1.

	KH-1	KH-2	KH-3	KH-4
Function	Intelligence	Intelligence	Intelligence	Intelligence
Type	Mono Panoramic	Mono Panoramic	Mono Panoramic	Stereo Panoramic
Scan (deg)	70	70	70	70
Stereo (deg)				30
Focal Length (in)	24	24	24	24
Ground Resolution (ft)	40	25	12~25	10~25
Film Resolution (lp/mm)	50~100	50~100	50~100	50~100
Film Width (in)	2.1	2.1	2.25	2.25
Image Format (in)	2.1	2.1	2.25 × 29.8	2.18 × 29.8
Maximum Scale	Unavailable	Unavailable	Unavailable	1:12,000
	KH-4A	KH-4B	KH-5	KH-6
Function	Intelligence	Intelligence	Mapping	Surveillance
Type	Stereo Panoramic	Stereo Panoramic	Mono Frame	Mono Panoramic
Scan (deg)	70	70	Unavailable	22
Stereo (deg)	30	30		
Focal Length (in)	24	24	3	66
Ground Resolution (ft)	9~25	6	460	6
Film Resolution (lp/mm)	120	160	30	160
film Width (in)	2.25	2.25	5	5
Image Format (in)	2.18 × 29.8	2.18 × 29.8	4.5 × 4.5	4.5 × 25
Maximum Scale	1:7,500	1:7,500~1:2,000	1:1,000.000	1:3,000

Table 2.1 Camera data for Corona, Argon, and Lanyard (McDonal, 1995)

2.1.3 DISP for Antarctic Coastlines

The Antarctic continent was only captured during the Argon program between February 1961 and August 1964. During this period three missions, 9034A, 9058A, and 9059A, successfully photographed the Antarctic continent. Mission 9034A was the first effort to map the Antarctic continent. The photographs were captured during the late austral autumn (May 15 – 19, 1962), and much of the interior of the ice sheet was dark. The photographs from this mission cover the entire Antarctic coastline except for the Ross and Ronne/Filchner ice shelves, but most of the coastline was cloud covered during this period. Mission 9058A was conducted during a period when the southern interior of the ice sheet was dark (August 29 – September 1, 1963). Thus, coverage only included the coastal perimeter of the continent. Fewer revolutions were included in this mission, but most of the coast was photographed. Clouds were far less prevalent, increasing the usefulness of this photographic data to the study of the ice sheet, but the austral season was late winter and sea ice adjacent to the coast was more extensive. Mission 9059A took place in the austral spring (October 29 – November 3, 1963), when the entire continent was brightly lit by the Sun. Revolutions extended across the entire continent producing a much larger data set.

The first two missions covered only the coastal areas, while the third mission covered the entire continent. Based on visual inspection of browse images, an optimal data set of 62 Argon photographs was identified that covered the entire Antarctic coast. The outline of Antarctic continent with the location of each frame and its corresponding entity identification are shown in Figure 2.1 and Table 2.2, respectively.

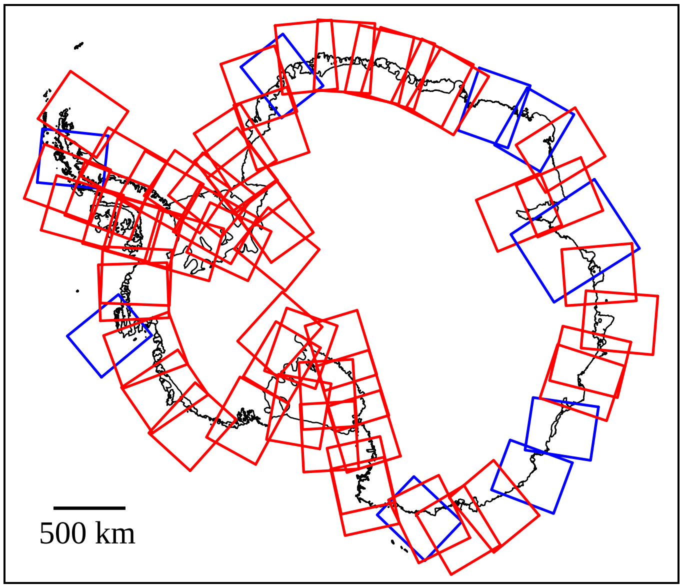

Figure 2.1 Outline of Antarctic coastlines with location of each frame: 9 Frames from the mission 9058A are in blue, and 53 frames from the mission 9059A are in red.

Entity ID	Mission Number	Revolution	Frame Number	Acquisition Date
[Mission 5098A]				
DS09058A006MC115	9058A	006M	115	8/29/1963
DS09058A009MC116	9058A	009M	116	8/29/1963
DS09058A012MC119	9058A	012M	119	8/29/1963
DS09058A014MC115	9058A	014M	115	8/29/1963
DS09058A015MC119	9058A	015M	119	8/29/1963
DS09058A016MC119	9058A	016M	119	8/29/1963
DS09058A036MC117	9058A	036M	117	8/29/1963
DS09058A041MC117	9058A	041M	117	8/29/1963
DS09058A047MC119	9058A	047M	119	8/29/1963

Continued

Table 2.2 Argon photographs providing continuous coverage of Antarctic coastline

[Mission 9059A]				
DS09059A001MC083	9059A	001M	83	10/29/1963
DS09059A003MC083	9059A	003M	83	10/29/1963
DS09059A003MC085	9059A	003M	85	10/29/1963
DS09059A003MC087	9059A	003M	87	10/29/1963
DS09059A004MC077	9059A	004M	77	10/29/1963
DS09059A006MC076	9059A	006M	76	10/29/1963
DS09059A009MC079	9059A	009M	79	10/29/1963
DS09059A010MC079	9059A	010M	79	10/29/1963
DS09059A011MC080	9059A	011M	80	10/29/1963
DS09059A011MC082	9059A	011M	82	10/29/1963
DS09059A013MC085	9059A	013M	85	10/29/1963
DS09059A014MC081	9059A	014M	81	10/29/1963
DS09059A015MC081	9059A	015M	81	10/29/1963
DS09059A023MC078	9059A	023M	78	10/29/1963
DS09059A023MC080	9059A	023M	80	10/29/1963
DS09059A029MC077	9059A	029M	77	10/29/1963
DS09059A029MC079	9059A	029M	79	10/29/1963
DS09059A030MC081	9059A	030M	81	10/29/1963
DS09059A032MC081	9059A	032M	81	10/29/1963
DS09059A032MC087	9059A	032M	87	10/29/1963
DS09059A033MC087	9059A	033M	87	10/29/1963
DS09059A034MC083	9059A	034M	83	10/29/1963
DS09059A034MC085	9059A	034M	85	10/29/1963
DS09059A035MC078	9059A	035M	78	10/29/1963
DS09059A037MC077	9059A	037M	77	10/29/1963
DS09059A038MC077	9059A	038M	77	10/29/1963
DS09059A041MC079	9059A	041M	79	10/29/1963
DS09059A042MC079	9059A	042M	79	10/29/1963
DS09059A044MC083	9059A	044M	83	10/29/1963
DS09059A044MC087	9059A	044M	87	10/29/1963
DS09059A045MC078	9059A	045M	78	10/29/1963
DS09059A045MC080	9059A	045M	80	10/29/1963
DS09059A045MC081	9059A	045M	81	10/29/1963
DS09059A045MC083	9059A	045M	83	10/29/1963

Continued

Table 2.2 Argon photographs providing continuous coverage of Antarctic coastline

DS09059A051MC077	9059A	051M	77	10/29/1963
DS09059A053MC077	9059A	053M	77	10/29/1963
DS09059A055MC077	9059A	055M	77	10/29/1963
DS09059A057MC079	9059A	057M	79	10/29/1963
DS09059A059MC082	9059A	059M	82	10/29/1963
DS09059A060MC076	9059A	060M	76	10/29/1963
DS09059A060MC082	9059A	060M	82	10/29/1963
DS09059A063MC081	9059A	063M	81	10/29/1963
DS09059A065MC084	9059A	065M	84	10/29/1963
DS09059A066MC080	9059A	066M	80	10/29/1963
DS09059A066MC081	9059A	066M	81	10/29/1963
DS09059A067MC094	9059A	067M	94	10/29/1963
DS09059A072MC079	9059A	072M	79	10/29/1963
DS09059A072MC094	9059A	072M	94	10/29/1963
DS09059A075MC083	9059A	075M	83	11/3/1963
DS09059A075MC084	9059A	075M	84	11/3/1963
DS09059A076MC079	9059A	076M	79	10/29/1963
DS09059A076MC081	9059A	076M	81	10/29/1963
DS09059A076MC084	9059A	076M	84	10/29/1963

Table 2.2 Argon photographs providing continuous coverage of Antarctic coastline

2.2 Ohio State University (OSU) Antarctic Digital Elevation Model (DEM)

Raw images digitized from the early reconnaissance photographs usually have such significant geometric distortions that they cannot be used as maps, compared with maps, or compared to each other. These distortions stem from sources such as un-calibrated camera lens distortion, atmospheric refraction, Earth curvature, and terrain relief. The orthorectification process corrects for terrain displacement and can be used if a digital elevation model of the study area exists.

The OSU Antarctic DEM was produced by integrating the best available topographic data from a variety sources (Liu et al., 1999). Though they produced three sets of continental scale DEMs with grid resolutions of 200, 400, and 1000 meters, the real resolution of the DEMs varies from place to place according to the density and scale of the original input source data. Resolutions were estimated at approximately 200 meters in the Transantarctic Mountains and Antarctic Peninsula, 400 meters in the sloped coastal regions, and 5000 meters in others. This DEM, used for terrain correcting 1997 RADARSAT-1 Synthetic Aperture Radar (SAR) imagery, was applied to the Argon imagery to eliminate effects of the relief displacement on the photographs taken over varied terrain. Figure 2.2 is a hill-shaded image derived from the OSU Antarctic DEM at a continental scale. The absolute accuracy of the DEM is estimated at approximately 35 meters for the relatively rough and steeply sloped portions of the coastal areas (Liu et al., 1999).

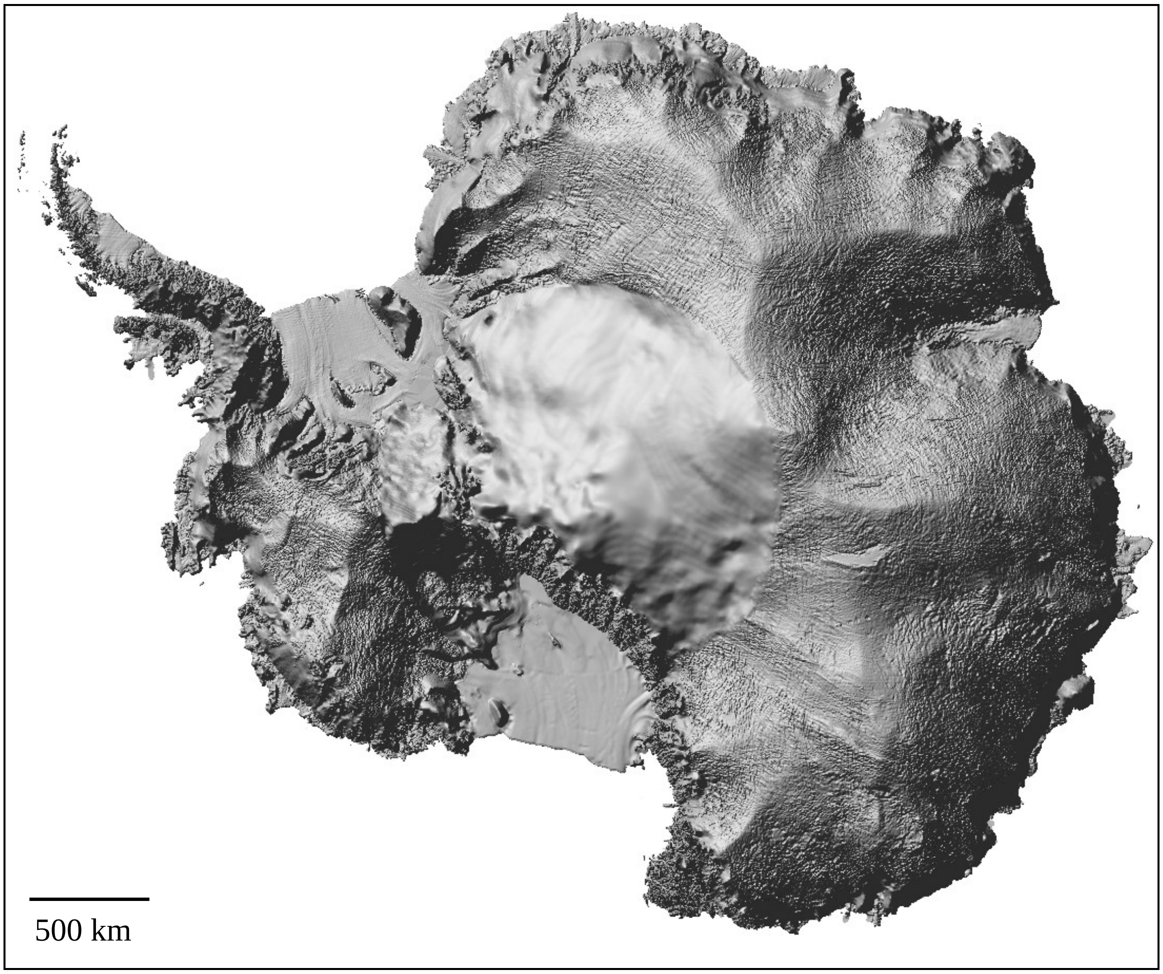

Figure 2.2 Hill-shaded image of the OSU Antarctic DEM at the continental scale

2.3 RADARSAT-1 Synthetic Aperture Radar (SAR) Mosaic of Antarctica

RADARSAT-1 SAR data were acquired over Antarctica between September 19 and October 14, 1997. The coverage is complete and has been used to construct a seamless 25-meter resolution image mosaic of Antarctica (Jezek, 1999). A 100-meter (pixel size) orthorectified mosaic displayed as a polar stereographic projection with a standard parallel of 71° S was used for identifying common features in the DISP data. The SAR data were orthorectified using the OSU Antarctic DEM. Orthorectification was further constrained by a network of ground control points obtained in cooperation with the Environmental Research Institute of Michigan and the National Imagery and Mapping Agency. The horizontal geolocation accuracy of the SAR mosaic over ice-covered terrain is estimated to be approximately 100 meters (Noltimier et al., 1999). The RADARSAT-1 SAR image mosaic of Antarctica is shown in Figure 2.3.

In general, bright areas are caused by crevassing or surface melting followed by refreezing. Dark areas are indicative of fine-grained snow and smooth ice surfaces. Most coastal areas and much of the Antarctic Peninsula appear bright because of refrozen seasonal melt. The seasonal sea ice cover is darker than the ice shelves, making the ice terminus relatively easy to identify.

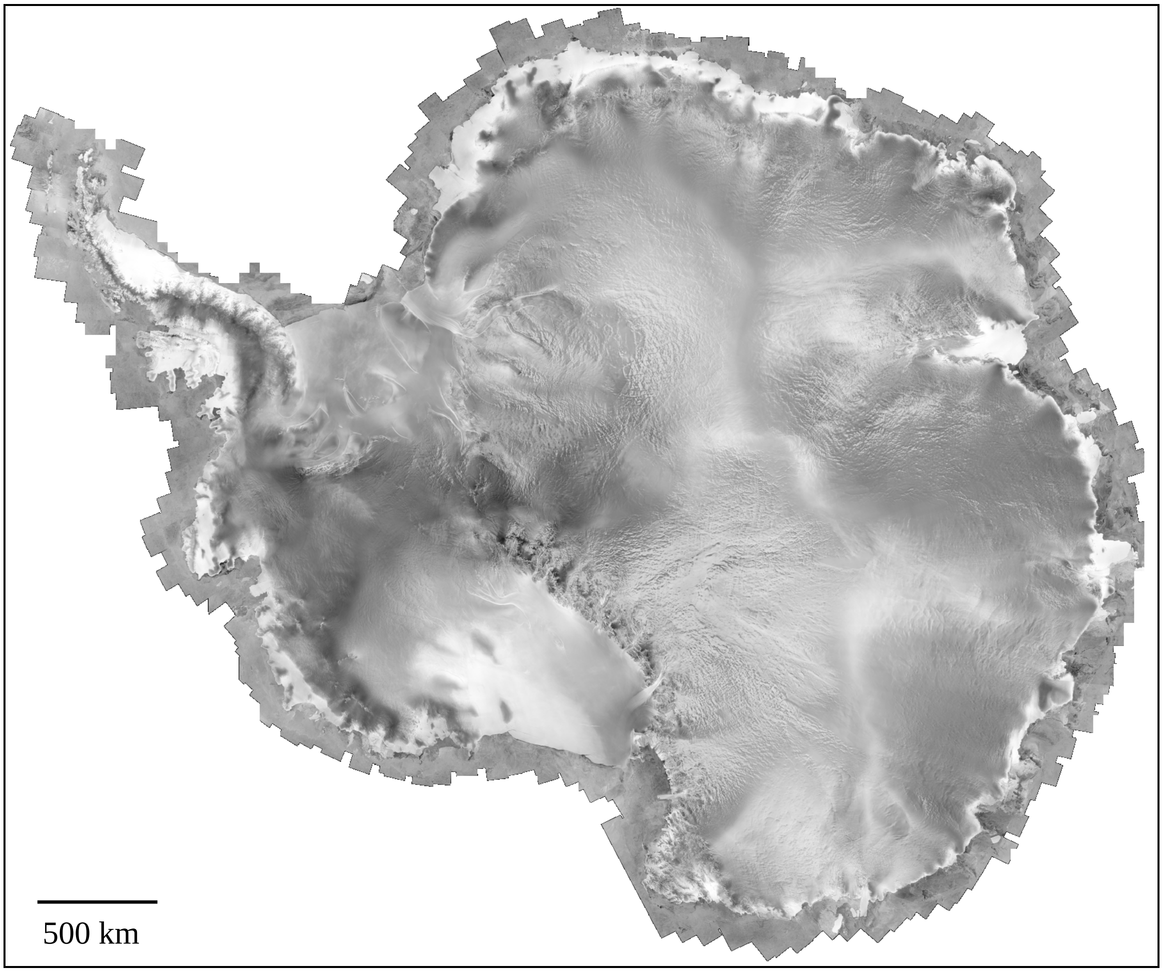

Figure 2.3 RADARSAT-1 SAR image mosaic of Antarctica, 1997

2.4 Antarctic Coastlines derived from the 1997 RADARSAT-1 SAR Mosaic

Liu and Jezek (2003) extracted the Antarctic coastline from the 25-meter resolution 1997 RADARSAT-1 SAR image mosaic. To do this, they refined a sequence of image processing algorithms originally performed by Sohn (1996) and Haverkamp et al. (1995). The key components were image segmentation based on a local dynamic threshold technique (Chow and Kaneko, 1972) after speckle noise removal and edge enhancement using an anisotropic diffusion algorithm, which was used for minimizing speckle noise while not perturbing the position and magnitude of significant edge features. The map of the Antarctic coastline extracted from the 1997 RADARSAT-1 mosaic is shown in Figure 2.4.

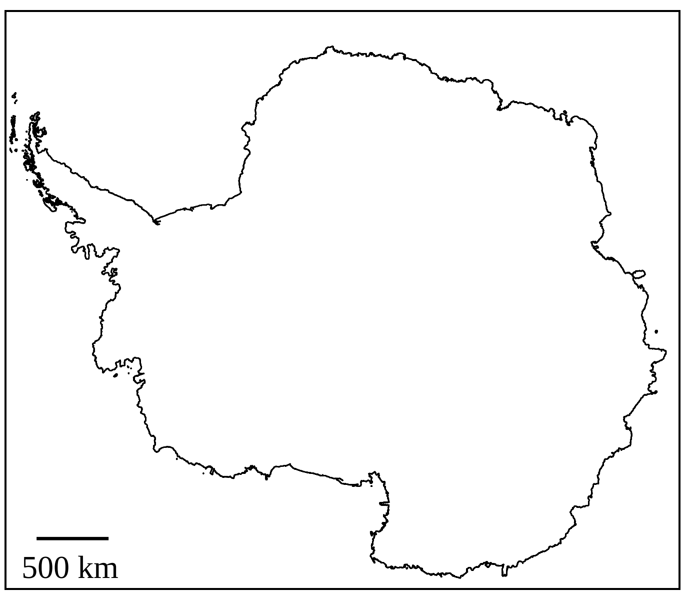

Figure 2.4 Antarctic coastline derived from the 1997 RADARSAT-1 SAR image mosaic

2.5 Antarctic Digital Database

Antarctic Digital Database (ADD) published by the Scientific Committee on Antarctic Research (SCAR) is a comprehensive digital collection of vector cartographic data for Antarctica. This data is a topographic database compiled from a variety of Antarctic map and satellite image sources (ADD Consortium, 2000). Recently the British Antarctic Survey released a new version of the database. In this version, the coastline in the Australian sector - between 12° E and 168° E – has been replaced with a much more detailed version provided by the Australian Antarctic Division, and the coastline of the Antarctic Peninsula north of about 68° S has also been refined. However, the source information used for updating the previous version is not available in public at this moment (Cooper in personal communication, 2003), so the ADD 3.0 is used in this study. Of 16 database layers, the coast layer represents the ice and rock coastline, including the grounding line of ice shelves or glacier tongues and the front of ice shelves. Figure 2.5 shows the map of Antarctic Ice Sheet and the International Map of the World (IMW) index number.

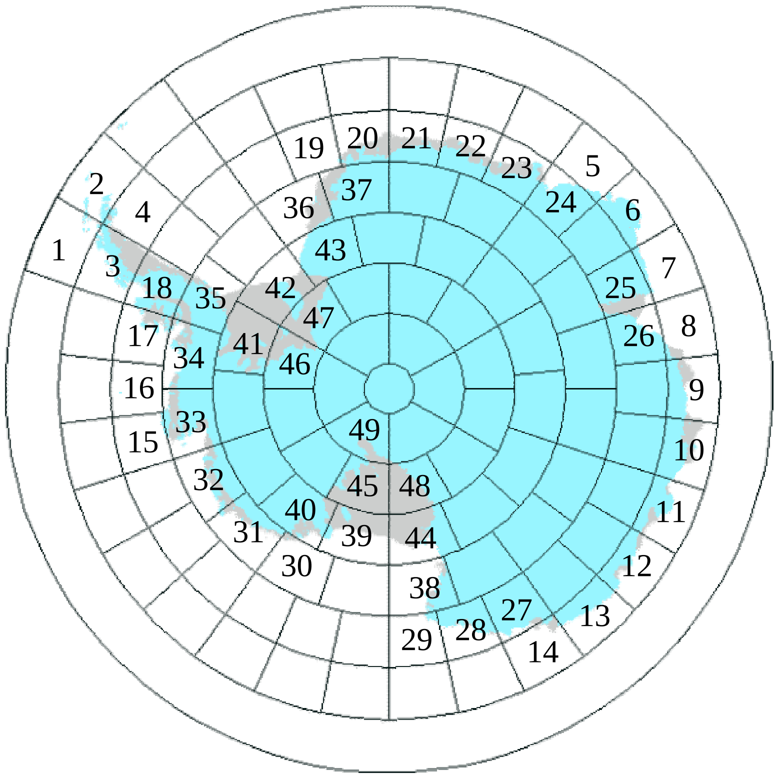

Figure 2.5 Map of Antarctica showing the International Map of the World (IMW) with index numbers (ADD Consortium, 2000)

The source information (version 3.0) about original coastline layers is shown in Table 2.3. According to this information, the temporal resolution of the SCAR ADD coastline is between the late 1960s and the early 1990s. Also the spatial accuracies can be estimated by considering the scale (Light, 1993). This suggests that the SCAR ADD coastline may be systematically displaced by several meters to several kilometers. The SCAR ADD 3.0 coastline and grounding line of Antarctica are shown in Figure 2.6.

Index	Tile Number	Year	Scale	Source	Projection
1	SP 19-20	1977	1:250,000	BAS[1]	Lambert
2	SP 21-22	1978	1:250,000	BSA	Lambert
3	SQ 19-20	1978	1:250,000	BSA	Lambert
4	SQ 21-22	1978	1:250,000	BAS	Lambert
5	SQ 37-38	1974	1:1,000,000	ADNM[2]	Lambert
6	SQ 39-40	1969	1:1,000,000	ADNM	Lambert
7	SQ 41-42	1971	1:1,000,000	ADNM	Lambert
8	SQ 43-44	1969	1:1,000,000	ADNM	Lambert
9	SQ 45-46	1969	1:1,000,000	ADNM	Lambert
10	SQ 47-48	1969	1:1,000,000	ADNM	Lambert
11	SQ 49-50	1971	1:1,000,000	ADNM	Lambert
12	SQ 51-52	1971	1:1,000,000	ADNM	Lambert
13	SQ 53-54	1971	1:1,000,000	ADNM	Lambert
14	SQ 55-56	1971	1:1,000,000	ADNM	Lambert
15	SR 13-14	1968	1:500,000	USGS[3]	Polar Stereo
16	SR 15-16	1988	1:500,000	NP[4]	UTM
17	SR 17-18	1978	1:250,000	BSA	Lambert
18	SR 19-20	1978	1:250,000	BSA	Lambert
19	SR 27-28	1991	1:1,000,000	IFAG[5]	Lambert
20	SR 29-30	1983	1:6,000,000	SPRI[6]	Polar Stereo
21	SR 31-32	1976	1:1,000,000	USSR	Polyconic
22	SR 33-34	1983	1:6,000,000	SPRI	Polar Stereo
23	SR 35-36	1983	1:6,000,000	SPRI	Polar Stereo
24	SR 37-38	1974	1:1,000,000	ADNM	Lambert
25	SR 41-42	1971	1:1,000,000	ADNM	Lambert
26	SR 43-44	1971	1:1,000,000	ADNM	Lambert
27	SR 55-56	1974	1:1,000,000	ADNM	Lambert
28	SR 57-58	1975	1:1,000,000	ADNM	Lambert
29	SR 59-60	1970	1:250,000	USGS	Lambert
30	SS 04-06	1968	1:500,000	USGS	Polar Stereo
31	SS 07-09	1974	1:250,000	USGS	Lambert
32	SS 10-12	1968	1:500,000	USGS	Polar Stereo
33	SS 13-15	1968	1:500,000	USGS	Polar Stereo
34	SS 16-18	1968	1:500,000	USGS	Polar Stereo
35	SS 19-21	1978	1:250,000	BSA	Lambert
36	SS 25-27	1990	1:1,000,000	IFAG	Lambert
37	SS 28-30	1988	1:1,000,000	IFAG	Lambert
38	SS 58-60	1989	1:250,000	USGS	Lambert
39	ST 01-04	1983	1:6,000,000	SPRI	Polar Stereo
40	ST 05-08	1983	1:6,000,000	SPRI	Polar Stereo

Continued

[1] British Antarctic Survey; [2] Australian Division of National Mapping; [3] United State Geological Survey; [4] Norsk Polarinstitutt topographic map; [5] Institut fur Angewandte Geodasie; [6] Scott Polar Research Institute [7] International Glaciological Society. [8] Council of Ministers of USSR.

Table 2.3 Original data source information based on ADD 3.0 (ADD Consortium, 2000)

41	ST 17-20	1991	1:1,000,000	IFAG	Lambert
42	ST 21-24	1991	1:1,000,000	IFAG	Lambert
43	ST 25-28	1991	1:1,000,000	IFAG	Lambert
44	ST 57-60	1989	1:250,000	USGS	Lambert
45	SU 01-05	1988	unavailable	IGS[7]	Unavailable
46	SU 16-20	1983	1:6,000,000	SPRI	Polar Stereo
47	SU 21-25	1983	1:6,000,000	SPRI	Polar Stereo
48	SU 56-60	1966	1:250,000	USGS	Polar Stereo
49	SV 01-10	1976	1:1,000,000	USSR[8]	Polyconic

Table 2.3 Original data source information based on ADD 3.0 (ADD Consortium, 2000)

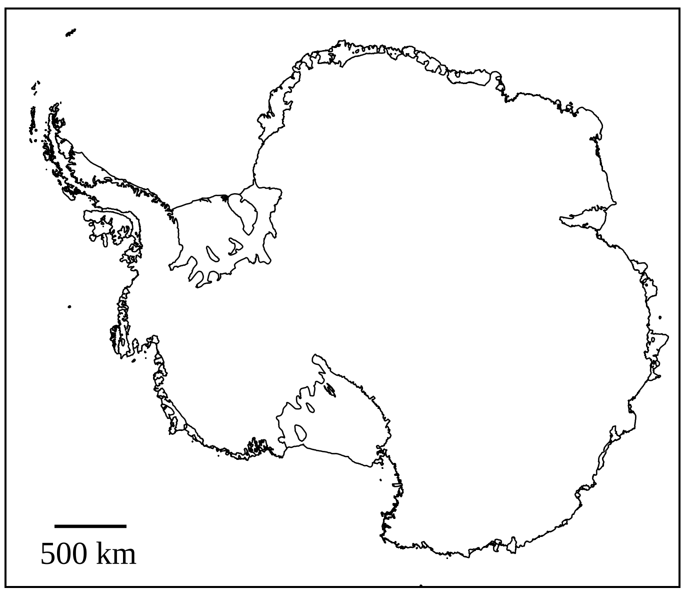

Figure 2.6 SCAR ADD 3.0 coastline and grounding line (inside) of Antarctica

CHAPTER 3

RIGOROUS ORTHORECTIFICATION OF SATELLITE PHOTOGRAPHS

3.1 Introduction

Raw, remotely sensed image data gathered by a satellite are a representation of the irregular surface of the Earth. Because they do not have a uniform scale, we cannot directly measure distance on a satellite image. Instead, digital rectification techniques must be used to generate a uniform-scale image map. Bundle block triangulation and orthorectification using a DEM were applied to Argon DISP photographs with varied terrain surface, and the orthorectified images were mosaicked to create a map-quality image mosaic of the Antarctic coastal areas.

A simple photogrammetric and mapping technique using a DEM was implemented to derive accurate positional information from Argon photographs acquired over a specific sector of Antarctica (Kim et al., 2001). A single photo resection method was used to orthorectify five Argon photographs. The orthorectified images were then assembled into a common coordinate system. More rigorous orthorectification and mosaic techniques were proposed by Zhou et al. (2002). 24 Argon photographs acquired over the entire Greenland were integrated by the bundle adjustment method and satellite orbital parameters, solving for interior and exterior orientations as well as lens distortion parameters simultaneously. In the case of featureless photographs, the parameters were interpolated or extrapolated by the adjacent, known orbital parameters in the same orbit. However, this is not the case of the Antarctic coastal areas because as shown in Figure 2.1, most photographs are not in the same orbit.

This chapter explains the processes of geometrically and radiometrically correcting the Argon photographs of the Antarctic coastal areas, so that they can be represented on a planar surface, conform to other images, and have the integrity of a map. The processes are basically similar to Zhou et al.'s, but without estimating interior and lens distortion parameters. For this reason, the processes proposed in this study need fewer control points, but preserve similar accuracy.

3.2 Digitizing Argon DISP Photographs

Argon was a film-return system, and its imagery is available in film product from Earth Resources Observation Systems (EROS) Data Center (http://edc.usgs.gov/). Argon imagery had an estimated film resolution of 30 line-pair/mm and a ground resolution of approximate 140 meters. This is equivalent to a 33 μm pixel resolution. Sampling theory was applied to determine the range of acceptable spot size that preserves the original film resolution (Light, 1993).

$$\frac{33\mu m}{2\sqrt{2}} \leq scan\ \ spot\ \ size \leq \frac{33\mu m}{2} \qquad \Rightarrow \qquad 11\mu m \leq scan\ \ spot\ \ size \leq 17\mu m$$

Argon imagery was scanned at 7µm, which is slightly smaller than the scan spot size calculated by sampling theory using the INTERGRAPH PhotoScan TD® Scanner, which is a high-resolution radiometrically and geometrically precise flatbed scanning system.

There were two parameters that affect the appearance of a scanned image: transmissivity and mapping function. Film transmissivity is a value that expresses the percent of light that passes through film. Where no light passes, the transmissivity at that location is zero. Transmissivity is close to 1 where film is completely transparent. A mapping function is an equation that maps input film transmissivity values to output pixel intensities (e.g, 0-255). Therefore, it is important that the minimum transmissivity ($T_{\min}$) and the maximum transmissivity ($T_{\max}$) be as close as possible to the minimum and maximum film transmissivity values of the photographs.

A test scan was conducted to determine the best $T_{\min}$ and $T_{\max}$ settings for Argon photographs. They were first scanned at a low resolution of 224 µm with a default transmissivity range of 0.001 and 1.0 and a liner mapping function. After conducting a test scan, the minimum ($G_{\min}$) and maximum ($G_{\max}$) gray values were observed from the histogram. $T_{\min}$ and $T_{\max}$ were then determined by:

$$T\max\_new = \left(\frac{(T\max - T\min)}{255} \times G\max \right) + T\min$$
$$T\min\_new = \left(\frac{(T\max - T\min)}{255} \times G\min \right) + T\min$$

Once the new $T_{\min}$ and $T_{\max}$ values were determined, the imagery was scanned with these values at 7 μm.

3.3 Bundle Block Triangulation

Argon satellite photographs were captured with overlap areas. This is advantageous and allows us to use the bundle block triangulation, which can incorporate the minimum number of points distributed across several overlapping scenes. This method is especially important in the image data over Antarctica where cloud cover can obscure large sectors of an intermediate image.

3.3.1 Coordinate System

Three different coordinate systems are involved in orthorectifying the digitized Argon images. They are the pixel, the image, and the object coordinate systems. Figure 3.1 shows the pixel coordinate system. This system is defined as a left-handed system, because an image is often scanned from left to right in columns and from top to bottom in rows. The origin of the pixel coordinate system is in the upper left corner.

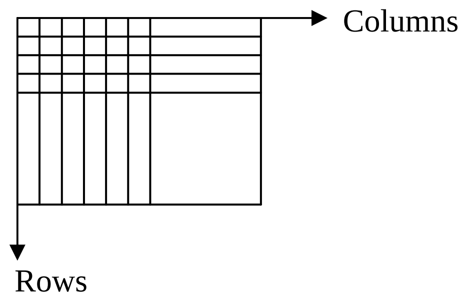

Figure 3.1 Pixel coordinate system

The image coordinate system serves as the reference for expressing spatial positions of the image space. Figure 3.2 shows the image coordinate system and the configuration of Argon imagery with four fiducial marks. Its origin is in the perspective center (PC). The fiducial marks define the fiducial center (FC). The principal point (PP) is mathematically defined as the intersection of the perpendicular line to the image plane through the perspective center of the image space. The length from the principal point to the perspective center is called the focal length (f). If the optical system of camera has some distortion, this point will be slightly different from the fiducial center. In other words, the principal point corresponds to the fiducial center when an ideal camera is assumed. Under this assumption, we used value $(x, y) = (0, 0)$ as the Argon image coordinates of the principal point. Then, an image position is expressed as a point vector, $p = \begin{bmatrix} x & y & -f \end{bmatrix}^T$ in the image coordinate system. This assumption is reasonable because the bundle block method used in this study is indirect. That is, the idea in bundle block adjustment is to iteratively find the set of exterior orientation parameters, which minimizes the squared errors of image coordinates for observations. The rays forming the bundles are made to intersect in the object space and errors are treated in the image coordinate system, not in object coordinate system (Altmaier et al., 2002 and Shin, 2003).

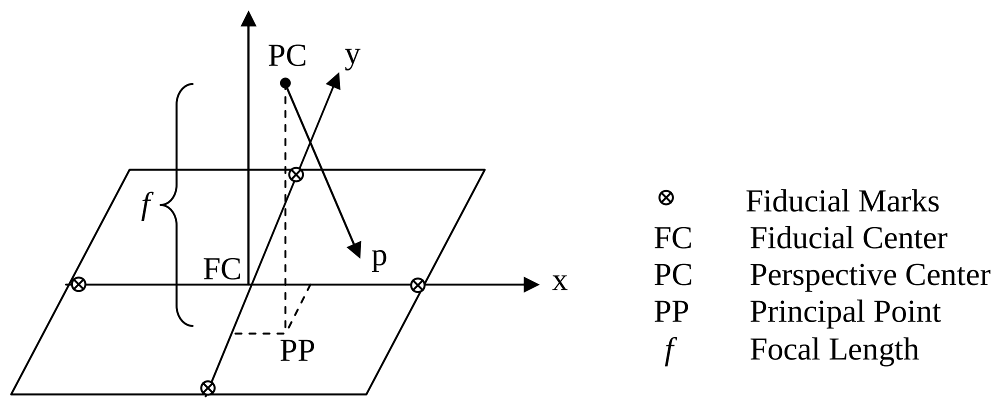

Figure 3.2 Image coordinate system

For a polar research, the object coordinate system is often represented by a local three-dimensional Cartesian system with a plane tangential to the ellipsoid (WGS84) at the center of the image. Table 3.1 summarizes the relationships between the pixel, the image, and the object coordinate systems with the associated procedures and the underlying mathematical models.

Relationship	Procedure	Mathematical model
Pixel coordinate system and image coordinate system	Interior orientation	Affine Transformation
Image coordinate system and object coordinate system	Exterior orientation	Collinearity Equations

Table 3.1 Relationships of three different coordinate system

3.3.2 Interior Orientation

Interior orientation defines the internal geometry of a camera, as it existed at the time of image capture. The variables associated with the image space are defined during the process of interior orientation. Interior orientation is primarily used to transform the pixel coordinate system to the image coordinates system whose origin is at the center of the image. Figure 3.3 shows the difference between the (x, y) pixel coordinate system and the (x', y') image coordinate system.

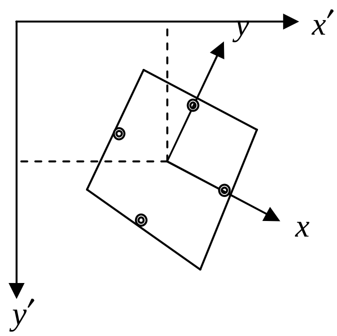

Figure 3.3 Pixel coordinate system vs. image coordinate system

Using a two-dimensional affine transformation, the relationship between the pixel coordinate system and the image coordinate system is defined. The following two-dimensional affine transformation can be used to determine the coefficients required to transform pixel coordinate measurements to the image coordinates:

$$x = a_1 + a_2 x' + a_3 y'$$
$$y = b_1 + b_2 x' + b_3 y' \tag{3.1}$$

x and y are determined by the coordinates of fiducial marks in the image coordinate system. The x' and y' pixel coordinates are the measured coordinates of fiducial marks in the pixel coordinate system. They are used to determine six affine transformation coefficients. The resulting six coefficients can be used to transform each set of row and column pixel coordinates to image coordinates (Figure 3.2).

The affine transformation defines the translation between two different origins of the pixel coordinate system and the image coordinate system. Additionally, the affine transformation takes into account rotation of the image coordinate system. A scanned image of a photograph is normally rotated due to the scanning procedure. The degree of variation between the x- and y-axis is referred to as nonorthogonality. The two-dimensional affine transformation also considers the degree of nonorthogonality. Scale differences between the x- and y-axis are also addressed using the affine transformation.

3.3.3 Exterior Orientation

Exterior orientation defines the position and angular orientation associated with an image in the object space. The variables defining the position and orientation of an image are referred to as the elements of exterior orientation. The elements of exterior orientation define the characteristics associated with an image at the time of exposure. The positional elements of exterior orientation define the position of the perspective center with respect to the object coordinate system. The angular elements of exterior orientation describe the relationship between the object coordinate system and the image coordinate system. The angular elements are omega (ω), phi (φ), and kappa (κ); ω is a rotation about the x-axis, φ is a rotation about the y-axis, and κ is a rotation about the z-axis.

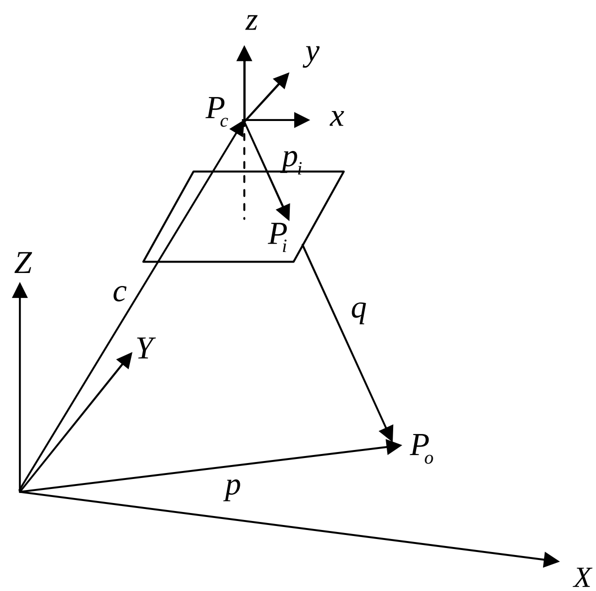

Figure 3.4 Elements of exterior orientation

The collinearity model (Kraus, 1993 and Slama et al., 1980) determines the six elements of exterior orientation. An overview of exterior orientation parameters is shown in Figure 3.4. The collinearity model imposes the condition that the perspective center P_c, the image point P_i, and the object point P_o must be on a straight line. If the exterior orientation is known, then the image vector p_i and the vector q in object space are collinear:

$$p_i = \frac{1}{\lambda} q \tag{3.2}$$

Vector q is the difference between the two vectors, c and p. To satisfy the collinearity condition, we rotate and scale vector q from object to image space. We have

$$p_i = \frac{1}{\lambda} Rq = \frac{1}{\lambda} R(p - c) \tag{3.3}$$

with R an orthogonal rotation matrix consisting of the three angles ω, φ, and κ:

$$R = R_\omega R_\varphi R_\kappa = \begin{bmatrix} \cos\varphi\cos\kappa & -\cos\varphi\sin\kappa & \sin\varphi \\ \cos\omega\sin\kappa + \sin\omega\sin\varphi\cos\kappa & \cos\omega\cos\kappa - \sin\omega\sin\varphi\sin\kappa & -\sin\omega\cos\varphi \\ \sin\omega\sin\kappa - \cos\omega\sin\varphi\cos\kappa & \sin\omega\cos\kappa + \cos\omega\sin\varphi\sin\kappa & \cos\omega\cos\varphi \end{bmatrix}$$

The rotation matrix R is derived by applying a sequential rotation of ω about the x-axis, φ about the y-axis, and κ about the z-axis. Equation (3.3) renders the following three coordinate equations:

$$\begin{aligned} x &= \frac{1}{\lambda}\left\{(X_p - X_c)r_{11} + (Y_p - Y_c)r_{12} + (Z_p - Z_c)r_{13}\right\} \\ y &= \frac{1}{\lambda}\left\{(X_p - X_c)r_{21} + (Y_p - Y_c)r_{22} + (Z_p - Z_c)r_{23}\right\} \\ -f &= \frac{1}{\lambda}\left\{(X_p - X_c)r_{31} + (Y_p - Y_c)r_{32} + (Z_p - Z_c)r_{33}\right\} \end{aligned} \tag{3.4}$$

where,

x, y are the observed image coordinates;

X_p, Y_p, Z_p are the corresponding object coordinates;

X_c, Y_c, Z_c are locations of the perspective center; and

f is the focal length of camera.

By dividing the first by the third and the second by the third equation, the scale factor $1/\lambda$, is eliminated leading to the following two collinearity equations:

$$
\begin{aligned}
x &= -f\,\frac{r_{11}(X_p - X_c) + r_{12}(Y_p - Y_c) + r_{13}(Z_p - Z_c)}{r_{31}(X_p - X_c) + r_{32}(Y_p - Y_c) + r_{33}(Z_p - Z_c)} \\
y &= -f\,\frac{r_{21}(X_p - X_c) + r_{22}(Y_p - Y_c) + r_{23}(Z_p - Z_c)}{r_{31}(X_p - X_c) + r_{32}(Y_p - Y_c) + r_{33}(Z_p - Z_c)}
\end{aligned}
\qquad (3.5)
$$

X_c, Y_c, Z_c, ω, φ, and κ are the unknown parameters of exterior orientation. One set of equations can be formulated for each object point appearing on an image.

3.3.4 Bundle Block Adjustment

The bundle block adjustment is the process of establishing a mathematical relationship between the images, the camera model, and the object. This process provides a cost, time effective way for processing multiple images forming a block. Since the block is being processed in one step, the whole process is much faster than if each image is processed individually. This is mainly due to the number of control points required per image being greatly reduced. In addition to control points, tie points measured in overlap areas of two or more images are used for geometrically connecting the images. Although the object coordinates are unknown for the tie points, they increase the stability of the block and assist in finding the relationship between the images. For this reason, despite fewer control points, bundle block adjustment results in better accuracies than if each image is processed individually.

A bundled solution is computed including the exterior orientation of each image and the X, Y, and Z object coordinates of tie points. The bundle block adjustment uses the collinearity condition as the basis for formulating the relationship between image space and object space. A block of images is simultaneously processed in one solution. A statistical technique, known as least squares adjustment, is used to estimate the bundled solution for the entire block while minimizing errors.

Once the bundle block adjustment has been solved, the exterior orientation parameters of each image are known. These parameters together with a DEM can then be used to perform the image orthorectification.

3.3.5 Least Squares Adjustment

Least squares adjustment is a statistical technique that is used to estimate the unknown parameters associated with a solution while minimizing errors within the solution. With respect to bundle block adjustment, least squares adjustment techniques are used to estimate the exterior orientation, the X, Y, and Z object coordinates of tie points. Errors in the estimated result are attributed to the inaccuracy associated with the measured tie points and control points, camera information, and systematic errors.

A simplified version of the least squares observation equations can be introduced by the Gauss Markov model (Koch, 1988) as follows:

$$y = A\xi + e \qquad e \sim N(0, \sigma_0^{\,2} p^{-1}) \tag{3.6}$$

where,

y is a ($n \times 1$) vector of observations;

A is a ($n \times m$) matrix of partial derivatives with respect to the unknown parameters, including exterior orientation and object coordinates of tie points;

ξ is a ($m \times 1$) vector containing the corrections of the unknown parameters;

e is a ($n \times 1$) vector of errors;

n is the number of the observations;

m is the number of the unknowns;

$\sigma_o^{\,2}$ is the variance component of observation; and

p is a ($n \times n$) weight matrix of the observations.

It must be noted that only over-determined cases are considered in photogrammetric approaches. In other words, the number of observations is larger than the number of unknowns (e.g., $n > m$). The ξ vector is then estimated in the following manner:

$$\hat{\xi} = (A^T pA)^{-1} A^T py \tag{3.7}$$

The dispersion of the estimated parameters $\hat{\xi}$ can be also derived from the law of error propagation:

$$D\{\hat{\xi}\} = \sigma_0{}^2 (A^T pA)^{-1} \tag{3.8}$$

The predicted residual vector, $\tilde{e}$ can be computed as $\tilde{e} = y - A\hat{\xi}$. Finally the estimate for the variance component $\hat{\sigma}_o{}^2$ can be:

$$\hat{\sigma}_o{}^2 = \frac{\tilde{e}^T p\tilde{e}}{n-m} \tag{3.9}$$

where ($n-m$) is the redundancy of the system. The estimated variance-covariance matrix of $\hat{\xi}$ is expressed by:

$$\hat{D}\{\hat{\xi}\} = \hat{\sigma}_o{}^2 (A^T pA)^{-1} \tag{3.10}$$

At this point, it must be noted that the Gauss Markov model depicted by Equation (3.6) assumes a linear relationship between observations y and unkown parameters ξ. The collinearity equations in Equation (3.5), however, show highly non-linear relationship between the unknown parameters and the observations. The non-linearity can be eliminated by performing linearization using Taylor's series expansion with initial values for the unknown paramters.

By linearizing the collinearity equations, the components of the least squares condition are directly related to the functional model based on collinearity equations. The A matrix is formed by the differencing the functional model with respect to the unknown prarmters such as exterior orientation and object coordinates of tie points. The partial derivatives of collinearity equations are shown in Appendix B. The y vector is formed by subtracting the initial results obtained from the functional model with newly estimated results determined from a new iteration of processing. The ξ vector contains the corrections to the unkown parameters.

For every point in the image coordinates, we obtain two equations that have non-zero coefficients for the six exterior orientations of each image and three coefficients for the object coordinates of each tie point. Adding all observation equations for every measured point in the image coordinates, a design matrix of A can be depicted as Figure 3.5:

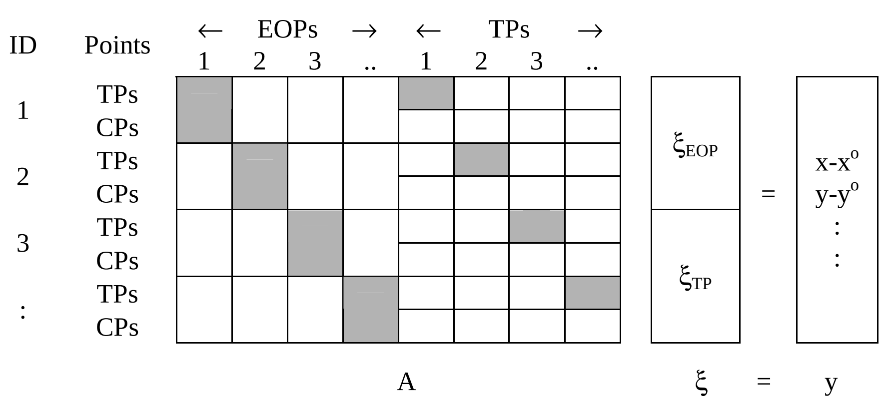

Figure 3.5 Structure of observation equations

The necessary approximations to the unknowns can be derived in various ways. For satellite photographs with approximately vertical axes, we can set approximations for the photo-tilts of $\omega^0 = \varphi^0 = 0$. The approximation κ^0 can be taken from the overview of all photographs (see in Figure 3.7). The initial approximate rotation matrix R^o for a photograph is obtained then:

$$R^o = R_\kappa = \begin{bmatrix} \cos k^o & -\sin k^o & 0 \\ \sin k^o & \cos k^o & 0 \\ 0 & 0 & 1 \end{bmatrix} \tag{3.11}$$

The approximate coordinates $X_c{}^0$, $Y_c{}^0$ and $Z_c{}^0$ of the perspective centers and the approximate coordinates $X_p{}^0$, $Y_p{}^0$ and $Z_p{}^0$ of the tie points can be derived with the help of the intial approximate rotation matrix R^0.

3.3.6 Grand Adjustment

A special concern is also required for the object coordinates of control points, because the accuracy of control points may not always be good enough for a mapping application. In this case, we can also consider the object coordinates of control points as additional parameters to be adjusted during the least squares process (Schaffrin, 1998). The additional mathematical model for this case is given by:

$$\begin{bmatrix} X \\ Y \\ Z \end{bmatrix} = \begin{bmatrix} X_t \\ Y_t \\ Z_t \end{bmatrix} + \underline{e} = \begin{bmatrix} X_t^{\,o} \\ Y_t^o \\ Z_t^{\,o} \end{bmatrix} + \begin{bmatrix} dX_t \\ dY_t \\ dZ_t \end{bmatrix} + \underline{e}$$

$$\begin{bmatrix} X - X_t^{\,o} \\ Y - Y_t^o \\ Z - Z_t^{\,o} \end{bmatrix} = \begin{bmatrix} dX_t \\ dY_t \\ dZ_t \end{bmatrix} + \underline{e} \quad \underline{e} \sim N(0, \sigma_o^{\,2} p_i^{\,-1}) \tag{3.12}$$

where,

X, Y, Z	are the observed control points;
$X_t^{\,o}, Y_t^o, Z_t^{\,o}$	are the initial values of the observations; and
$\underline{e}$	is the noise vector contaminating $X, Y,$ and Z .

It must be noted that the left-hand side of Equation (3.12) is numerically zero for using the observations themselves as intial values. The effect of the errors in the coordinates of the control points, however, will smear into the adjustment process and affect the estimates of unknown parameters. By combining all the observations and unknown parameters in Eequation (3.6) and (3.12), we can set up the observation equations for the Grand-Adjustment process (Schaffrin, 1997):

$$\begin{bmatrix} y_1 \\ y_2 \end{bmatrix} = \begin{bmatrix} A_1 & A_2 \\ 0 & I \end{bmatrix} \begin{bmatrix} \xi_1 \\ \xi_2 \end{bmatrix} + \begin{bmatrix} \underline{e}_{y_1} \\ \underline{e}_{y_2} \end{bmatrix} \tag{3.13}$$

where,

y_1 is an observation vector in the image coordinates;

y_2 is an observation vector in the object coordinates of control points;

ξ_1 is an unknow vector in the image coordinates;

ξ_2 is an unknow vector in the object coordinates of control points;

A_i are the matrices of the partial derivatives related to the parameters ξ_1 and ξ_2, respectively;

I is an identity matrix; and

$\underline{e}_{y_i}$, $\underline{e}_{y_2}$ are the noises contaminating y_1, y_2 respectively.

Finally, the observation equations for bundle block adjustment can be found as:

$$y = \begin{bmatrix} y_1 \\ y_2 \end{bmatrix}, \quad A = \begin{bmatrix} A_1 & A_2 \\ 0 & I \end{bmatrix}, \quad and \quad \xi = \begin{bmatrix} \xi_1 \\ \xi_2 \end{bmatrix} \tag{3.14}$$

3.4 Orthorectification

Orthorectification is the process of removing geometric errors inherent within imagery. The variables contributing to geometric errors include camera orientation, topographic relief displacement, and Earth's curvature. By performing bundle block triangulation, the parameters associated with camera orientation are defined. Utilizing least squares adjustment techniques during bundle block triangulation minimizes the error associated with camera instability. The effects of the Earth's curvature are significant if satellite imagery in involved. They can be eliminated during bundle block triangulation procedure by introducing a three-dimensional reference system. The effects of topographic relief displacement are considered by utilizing a DEM during the orthorectification procedure.

Relief displacement is corrected by taking each pixel of a DEM and finding the equivalent position in the satellite image. A brightness value is determined for this location based on resampling of the surrounding pixels. The brightness value, elevation, and exterior orientation are used to calculate the equivalent location in the orthorectified image. The orthorectification procedures that find gray values of the orthorectified image are shown in Figure 3.6. A proper resampling method such as nearest neighbor, bilinear interpolation and cubic convolution is required for finding gray values at the non-integer location. Generally, when the cell sizes of orthorectified image pixels are selected, they should be similar or larger than the cell sizes of the original image.

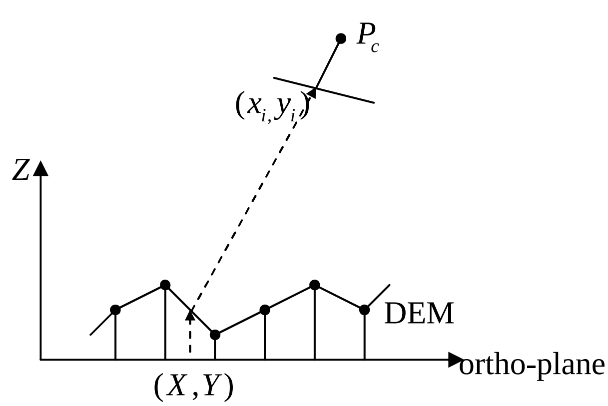

Figure 3.6 Principle of orthorectification

3.5 Mosaicking

Mosaicking is the process of combining georeferenced images into a single composite image covering a larger geographic area. In this case, there are often intensity differences that cause artificial edges at the seam between adjacent images. These intensity differences are mainly due to changes in atmospheric transmittance and in illumination caused by different Sun angles. Seasonal changes of surface reflectance also contribute to the artificial edges in the output mosaic.

Mosaicking processes usually require scaling (or radiometric balancing) to minimize image difference in the mosaic. Thus, the first step is to contrast stretch the images. This is done by adjusting the average gray level of each image to the similar value. The second step is to define a cut-line in overlapping area. A simple, minimum distance algorithm is used for finding pixels that have minimum differences in overlapping area. The cut-line is a polyline defined along the feature boundary in overlapping area.

3.6 Argon DISP Image Mosaic of the Antarctic Coast, 1963

An image mosaic of the Antarctic coast was produced from 1963 Argon DISP satellite photographs. First, Argon photographs were digitized at 7 μm using the INTERGRAPH PhotoScan TD® Scanner, which is high-resolution radiometrically and geometrically precise flatbed scanning system. Second, the digitized images were orthorectified and resampled into a conformal map projection (e.g., Polar Stereographic with the standard parallel at 71° S) with a resolution of 100-m using bundle block triangulation, the OSU Antarctic DEM, and control points selected from the RADARSAT-1 Antarctic Mapping Project image mosaic. Finally, the orthorectified images were mosaicked to create a map-quality image mosaic of the Antarctic coast in 1963.

3.6.1 Problems and Solutions

The fundamental problems in producing accurate image maps of the Antarctic coast using Argon data were that more than 40% of the imagery contained significant cloud cover and that little information is available about the satellite design. Although satellite ephemeris and camera orientation data derived from stellar photography are available, accuracy in locating corner coordinates derived from the collateral materials is more than approximately 80-km at the corners of the images (at http://edc.usgs.gov/guides/disp1.html).

The best way to produce a useful, accurate Antarctic image map using Argon data was to use the small number of control points relating image coordinates to object coordinates. Argon photographs were taken with some overlaps between adjacent photographs, so that bundle block triangulation enabled incorporation of many control points for each image.

3.6.2 Orthorectification and Mosaic

Based on visual inspection of browse images available at EROS Data Center, an optimal data set of 62 Argon DISP photographs covering the entire Antarctic coast (see

Figure 2.1) was identified. From this data set, 15 blocks were created for bundle block triangulation. Each block consisted of 2 to 5 photographs by considering the cloud cover and control points in the block. We note that since the accuracy of points in the case of a strip block depends primarily on the number of photographs bridged between control points, it is a common practice not to bridge more than 5 photographs to be considered in a block (Kraus, 1993).

Figure 3.7 shows one of the blocks illustrating a schematic overview of bundle block triangulation. The overview shows 5 Argon photographs taken over the Antarctic Peninsula. For the orientation of this block of photographs, we selected 17 control points and 12 tie points on the block image. 9 tie points were selected from the areas overlapped by 2 neighboring photographs, and 3 tie points were selected from the areas overlapped by 3 neighboring photographs. The planimetric control points were selected by identifying common features in the orthorectified RADARSAT-1 SAR image mosaic with 100-m pixel resolution and the corresponding vertical control points taken from the OSU Antarctic DEM with 200-m pixel resolution. The summaries of the balance between unknowns and observations for bundle block adjustment and the uncertainties of observations are shown in Table 3.2.

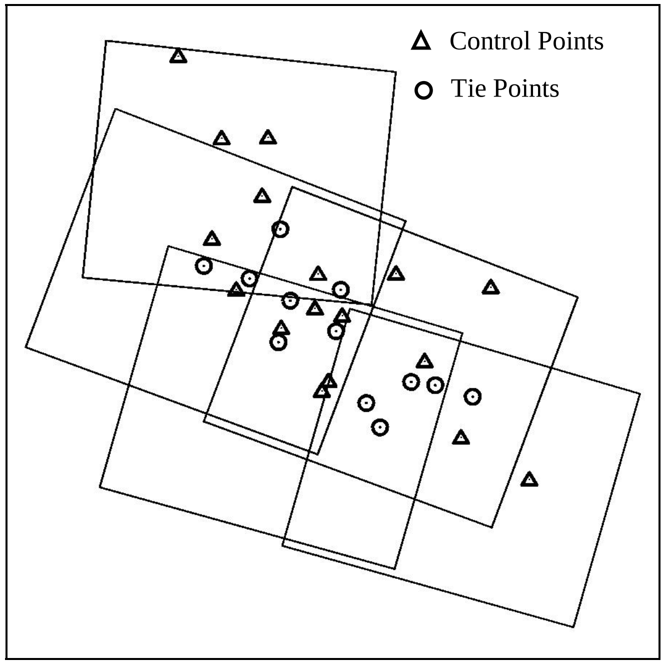

Figure 3.7 Geometric network of observations in an image block

Number of Photographs		5
Number of Control Point		17
Number of Tie Points		12
Number of Observations	9 x 2 x 2 = 36	88
	3 x 2 x 3 = 18	
	17 x 2 = 34	
Number of Unknowns	6 x 5 = 30	66
	12 x 3 = 36	
Redundancy	88 - 66	22
Number of Iteration		6
σ of image coordinate		14-µm
σ of object coordinate		100-m

Table 3.2 Summaries of block statistics

The uncertainties were estimated for the observations to indicate the quality of the observations. The uncertainty of the measured image coordinates was estimated to be 14 μm (two pixels) as a measurement error of the Argon imagery. The uncertainties of the measured object coordinates were estimated to be 100-m (one pixel) as a measurement error from the RADARSAT-1 SAR imagery. These uncertainties were weighted inversely proportional to the uncertainty values, so that points with high error affected the solution less than points with lower error.

For Argon satellite photographs with approximately vertical axes, we set initial approximations for the photo tilts of $\omega^0 = \varphi^0 = 0$. The approximation κ^0 was taken from the overview of all photographs (Figure 3.7). The initial approximate rotation matrix for a photograph was obtained from Equation (3.12). The approximate coordinates $X_c{}^0$, $Y_c{}^0$ and $Z_c{}^0$ of the perspective centers and the approximate coordinates $X_p{}^0$, $Y_p{}^0$ and $Z_p{}^0$ of the tie points were derived using the intial approximate rotation matrix.

The estimates of exterior orientations using bundle block adjustment and geometric network of observations (Figure 3.7) are shown in Table 3.3, respectively.

Id	Positions (m)			Rotations (degree)		
	X_c	Y_c	Z_c	ω	φ	κ
014115	-2366570	1218244	335550	-0.2	-0.2	83.8
029077	-2393420	981917	362357	0.7	1.6	-292.6
029079	-2040780	823749	352517	0.5	-1.3	67.4
045078	-2276139	721396	353903	-0.3	-1.5	-287.9
045080	-1885907	592969	349985	-0.5	-0.5	72.4

Table 3.3 Estimates of exterior orientations

These exterior orientation parameters of each image were used to perform the image orthorectification with a resolution of 100-m using the OSU Antarctic DEM. Figure 3.8 shows the resulting Argon image mosaic of the Antarctic Peninsula.

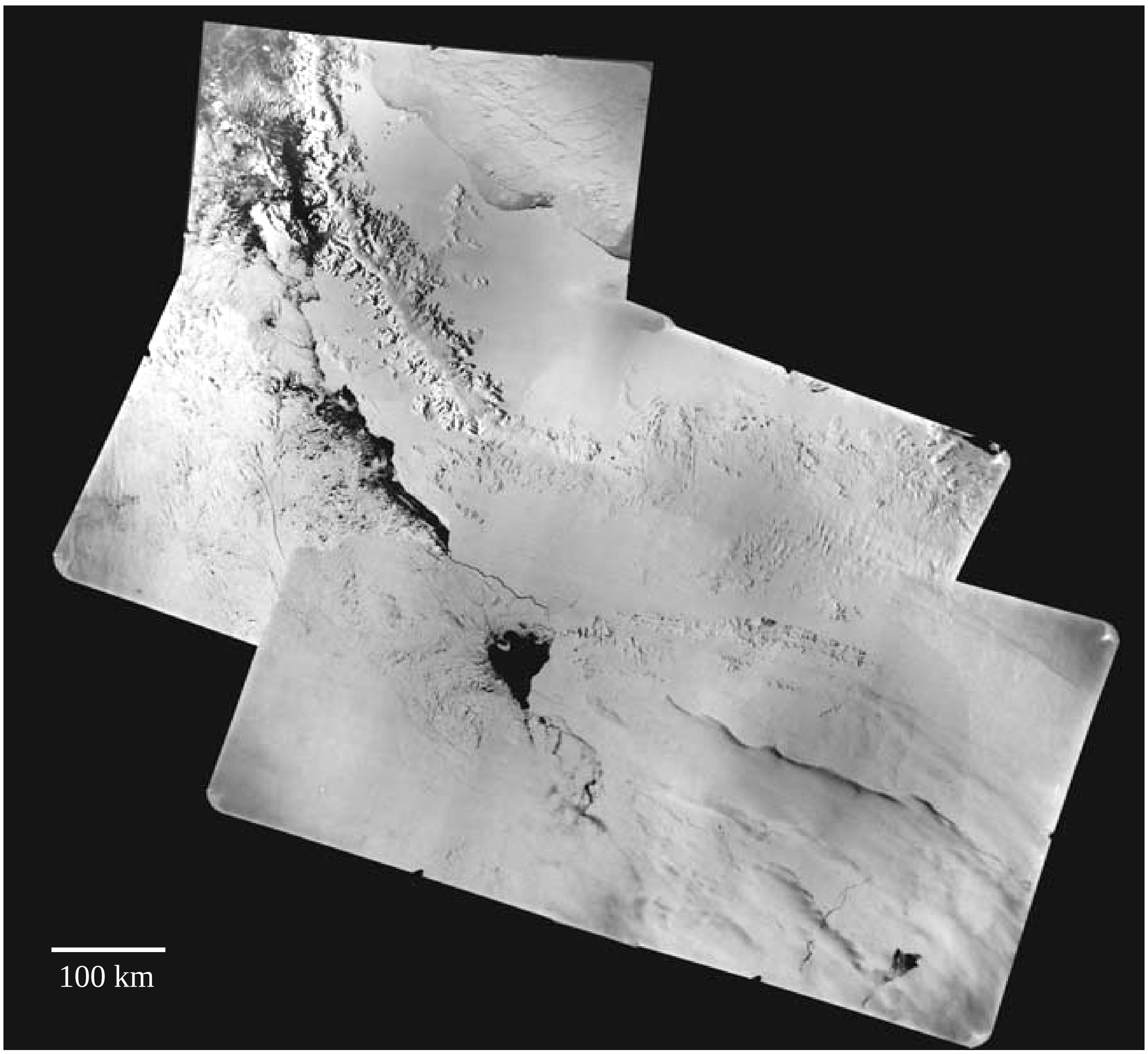

Figure 3.8 Image block mosaic of the Antarctic Peninsula

Coordinates measured on the resulting mosaic must satisfy certain expectations. On the other hand, they must be as accurate as the application demands and, on the other hand, there must be a guarantee that the results are thoroughly checked. Quality control therefore comprises of accuracy.

The unknowns in a bundle block adjustment were the coordinates of the tie points and the control points and the accuracy of these points were calculated from the diagonal elements of the inverse of the normal matrix $(A^T pA)^{-1}$ and the estimate of the variance component $\hat{\sigma}_o{}^2$ using Equation (3.10) as follow:

$$\sigma = \sqrt{\sigma_o{}^2 diag(A^T pA)^{-1}} \tag{3.15}$$

Table 3.4 shows the summary of orthorectified image blocks and their error statistics, and Figure 3.9 shows the orthorectified Argon image mosaic of the entire Antarctic coast. Figure 3.10 shows a configuration of the entire GCPs derived from RADARSAT-1 SAR image mosaic and used for the bundle block triangulations. The detailed map coordinates of the entire GCPs are attached in Appendix A.

Blocks	# photos	# CPs	# TPs	$\sigma_{x\ (m)}$		$\sigma_{y\ (m)}$		$\sigma_{\ (m)}$	
				CP	TP	CP	TP	CP	TP
1	4	17	9	104.94	139.18	127.07	122.32	164.80	185.29
2	2	8	3	93.22	188.24	148.62	181.64	175.43	261.58
3	3	6	6	163.49	166.63	61.53	47.52	174.62	173.27
4	3	7	6	15.99	85.05	10.13	32.06	18.92	90.89
5	3	7	7	100.02	144.40	56.53	126.40	114.88	191.90
6	5	17	9	50.05	141.23	147.68	82.64	155.93	163.63
7	2	8	3	154.41	58.92	167.79	184.32	228.02	193.50
8	4	14	9	111.17	190.13	91.40	184.88	143.91	265.19
9	4	18	7	161.31	89.09	178.86	82.20	240.85	121.21
10	3	10	5	120.75	111.21	84.35	130.23	147.29	171.25
11	2	7	3	50.35	167.97	111.93	125.58	122.73	209.72
12	4	14	8	121.58	107.15	84.83	170.93	148.24	201.73
13	4	17	11	138.35	149.44	154.41	142.21	207.32	206.29
14	4	10	12	112.30	128.51	52.70	123.84	124.05	178.46
15	5	17	12	104.73	123.82	60.27	144.86	120.83	190.56

Table 3.4 Summary and error statistics of orthorectified image blocks

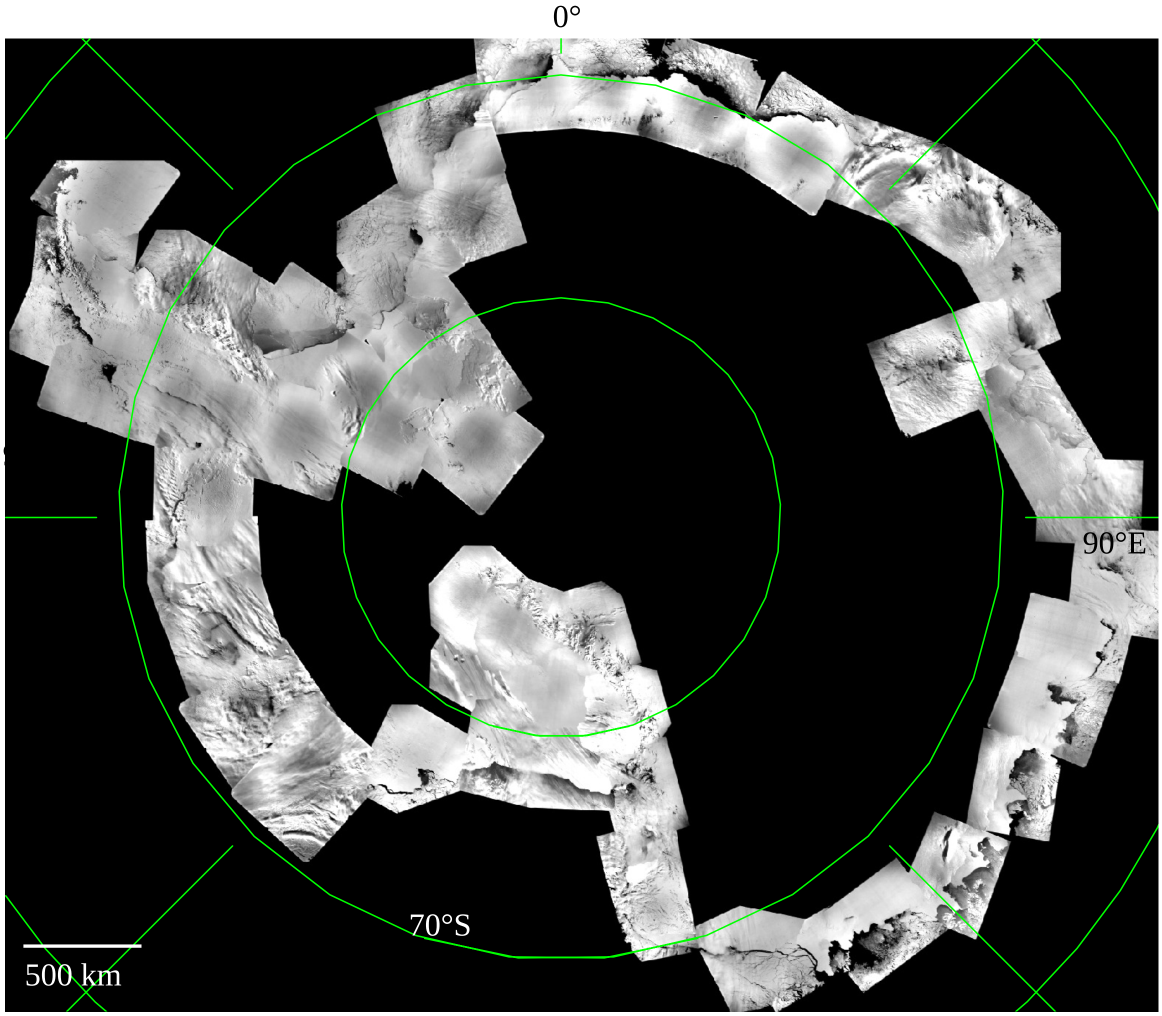

Figure 3.9 Orthorectified Argon DISP image mosaic of the entire Antarctic coast, 1963 in a polar stereo graphic map projection with standard parallel of 71°S (WGS 84)

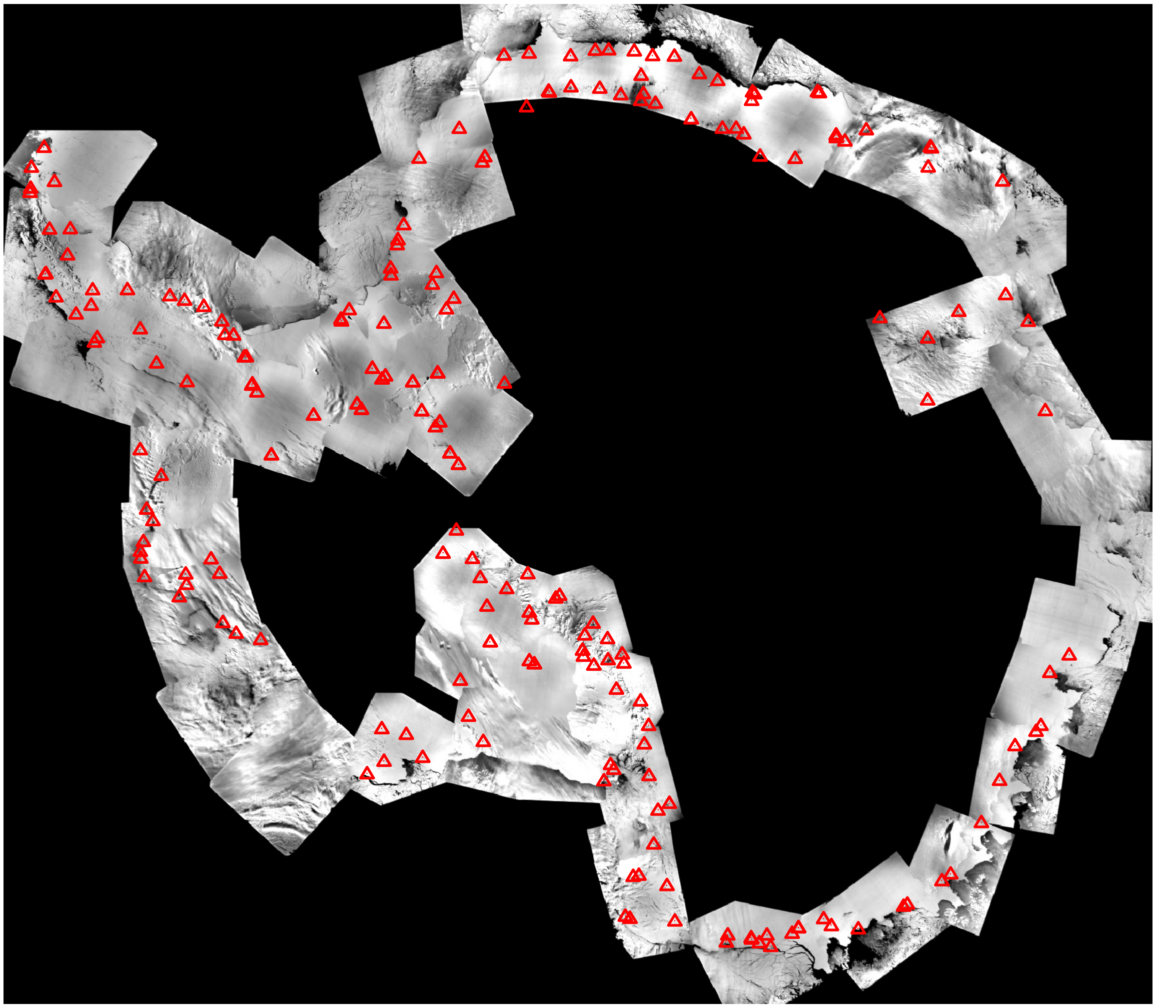

Figure 3.10 Configurations of the entire GCPs used for bundle block triangulations

3.6.3 Summary

The individual Argon photographs are important resources for measuring the geometry of the coastline of Antarctica. By using the most modern digitizing technology, bundle block triangulation based on tie points, and control points derived from the RADARSAT-1 SAR image mosaic, we accurately assembled the individual images into a map quality mosaic of Antarctica as it appeared in 1963. The standard deviations of the resulting image blocks satisfied our mapping application to the Antarctic coastal change within two-pixel accuracy. This became another important benchmark for gauging the response of the Antarctic coastline to changing climate.

CHAPTER 4

AUTOMATED BOUNDARY DETECTION SOFTWARE DESIGN

4.1 Introduction

Segmentation is the process of grouping an observed image into its homogeneous regions. It may also be thought of as a labeling process, where each pixel in the observed image is assigned to a label designating the region or class to which it belongs (Li, 1995 and Tso et al., 2001).

Let y be the observed image intensities defined on a $m \times m$ rectangular lattice $S = \{(i, j) \mid 1 \le i, j \le m\}$, then the labels x may be defined on an identical lattice S. For each site $s = (i, j)$, there is a label x_s specifying to which region the observed pixel value y_s belongs. The relationship between the observed image intensities and the labels can be formulated by Bayesian likelihood functions as follow:

$$\Pr(x \mid y) = \frac{\Pr(y \mid x)\Pr(x)}{\Pr(y)} \tag{4.1}$$

where $\Pr(x)$ is the prior probability density function (PDF) of labels x, $\Pr(y \mid x)$ is the conditional PDF of the observed image intensities y given x, and $\Pr(y)$ is the PDF of y.

A maximum a posterior (MAP) criterion that maximizes the posterior PDF $\Pr(x \mid y)$ with respect to x, provides the estimate of x given y as follow:

$$\hat{x}_{map} = \underbrace{\arg\max}_{x \in X} \Pr(x \mid y) \tag{4.2}$$

Because $\Pr(y)$ in Equation (4.1) is a constant for a fixed y, $\Pr(x \mid y)$ is proportional to the following joint PDF.

$$\Pr(x \mid y) \propto \Pr(x, y) = \Pr(y \mid x)\Pr(x) \tag{4.3}$$

If two random variables x and y are taken to be a Gibbs distribution (GD) with respect to a neighborhood system $\eta = \{\eta_s \mid s \in S, \eta_s \subseteq S\}$, the joint PDF $\Pr(x \mid y)$ is given by:

$$\Pr(x \mid y) = \frac{1}{Z}\exp\left[-U(x \mid y)\right] \tag{4.4}$$

where Z is called the partition function that is simply a normalizing constant, and $U(x \mid y)$ is called the energy function of x given y.

The joint PDF has the physical interpretation that the smaller $U(x \mid y)$, the larger $\Pr(x \mid y)$; consequently the MAP estimate in Equation (4.2) is equivalently found by:

$$\hat{x}_{map} = \underbrace{\arg\min}_{x \in X} \{U(x \mid y)\} \tag{4.5}$$

where,

$$U(x \mid y) = U(y \mid x) + U(x) \tag{4.6}$$

$U(y \mid x)$ is the conditional energy function of y given x, and $U(x)$ is the prior energy function of x. So the MAP estimate for a label x given an observed image intensity y at site s is directly correlated with the conditional energy function $U(y \mid x)$ and the prior energy function $U(x)$.

In practice, there are difficulties in using this MAP estimate. Problems are that the prior information or information concerning the image distribution may not always be available. The Markov random field (MRF) model has been used in determining the prior and conditional PDF (Besag, 1974; Geman and Geman, 1984; Derin and Elliott, 1987; Dubes and Jain, 1989; Geman and Reynolds, 1992). The parameter estimation problem is a crucial issue for the MRF methods, and their performance depends on the availability of correct parameter estimates. These methods work well in supervised mode, where the number of regions and their associated parameters are known. In unsupervised mode, when such knowledge is not available, a problem arises: The main problem is that the model and its parameters are unknown and need to be computed from the given image before segmentation. To compute the parameters effectively the segmented image itself is needed. Simultaneous parameter estimation and segmentation is often computationally prohibitive.

Chellappa (1985) and Lakshmanan & Derin (1989) proposed an alternative strategy, which performs a two-step process: first estimating the parameters in small, non-overlapping regions and performing a coarse segmentation, and then estimating the parameters again from this segmented image using a stochastic relaxation algorithm, such as simulated annealing (Geman and Geman, 1984), iterated conditional modes (Besag, 1986), and maximizer of posterior marginals (Marroquin et al., 1987).

Such algorithms are effective when segmenting images composed of large regions with distinct classes, however, if the class pattern in the images is more complicated then the algorithms perform poorly because they use a windowing function to estimate model parameters (Barker, 1989).

In this study, the fuzzy c-means clustering (FCM) technique (Bezdek et al., 1984) is adopted to improve segmentation performance during the first step process. The computed FCM estimates are then combined with maximizer of posterior marginals (MPM) to obtain an optimum segmentation of the image. The MPM algorithm is similar to simulated annealing and iterated conditional modes, but because any cooling schedule does not exist, it is much faster than others. The proposed Bayesian framework of image segmentation is shown in Figure 4.1.

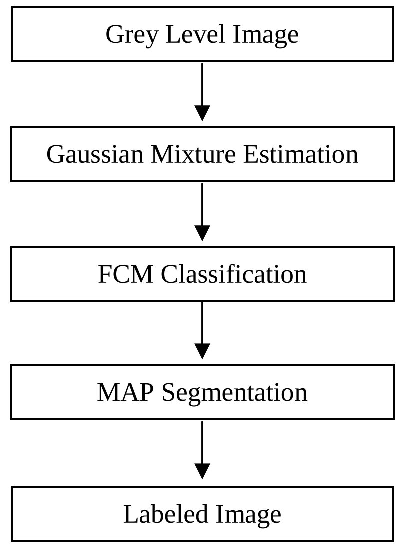

Figure 4.1 Proposed framework of the Bayesian approach to image segmentation

4.2 Segmentation Pre-processing

Noise can be thought of as a random event, which corrupts the signal corresponding to an image. It is undesirable because it changes the image. Thus, if we apply a segmentation technique to the corrupted image without any removal or reduction of noise, we may not successfully achieve our goal in grouping an image into its homogeneous regions. Many techniques have been developed to remove as much of the noise as possible (Lee, 1980; Kuan et al., 1985; Naderi & Sawchuk, 1978; and Froehlich et al, 1981). However, these techniques while removing noise also alter the image, for example, by blurring the edges of the signal due to the use of local statistics computed within a fixed window neighborhood (e.g., 3×3). Thus, one of the main requirements to an algorithm for image enhancement is that the main features of the image as well as their location must be preserved.

In this study, as a segmentation pre-processing, we use the adaptive neighborhood approach to filtering images corrupted by signal-dependent noise (Rangayyan et al., 1998). They proposed a new method for filtering images corrupted by signal-dependent noise based on the linear minimum mean square error (LMMSE) estimation, which requires the first- and second-order statistics of the image. This method estimated the signal and the noise statistics within variable-size, variable-shape neighborhoods around the pixel being processed, instead of within fixed-size, fixed-shape neighborhoods. The neighborhoods were grown for the seed pixel in such a way that they contain only pixels belonging to the same object as the seed. The statistics computed in this manner were used to derive the final estimate of the pixel being processed.

4.2.1 Noise Model

When images recorded on photographic film are digitized to be processed by a digital computer, film-grain noise could be an important source of degradation of the information (Froehlich et al., 1981). The model of an image corrupted by film-grain noise is given by:

$$y_s = x_s + D \cdot F(x_s) \cdot u^1{}_s + u^2{}_s, \qquad u^{1,2}{}_s \sim N(0, \sigma_{1,2}{}^2) \tag{4.7}$$

where y_s is the noisy image; x_s is the uncorrupted image; $u^1{}_s$ and $u^2{}_s$ are samples from two Gaussian-distributed, uncorrelated, zero-mean random processes uncorrelated with the signal and with variance σ_1^2 and $\sigma_2{}^2$, respectively; $F(x)=\sqrt{x}$; and D is a proportionality factor. This noise model is composed of two components: one is signal dependent through the factor $D\sqrt{x_s}\,u^1{}_s$ and another is signal independent given by $u^2{}_s$.

Equation (4.7) can be simply rewritten as an additive noise model:

$$y_s = x_s + e_s, \qquad e_s \sim N(0, \sigma_e{}^2) \tag{4.8}$$

where $e_s = D\sqrt{f_s}\,u^1{}_s + u^2{}_s$. It can be easily shown that e_s is stationary with a zero-mean and a variance as follow:

$$\sigma_{e_s}{}^2 = D^2 E\{x_s\}\sigma_1^2 + \sigma_2{}^2 \tag{4.9}$$

To derive the linear mean-squared error estimates (LMMSE) of this model, we regard further the image as a sample realization of a random filed, which has the following characteristics:

$C\{x_s, e_{s'}\} = 0$ for all s and s′

"no correlation bewteen the signal and the noise"

$$C\{e_s, e_{s'}\} = \begin{cases} 0 & \text{for } s \neq s' \\ \sigma_e^{\,2} & \text{for } s = s' \end{cases} \tag{4.10}$$

"uncorrelated (homoscadiestic) noise process"

4.2.2 Linear Minimum Mean-Squares Error (LMMSE) Estimator

If we restrict ourselves to the class of estimators that are liner functions of the observation y, the LMMSE estimator is a function of the first and second moments of x and y. Then, the LMMSE estimate $\hat{x}$ can be computed for minimizing the MSE, $E\left\{(x-\hat{x})^T(x-\hat{x})\right\}$ as follow:

$$\hat{x} = E\{x\} + C_{xy}C_{yy}^{\ -1}(y - E\{y\}) \tag{4.11}$$

where this LMMSE estimate requires the following information:

$$\begin{aligned}
&E\{x\}: && \text{the mean of x} \\
&E\{y\}: && \text{the mean of y} \\
&C_{xy}: && \text{the cross-covariance matrix of x and y} \\
& && C_{xy} = E[(x - E\{x\})(y - E\{y\})^T] \\
&C_{yy}: && \text{the auto-covariance matrix of y} \\
& && C_{yy} = E[(y - E\{y\})(y - E\{y\})^T]
\end{aligned} \tag{4.12}$$

If x has mean μ_x and variance $\sigma_x{}^2$, the first- and second-order statistics of the observed image can be described by using the characteristics in Equation (4.12):

$$\begin{aligned}\mu_y &= E\{y\} \\ &= E\{x+e\} \\ &= E\{x\} \\ &= \mu_x\end{aligned} \tag{4.13}$$

$$\begin{aligned}\sigma_y{}^2 &= D\{y\} \\ &= D\{x+e\} \\ &= D\{x\}+D\{e\} \\ &= \sigma_x{}^2+\sigma_e{}^2\end{aligned} \tag{4.14}$$

$$\begin{aligned}C_{yy} &= E[(y-\mu_y)^2] \\ &= E[(x+e-\mu_x)^2] \\ &= E[(x-\mu_x)^2]+E[2(x-\mu_x)e]+E[e^2] \\ &= \sigma_x{}^2+\sigma_e{}^2\end{aligned} \tag{4.15}$$

$$\begin{aligned}C_{xy} &= E[(x-\mu_x)(y-\mu_y)] \\ &= E[(x-\mu_x)(x-\mu_x+e)] \\ &= E[(x-\mu_x)^2]+E[(x-\mu_x)e] \\ &= \sigma_x{}^2\end{aligned} \tag{4.16}$$

Then, the LMMSE estimate $\hat{x}$ in Equation (4.11) is simplified by

$$\begin{aligned}\hat{x} &= \mu_x+C_{xy}C_{yy}{}^{-1}(y-\mu_y) \\ &= \mu_y+\frac{\sigma_x{}^2}{\sigma_x{}^2+\sigma_e{}^2}(y-\mu_y)\end{aligned} \tag{4.17}$$

Equation (4.17) is equivalent to the Lee filter (Lee, 1980) in Equation (4.18), which was originally derived to deal with signal-independent additive noise and signal-dependent multiplicative noise, based on a fixed window neighborhood (e.g., 3×3)

$$\hat{x} = \mu_y + \frac{\sigma_y{}^2 - \sigma_e{}^2}{\sigma_y{}^2}(y - \mu_y) \tag{4.18}$$

4.2.3 Adaptive Region Growing

Before correctly using Equation (4.18), a region must be grown for the seed pixel in such a way that it contains only pixels belonging to the same object as the seed pixel using the following tolerance property.

$$|y_{s'} - y_s| \leq T \tag{4.19}$$

where y_s is the seed pixel, $y_{s'}$ is the pixels eight-connected to the seed pixel, and T is a threshold of the adaptive neighborhood. Figure 4.2 shows a flowchart of the adaptive region growing procedures for one pixel in the image. The first step in the procedures is to locally (3 x 3 window) estimate the seed value for the pixel being processed using the alpha-trimmed mean filter (Pitas and Venetsanopoulos, 1992), which is good for eliminating large amplitude spikes of noise while preserving boundaries present in the image. The noise standard deviation given by Equation (4.9) is then computed by using the seed value, and this is assigned to the threshold T. The adaptive region growing is performed to inspect the seed neighborhoods for inclusion in the region according to the criterion in Equation (4.19).

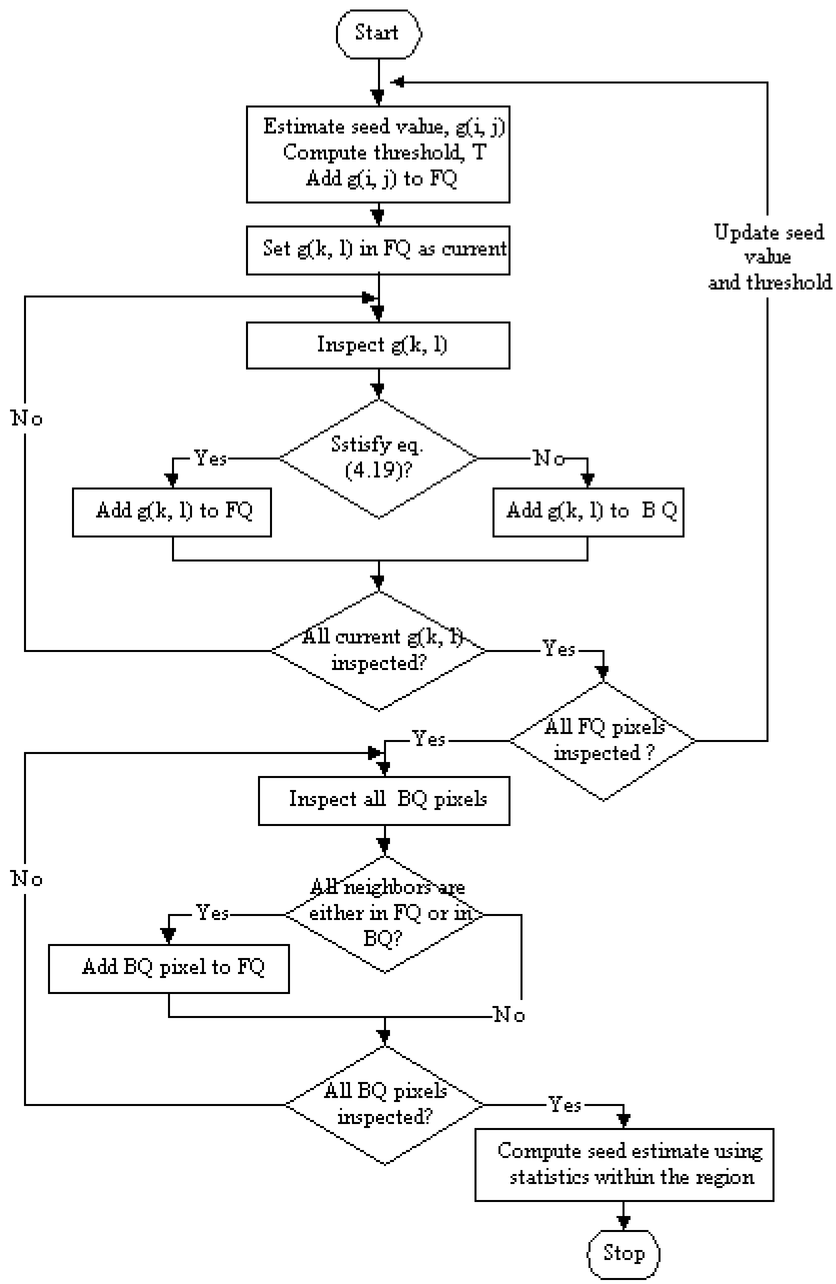

Figure 4.2 Adaptive region growing procedures (Rangayyan et al., 1998)

After the region growing procedure stops, there are three types of pixels: foreground pixels, background pixels, and un-inspected pixels (Figure 4.3).

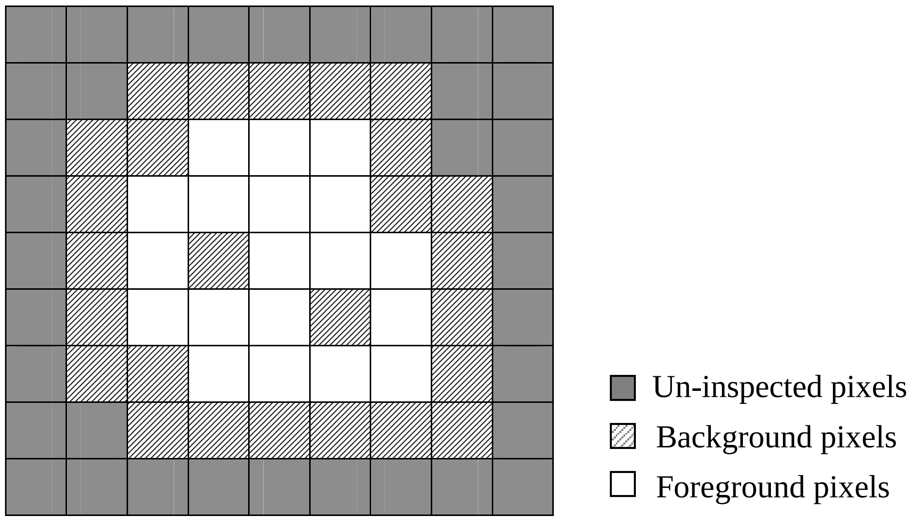

Figure 4.3 Three types of pixels constructed by adaptive region growing

Because a region does not contain background pixels inside the region, some of the background pixels must be checked further for inclusion in the region. The addition criterion for further inclusion of selected background pixels in the region is to find all background pixels whose 8-connected neighbors are all either in the foreground or in the background.

After a region is completely grown, statistics of the signal and the noise are computed by use of the pixels in the foreground. Finally the LMMSE is estimated based on Equation (4.18), and its mean squared error (MSE) between the original and the filtered images is computed by

$$MSE = \frac{1}{m^2}\sum_{i=1}^{m}\sum_{j=1}^{m}\left[x_s - \hat{x}_s\right]^2 \tag{4.20}$$

4.2.4 Examples and Discussions

To simply test the adaptive neighborhood filtering (ANF) described in this section, a synthetic image (256×256) with a set of four gray values (50, 100, 150 and 200) was created and normalized between 0 and 1 in double precision. The synthetic image is shown in Figure 4.4. Gaussian white noise ($\sigma^2 = 0.01$) and multiplicative speckle noise ($\sigma^2 = 0.04$) were simulated with the normalized image. Figure 4.5 shows the images corrupted by simulated noises and their histograms, and Figure 4.6 shows the images filtered with the ANF and their histogram.

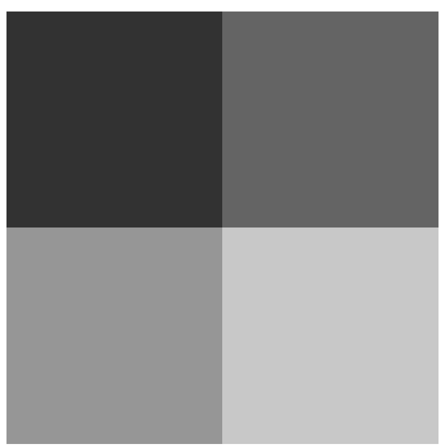

Figure 4.4 The synthetic image (256×256) normalized between 0 to 1 in double precision

(a)

(b)

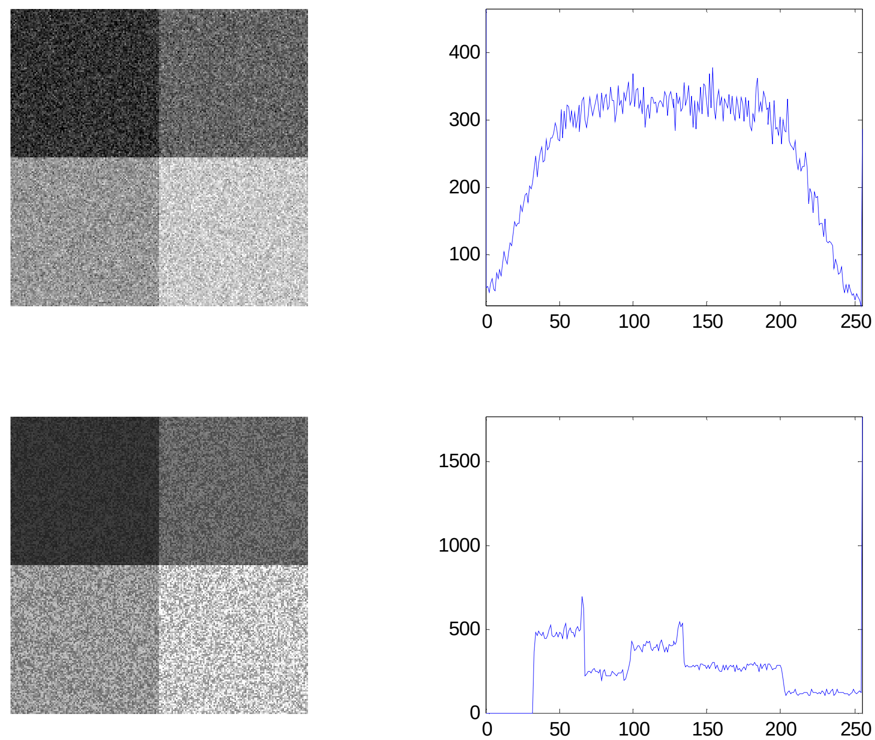

Figure 4.5 Images and histograms corrupted by (a) simulated Gaussian white noise with $\sigma^2 = 0.01$ and (b) simulated multiplicative speckle noise with $\sigma^2 = 0.04$.

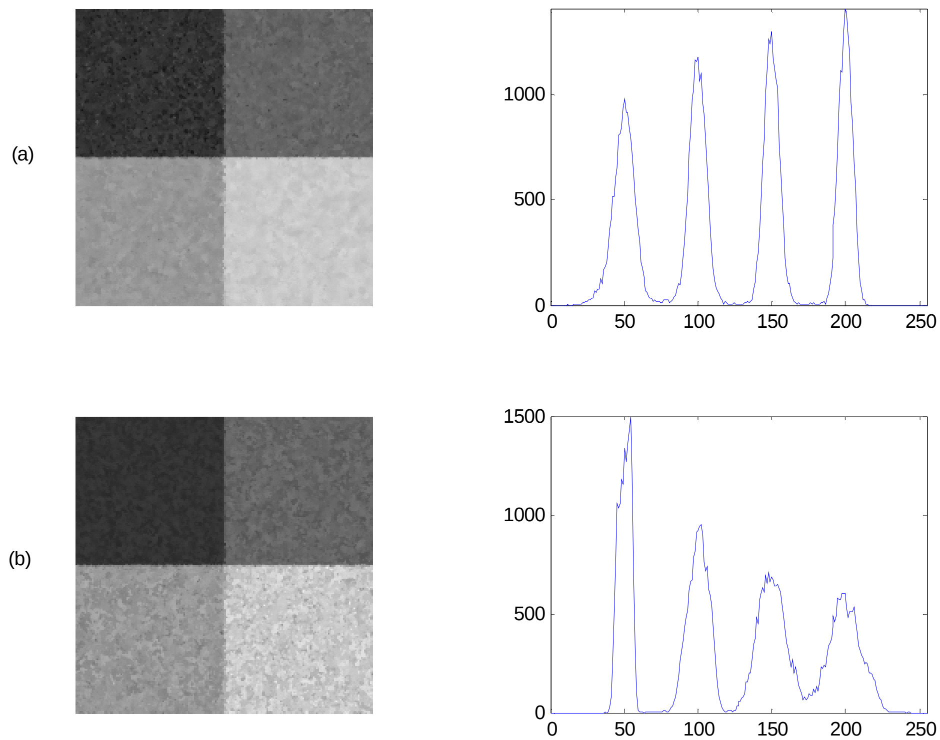

Figure 4.6 Images and histograms filtered with ANF over (a) simulated Gaussian white and (b) multiplicative speckle noises

Finally, the results produced by the ANF were analyzed using the MSE in Equation (4.20). Table 4.1 summarizes the MSE values. The results show that the filter provided good noise reduction and less blurring edge features on the images corrupted by both Gaussian white and multiplicative speckle noises, but a better result was yielded on the image corrupted by Gaussian white noise than multiplicative speckle noise. This is because the filtering algorithm is based on the correct noise model, and the noise model used in Equation (4.9) was about Gaussian film-grain noise. It implies that if the correct noise characteristics are given, the filter would provide good noise reduction while preserving edge features.

Images	Noise	Filtered	Filtered/Noise
Gaussian	637.5790	39.2391	6.15 %
Speckle	732.3999	75.4480	10.3 %

Table 4.1 MSE values for the noisy image and the results of filtering

4.3 Gaussian Mixture Density Estimation

Expectation Maximization (EM) algorithm (Dempster et al., 1977) is used to estimate the PDF of an observed image. In order to model the PDF of the image, Gaussian mixture model (GMM) is often used. The PDF of the image is modeled as weighted sum of a number of Gaussian distributions. A Gaussian density function is given by:

$$\Pr(y) = \frac{1}{\sqrt{2\pi\sigma^2}} \mathrm{e}^{-\frac{(y-\mu)^2}{2\sigma^2}} \tag{4.21}$$

with the mean μ and the variance σ^2. y is an observed gray value. A weighted sum of K Gaussian densities is then:

$$g(y) = \sum_{k=1}^{K} \pi_k p_k(y; \mu_k, \sigma_k) \tag{4.22}$$

where $p_k(y;\mu_k,\sigma_k)$ are component densities , and π_k are mixture weights. Thus, a GMM presents each class of image as a linear combination of several Gaussian densities in the image. The linear combination of Gaussian basis functions is used to form smooth approximations of arbitrarily shaped densities.

The means, variances and mixture weights of all Gaussian functions together parameterize the complete Gaussian mixture density. These parameters are collectively represented by the following notation:

$$\theta = \{\pi_k, \mu_k, \sigma_k\},\ k = 1, \cdots, K \tag{4.23}$$

The mixture weights satisfy the following constraint:

$$\sum_{k=1}^{K} \pi_k = 1 \tag{4.24}$$

We compute the parameters of the model by maximizing the log-likelihood of the joint probability density of y and x. Now x is unobserved, thus we try to estimate the marginal density of x

$$\sum_{x} g(y, x; \theta) \tag{4.25}$$

and then apply the maximum likelihood (ML) method. In order to do that, assume we have a guess θ' of the value of the parameters, and consider a series of observed feature vectors of $Y = \{y_1, \cdots, y_N\}$. Thus if we are able to construct a function $Q(\theta, \theta', Y)$ that estimates the log-likelihood of y given the guess θ' of the parameters and the observed feature vectors on y, then we can find a new estimate of the parameters that maximize Q. This procedure can be repeated to find a sequence of better approximations of θ. Such an iterative algorithm is called EM and can be summarized the following steps: First, the expectation-step constructs a log-likelihood function Q based on the previous guess θ'. Second, the maximization-step maximizes the log-likelihood function Q. For the expectation-step, we can choose Q as the expected value of the log-likelihood of y given the observed feature vectors, that is:

$$
\begin{aligned}
Q(\theta, \theta', Y) &= E\left[\sum_{i=1}^{N}\sum_{k=1}^{K} \log(g(x_i^k, y_i; \theta) \mid Y\right] \\
&= \sum_{i=1}^{N}\sum_{k=1}^{K}\sum_{x} \log(g(x_i^k, y_i; \lambda)) g(x_i^k \mid y_i; \theta') \\
&= \sum_{i=1}^{N}\sum_{k=1}^{K}\sum_{x} x_i^k \log(\pi_k p_k(y_i; \mu_i', \sigma_i')) g(x_i^k \mid y_i; \theta') \\
&= \sum_{i=1}^{N}\sum_{k=1}^{K} < x_i^k > \log(\pi_k p_k(y_i; \mu_i', \sigma_i'))
\end{aligned}
$$

where,

$$
\begin{aligned}
< x_i^k > &= \sum_x x_i^k g(x_i^k \mid y_i; \theta') \\
&= \frac{\sum_x g(y_i \mid x_i^i; \theta') g(x_i^k) x_i^k}{g(y_i; \theta')} \\
&= \frac{\pi_i' p_k(y_i; \mu_i', \sigma_i')}{\sum_{k=1}^K g(y_i \mid x_i^k; \theta') g(x_i^k)} \\
&= \frac{\pi_i' p_k(y_i; \mu_i', \sigma_i')}{\sum_{k=1}^K \pi_i' p_k(y_i; \mu_i', \sigma_i')}
\end{aligned}
\tag{4.26}
$$

Then we have to optimize Q using the following Lagrange target function:

$$
L = \sum_{i=1}^N \sum_{k=1}^K < x_i^k > \log(\pi_k p_k(y_i; \mu_k, \sigma_k)) + \lambda(1 - \sum_{k=1}^K \pi_k) \tag{4.27}
$$

where λ is the Lagrange multiplier. Taking derivative of L with respect to the parameters π_k, μ_k and σ_k, and recalling a weight constraint in Equation (4.24), we can get the following formulas:

$$
\begin{aligned}
&\frac{\partial Q}{\partial \pi_k} = \sum_{i=1}^N \frac{< x_i^k >}{\pi_k} - \lambda = 0 && \Rightarrow \hat{\pi}_k = \frac{\sum_{i=1}^N < x_i^k >}{N} \\
&\frac{\partial Q}{\partial \mu_k} = \sum_{i=1}^N \frac{< x_i^k > (y_i - \pi_k)}{\sigma^2{}_k} = 0 && \Rightarrow \hat{\mu}_k = \frac{\sum_{i=1}^N < x_i^k > y_i}{\sum_{i=1}^N < x_i^k >} \\
&\frac{\partial Q}{\partial \sigma_k} = \sum_{i=1}^N \frac{< x_i^k > [(y_i - \pi_k)^2 - \sigma^2{}_k]}{\sigma^3{}_k} = 0 && \Rightarrow \hat{\sigma}_k^2 = \frac{\sum_{i=1}^N < x_i^k > (y_i - \hat{\mu}_k)^2}{\sum_{i=1}^N < x_i^k >}
\end{aligned}
\tag{4.28}
$$

These formulas give us new estimation for θ given the current estimation θ' and the observation Y.

The EM algorithm is guaranteed to find a local maximum likelihood model regardless of the initialization, but different initialization can lead to different local maximum (Dempster et al., 1977). In this study, we set the initial parameters based on the maximum intensity value of the observed image as follows:

$$\begin{aligned} \pi_k &= \frac{k}{0.5K(K+1)} \\ \mu_k &= \frac{(k-1)M}{K} + \frac{M}{2K} \\ \sigma_k &= M \end{aligned} \tag{4.29}$$

where M is the maximum intensity value of the observed image and K is the number of Gaussian mixture densities.

Gaussian mixture densities of the images filtered with the ANF in Section 4.3 were estimated to verity the EM algorithm. Figure 4.7 shows the estimated Gaussian mixture density functions (red) in comparison of the original histograms (blue) derived from the filtered images shown in Figure 4.6. Table 4.2 summarizes the numerical values of the derived Gaussian mixture parameters.

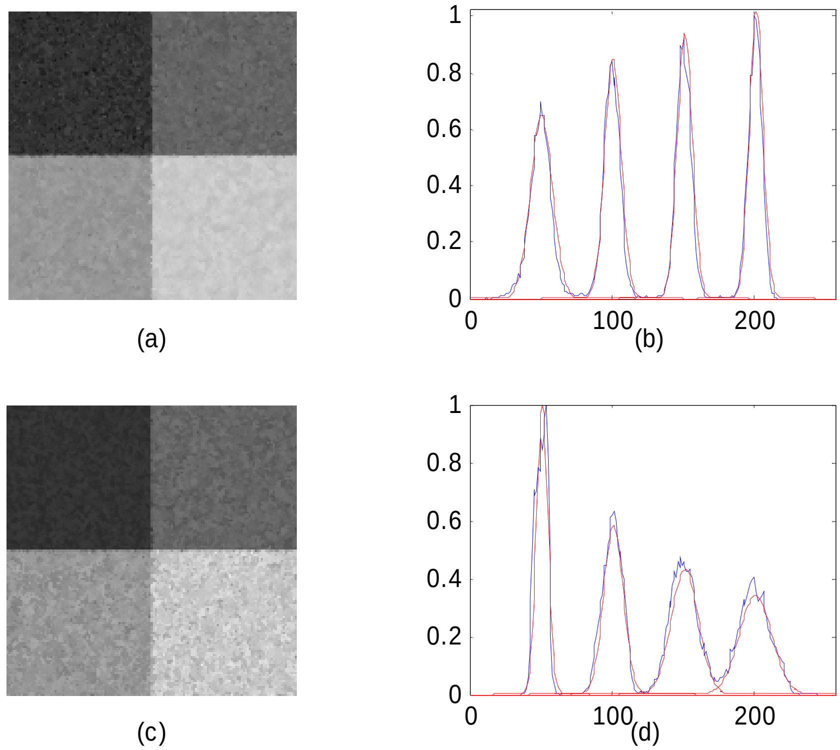

Figure 4.7 Examples of Gaussian mixture density estimation

Regions	Gaussian			Speckle		
	Weight	Mean	Variance	Weight	Mean	Variance
1	0.251561	49.434998	59.762581	0.250363	49.950577	15.893703
2	0.249173	99.546959	34.284313	0.250571	99.929138	47.120289
3	0.250614	149.868866	28.458136	0.256316	149.845215	89.353882
4	0.248652	199.922546	23.641296	0.242748	199.403946	128.545135

Table 4.2 The derived Gaussian mixture density values

4.4 Conditional Probability Density Estimation

Fuzzy c-means clustering (FCM) is a data clustering technique in which each data point belongs to a cluster to some degree that is specified by a membership grade. This technique was originally introduced by Bezdek (1984) as an improvement on earlier clustering methods (e.g., ISODATA). It provides a method that shows how to group data points that populate some multidimensional space into a specific number of different clusters. The fuzzy membership function produced by this FCM algorithm serves as a class-conditional probability density to a Bayesian image segmentation that produces the final segmentation results.

Let $Y = \{y_1, y_2, ..., y_n\}$, be a finite subset of R^d, the d-dimensional real number vector space (i.e., where two features are used for clustering, $d = 2$). Let the integer c, $n \geq c \geq 2$, denote the number of fuzzy subsets. Thus, a fuzzy c-partition of Y can be represented by a $(c \times n)$ matrix U in which each entry of U, denoted by u_{ik}, satisfies the following two constraints:

$$u_{ik} \in [0,1] \text{ and } \sum_{i=1}^{n} u_{ik} = 1, \text{ for all } k \tag{4.30}$$

The resulting matrix is shown in Figure 4.8. The value u_{ik} corresponding to the entry at the location (i,k) represents the membership value of the kth pixel for class i. All the entries in a given column must sum to one as specified in Equation (4.30).

	1	2	3	$\cdots$	n
1	u_{11}	u_{12}	u_{13}		u_{1n}
2	u_{21}				
3	u_{31}				
$\vdots$					
c	u_{c1}				u_{cn}

Figure 4.8 FCM membership matrix ($c \times n$)

The clustering criterion used in the FCM algorithm is based on minimizing the generalized within-group sum of square error function J_m:

$$J_m(U,V) = \sum_{k=1}^{n}\sum_{i=1}^{c} u_{ik}{}^{m}(y_k - v_i)^2, \qquad \text{for } 1 \le m < \infty \tag{4.31}$$

where $V = (v_1, v_2, ..., v_c)$ is the vector of cluster centers with $v_i \in R^d$, and m is the membership weighting exponent. For $m > 1$ and $y_k \neq v_i$, a local minimum of J_m is achieved under the following circumstance:

$$u_{ik} = \frac{1}{\sum_{j=1}^{c}\left(\frac{|y_k - v_i|}{|y_k - v_j|}\right)^{\frac{2}{m-1}}} \qquad \text{for all } k \tag{4.32}$$

and the ith cluster mean v_i is calculated from:

$$v_i = \frac{\sum_{k=1}^{n} u_{ik}{}^{m} y_k}{\sum_{k=1}^{n} u_{ik}{}^{m}} \qquad \text{for all } i \tag{4.33}$$

The FCM algorithm starts with a set of initial guesses for the cluster centers, which are intended to mark the mean location of each cluster. Using these initial cluster centers, FCM assigns every data point a membership grade for each cluster. By iteratively updating the cluster centers and the membership grades for each data point using Equations (4.32) and (4.33), FCM iteratively moves the cluster centers to the right location within a data set. This iteration is based on minimizing Equation (4.31) that represents the distance from any given data point to a cluster center weighted by a membership grade of given data point. The pseudo-code used for the FCM algorithm is in Figure 4.9

Begin

Choose the number of cluster c, *the weighting exponent* m,

and the termination tolerance ε *;*

Initialize cluster means $v_i^{(0)}$ *;*

Do

Calculate new partition $U^{(t)}$ *using Equation* (*4.32*)*;*

Compute new cluster means $v_i^{(t)}$ *using Equation* (*4.33*)*;*

Until $(\|U^{(t)} - U^{(t-1)}\|) < \varepsilon$

End

Figure 4.9 Algorithm for the FCM clustering

The membership weighting exponent m controls the relative weights placed on each of the squared errors. As m becomes closer to 1, the solution of the FCM procedure converges to hardness or crispness (i.e., the membership values become closer to 1 or 0, respectively), while the greater the value of m, the fuzzier the membership assignments will be (i.e., the membership values for all clusters are close to each other). The FCM literatures (Bezdek et al., 1984 and Cannon et al., 1986) suggested that, for most data, the choice of m value in the interval [1.3, 3.0] give a valid clustering result.

The performance of the FCM algorithm depends on the selection of the number of clusters and their initial values. If a good initial set of cluster centers that are close to the actual final cluster centers can be found, the FCM algorithm will converge very constantly and the processing time can be drastically reduced. We find the number of clusters and their initial values using the Gaussian mixture density estimation described in section 4.2 in such a way that the results of the analysis with different numbers of clusters are compared with each other.

4.5 Prior Probability Density Estimation

Image segmentation is an ill-posed problem (Bertero et al., 1988) that fails to satisfy one or more of the following criteria: its solution (a) exits, (b) is unique, and (c) depends on the initial data. Standard regularization techniques are normally used for solving the ill-posed problems (Poggio et al., 1985) and lead to satisfactory solutions of image segmentation, but cannot deal effectively and directly with a few general problems, such as discontinuities and fusion of information from multiple modules (Marroquin et al., 1987). An alternative way for solving ill-posed problems is to restrict the class of admissible solutions by introducing suitable a prior knowledge in terms of an appropriate probability distribution. The GRF model is appropriate for the prior information in image segmentation because they can specify the local and global properties of regions.

Let $S = \{(i, j) \mid 1 \le i, j \le m\}$ be the $m \times m$ square lattice and $s = (i, j)$ be each site on the lattice S, then $y = \{y_s \mid s \in S\}$ and $x = \{x_s \mid s \in S\}$ denote the observed image and the corresponding labels of the observed image, respectively. A collection of subset of S defined as $\eta = \{\eta_s \mid s \in S, \eta_s \subseteq S\}$ is a neighborhood system if and only if η_s the neighborhoods of a pixel s are such that $s \notin \eta_s$, and if $s' \in \eta_s$, then $s \in \eta_{s'}$ for any $s \in S$. A neighborhood structure for η^2, called the 2nd order neighborhood system and its pair-wise clique types, $\mathrm{B} = \{\beta_1, \beta_2, \beta_3, \beta_4\}$ are shown in Figure 4.10.

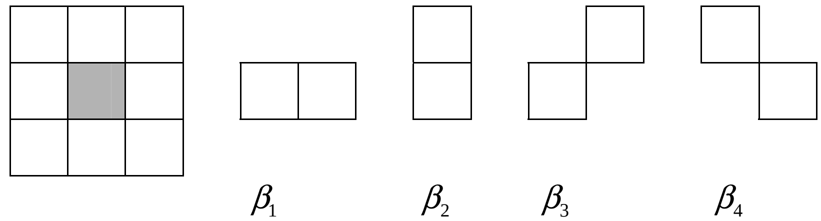

Figure 4.10 η^2 - neighbor system and its pair-wise clique types

A random field $x = \{x_s \mid s \in S\}$ is a GRF with respect to η if and only if its configurations obey a Gibbs distribution. A Gibbs distribution takes the following form:

$$\Pr(x) = \frac{1}{Z}\exp\left[-U(x)\right] \tag{4.34}$$

where

$$Z = \sum_{x \in X} \exp\left[-U(x)\right] \tag{4.35}$$

is a normalizing constant called the partition function, and $U(x)$ is the energy function. The energy function is given by:

$$U(x) = \sum_{c \in C} V_c(x) \tag{4.36}$$

is a sum of clique potentials $V_c(x)$ over all possible cliques C. The value of $V_c(x)$ depends on the local configuration on the clique c. The most general form of energy function $U(x)$ based on a pair-wise clique potential function in Figure 4.9 is expressed in the following expanded form:

$$U(x) = \sum_{c \in C} V(x, x') = \sum_{c \in C} \beta \delta(x, x') \tag{4.37}$$

where c represents a pair-site clique function, $\beta (> 0)$ is a set of pair-wise clique potential parameters and $\delta(a,b)$ is a step function defined as

$$\begin{aligned} &\delta(a,b) = 1 \qquad \text{if } a = b \\ &\delta(a,b) = 0 \qquad \text{otherwise} \end{aligned} \tag{4.38}$$

The choice of the coefficients β of the function shown in Equation (4.37) is a major topic in GRF modeling. When all the coefficients of the energy function are defined, the model is completely specified. The GRF model for the prior distribution on the observed image is in fact both homogeneous and isotropic in an appropriate sense, even if this is not the case for the posterior distribution (Geman and Geman, 1984). When a random model is isotropic (i.e., rotation invariant), the coefficients β of the prior energy function $U(x)$ may take the same values.

A GRF describes the global properties of an image (i.e., the label given to a specific pixel is affected by the labels given to all other pixels) in terms of the joint distribution of classes for all pixels. The practical value of the theorem is that it provides a simple way of specifying the joint probability. One can specify the joint probability $P(x)$ by specifying the clique potential functions $V_c(x)$ and chooses appropriate prior information about interactions between labels.

4.6 Posterior Probability Density Estimation

Once the class-conditional energy function of the observed feature vectors y given the labels x and the prior energy function of the labels x are modeled by means of FCM and GRF, respectively, the current trend is to use the Bayesian formulation in Equation (4.1) to construct either the posterior probability density or the posterior energy function and then to perform labeling by maximizing this posterior probability density or minimizing the posterior energy function by Equation (4.5).

The idea described in Section 4.5 is mainly designed to achieve a smooth interpolation of the observed image. In practice, the patterns in an image are only piece-wise continuous. In other words, discontinuities are naturally to be found within image. In such cases, the use of a smooth interpolation operation may smear these discontinuities (i.e., edges between different regions), causing over-smoothing.

4.7 Energy Minimization

Once the posterior energy and the associated parameters β have been determined, the next step is to find the MAP estimate using Equation (4.5). The MAP procedure for solving the labeling problem presents a considerable computational challenge. Marroquin et al. (1987) proposed a pixel labeling, but avoided the computational difficulties inherent in MAP estimation by introducing to minimize the following segmentation error ε. Let x^* be the true labeling, then a labeling $\hat{x}$ is sought which minimizes:

$$\varepsilon = \frac{1}{m^2}\sum_{i,j=1}^{m^2}\left[1-\delta(x_s{}^* - \hat{x}_s)\right] \tag{4.39}$$

which is the number of elements that are not classified correctly in the labeling $\hat{x}_s$ since $\delta(a) = 1$ if $a = 0$ and 0 otherwise. The labeling that minimizes the segmentation error ε can be shown to maximize the marginal posterior distribution so that the label $\hat{x}_s$ is taken at pixel s to be the one that satisfies:

$$\Pr(\hat{x}_s \mid y_s) \geq \Pr(x_s \mid y_s),\ \text{for all } x_s \tag{4.40}$$

The point of departure of the MPM is the manner in which this marginal conditional distribution is computed by counting the number of times each label is present at each pixel in a series of configurations. This approximation can be expressed by:

$$\hat{\Pr}(x_s \mid y_s) = \frac{1}{n-k}\sum_{i=k+1}^{n}\delta(x_s - g) \tag{4.41}$$

where g represents the possible label belonging to label set.

The parameters k and n are chosen heuristically; k is the number of iterations needed for the process to reach a steady state and n is selected for accurate estimation at acceptable computational cost. For example, in the case of a two-label segmentation, if one choose $k = 20$ and $n = 120$, and if a pixel x is labeled 1 on 20 occasions and labeled 2 on 60 occasions, then the probability $\Pr(x = 1 | y)$ will be $20/(120 - 20) = 0.2$, and $\Pr(x = 2 | y)$ will be $60/(120 - 20) = 0.6$. The pixel x will then be segmented as label 2 according to Equation (4.40). It is clear that the MPM algorithm requires more computation than the iterated conditional modes algorithm, but is much less than that required by the simulated annealing algorithm. The MPM algorithm is given in Figure 4.11

Begin

1. *Set recording interval* k *and* n *in Equation (4.41);*
2. *Initialize* x *by choosing* x_s *as the label* g *that maximizes the conditional energy in Equation (4.32);*
3. *For all pixels*
    i. *Perturb* x_s *by labels* $x_{s'}, s' \in \eta_s$ *that is randomly selected from the labels in the neighborhood system in Figure 4.10;*
    ii. *Compute a energy difference* $\Delta = U(x_s | x_{s'}) - U(x_{s'} | x_s)$ *in terms of Equation (4.32) and (4.37), respectively;*
    iii. *if* $\Delta > 0$, *replace* x_s *by* $x_{s'}$*;*
    iv. *else if* $\exp(\Delta) \geq \text{random}[0,1]$, *replace* x_s *by* $x_{s'}$*;*
4. *Repeat step 3* n *times, and save configuration from* x^{k+1} *to* x^k*;*
5. *For each pixel* s, *compute probability* $\hat{\Pr}(x_s | y_s)$ *using Equation (4.41);*
6. *For each pixel* s, *choose* $\hat{x}_{map}$ *according to Equation (4.40);*

End

Figure 4.11 Maximizer of the posterior marginals segmentation algorithm

The test images are the same as those described in Section 4.2 and 4.3. The results of the MPM segmentation and their confusion matrices are shown in Figure 4.12 and Table 4.3, respectively. For the MPM algorithm, only pair-site neighborhood systems (i.e., clique $c = 2$) were considered, and the isotropic assumption (i.e., all β are 0.5) was used. The MPM is better to the image corrupted with the Gaussian white noise than the image corrupted with the multiplicative speckle noise. This means that the characteristics of Gaussian white noise are much close to the characteristics of film-grain noise in Equation (4.9) than the multiplicative speckle noise model. If the characteristics of the noise model are correctly defined, the MPM will produce the better results.

Figure 4.12 Synthetic image (left), MPM segmented image from Gaussian white noise (middle) and MPM segmented image from multiplicative speckle noise (right).

# classes	1	2	3	4	User %
[Image corrupted with Gaussian white noise]					
1	16359	0	20	0	99.88
2	9	16369	3	6	99.89
3	16	0	16359	0	99.90
4	0	15	2	16378	99.90
Producer %	99.85	99.91	99.85	99.96	65536
Accuracy	99.8916		Kappa	0.998556	
[Image corrupted with multiplicative speckle noise]					
1	16384	0	20	0	99.88
2	0	16382	0	127	99.23
3	0	2	16364	9	99.93
4	0	0	0	16248	100.00
Producer %	100.00	99.99	99.88	99.17	65536
Accuracy	99.7589		Kappa	0.996785	

Table 4.3 Confusion matrices of two test images

4.8 Segmentation Post-processing

4.8.1 Connected Component Labeling

A segmented image often contains too many regions as a result of either non-optimal parameter setting or significantly complex scene (Figure 4.13). A simple post-processing is based on visual interpretation and removes the small, isolated regions that cannot be merged with any adjacent region according to the originally applied segmentation algorithm. These small regions are usually not significant in further processing and can be considered as segmentation noise (Figure 4.13 a). The removal procedure of small regions implemented in this study is as follows:

1. Define Object and background regions along the object boundary based on visual interpretation of the segmented image (Figure 4.13 a).

2. Replace the values of each region with either 0 or 1. – object regions to 1 and others to 0 (Figure 4.13 b).
3. Calculate the size of each region in the binary image based on 8-connectivity and select the maximum size $O_{\max}$ of object regions and the maximum size $B_{\max}$ of background regions.
4. Replace the value of object regions smaller than $O_{\max}$ with the value of background regions and vice versa (Figure 4.13 c).

1	3	3	3	3
1	1	3	3	3
2	1	1	2	2
2	1	1	2	4
1	1	2	2	4

(a)

0	1	1	1	1
0	0	1	1	1
1	0	0	1	1
1	0	0	1	0
0	0	1	1	0

(b)

0	1	1	1	1
0	0	1	1	1
0	0	0	1	1
0	0	0	1	1
0	0	1	1	1

(c)

Figure 4.13 Segmentation post-processing: (a) segmented image with object pixels (2, 3 and 4) and background pixels (1 and 2), (b) merged (3 and 4), binary image and (c) complete object and background image.

4.8.2 Boundary Extraction

An eight neighborhood scan of the segmented, binary image is used for locating region boundaries. Each object pixel of the image is scanned by a 3×3 neighborhood window, and then makes the center pixel as a boundary pixel if all pixels in the window are same. A pseudo-code for the algorithm and its example are in Figure 4.14 and Figure 4.15, respectively:

```
Begin
    input a segmented, black and white image, g(i, j)
    initialize a boundary map, f(i, j) = 0
    for i, j = 1 : N
      if ((g(i, j) == 1 & &
          g(i, j) ≠ g(i−1, j−1) || g(i, j) ≠ g(i−1, j) || g(i, j) ≠ g(i−1, j+1) ||
          g(i, j) ≠ g(i, j−1) || g(i, j) ≠ g(i, j) || g(i, j) ≠ g(i, j+1) ||
          g(i, j) ≠ g(i+1, j−1) || g(i, j) ≠ g(i+1, j) || g(i, j) ≠ g(i+1, j+1))
          f(i, j) = 1;
      else
          f(i, j) = 0;
    end
End
```

Figure 4.14 Boundary detection algorithm for a object-background image

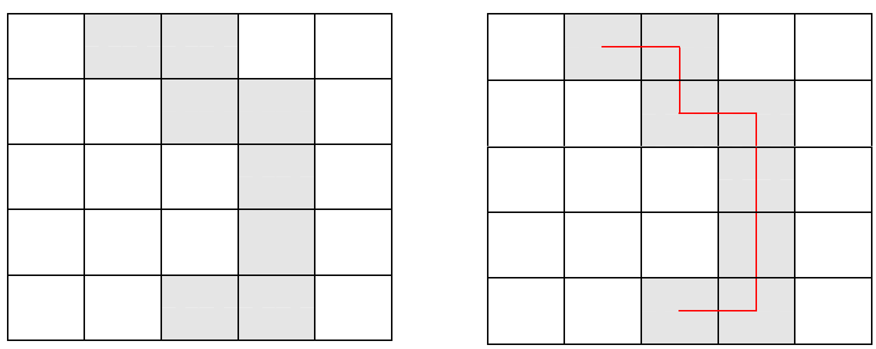

(a) (b)

Figure 4.15 Object boundary pixels (grey) detected based on eight-connectivity (a) and its vectorized boundary (b)

The boundary pixels are in the form of arrays of square data units and may need to be changed into lines for further analytical purposes. The spatial location of each boundary pixel is implicitly defined due to the pixel resolution. Lines connected by boundary pixels are recognized as such, however, raster structures cannot identify the correct shape of linear features. In contrast, vector structures are able to explicitly identify the correct shape of linear features because these features are composed simply as a series of one or more coordinate points. As a result, the spatial accuracy of vector representations is better than raster representations. In this study, the center coordinates of boundary pixels are calculated, and then simply connected together within the ArcInfo GIS environment.

4.9 Summary

The development of image segmentation algorithms based on an adaptive Bayesian approach is the second theme of this dissertation. The adaptive Bayesian framework to image segmentation developed in Chapter 4 relied upon the use of the prior and conditional probability density functions. The Markov random field (MRF) model was successfully replaced by the fuzzy c-means clustering (FCM) technique, which avoids the difficulty in estimating the conditional probability $\Pr(y \mid x)$ of the observed intensity values y given the labels x. Initial values derived from the Gaussian mixture model (GMM) made another contribution to the Bayesian framework, resulting in more reliable results than randomly chosen initial values. A simple synthetic image has been used for verifying the algorithm. Results have been presented that demonstrate the effectiveness of the algorithm in segmenting the synthetic image, resulting in more than 99.8% accuracy when noise characteristics are correctly modeled. The algorithms have been implemented using the C-programming language.

The following chapter will provide a comparison of our algorithm and recently developed coastline extraction algorithm (Liu and Jezek, 2003) and demonstrate the application results on the Argon DISP image mosaic created in Chapter 3.

CHAPTER 5

COASTLINE MAPPING OF ANTARCTICA

5.1 Introduction

The Antarctic coastline is either rock or ice wall, or ice shelf terminus that is adjoined by sea ice covered or open ocean ice. Sea ice is any form of ice found at sea which has originated from the freezing of sea water. Fast ice is sea ice in a sheet permanently attached to the coastline and may extend a few meters or several hundred kilometers from the coastline. Although icebergs and ridges within fast ice can have high relief, fast ice is generally fairly flat.

In spite of their importance as a potential indicator of global climate change, the long-term behavior of the Antarctic coastline over continental scales was largely unknown. Recently, many Antarctic researchers have studied changes in the Antarctica coast (Kim et al., 2001; Bindschadler and Rignot, 2001; Shepard et al., 2001; Rignot, 1998; and Vaughan and Doake, 1996), but their research was limited to a specific, local sector of Antarctica. An historical image mosaic of the entire Antarctic coast (see Figure 3.9) created from the DISP data acquired during the early 1960s becomes a resource for measuring the changes of the Antarctic coastline over continental scales.

The purpose of this chapter is to extract the entire coastline of Antarctica using the historical DISP image mosaic created in Chapter 3. Liu and Jezek (2003) presented a local dynamic thresholding (LDT) approach to extracting the Antarctic coastline from 1997 SAR image data, in which ice margin mapping is relatively simple because the glacier ice appears substantially brighter than either seasonal or fast ice. At the processing stage, they used a Lee sigma filter and anisotropic diffusion operator to suppress the speckle noise and to enhance the coastline edges. At the segmentation stage, a locally adaptive thresholding method is used to segment the SAR images into homogeneous glacier and ocean water regions, in which the Levenberg-Marquardt method is introduced to fit the bimodal Gaussian parameters and Canny edge detector is used to refine the observed histogram and to estimate reliable initial values for the bimodal Gaussian parameters. They successfully created two complete coastline maps (in 25-m and 100-m pixel resolutions) for the entire Antarctic coastal regions and surrounding islands.

A trimodal scheme was introduced in an attempt to extend the technique the DISP data, which were more difficult to interpret because there was very little contrast between glacier ice and fast ice and there was substantially more fast ice cover in 1963 than in 1997. The trimodal shceme did not successfully segment the DISP data when even light cloud cover was present (Figure 5.1) – possibly a problem associated with selecting regions that have low contrast boundary between glacier ice and fast ice. A more satisfactory segmentation resulting from the adaptive Bayesian approach developed in Chapter 4 is shown in Figure 5.1 (c).

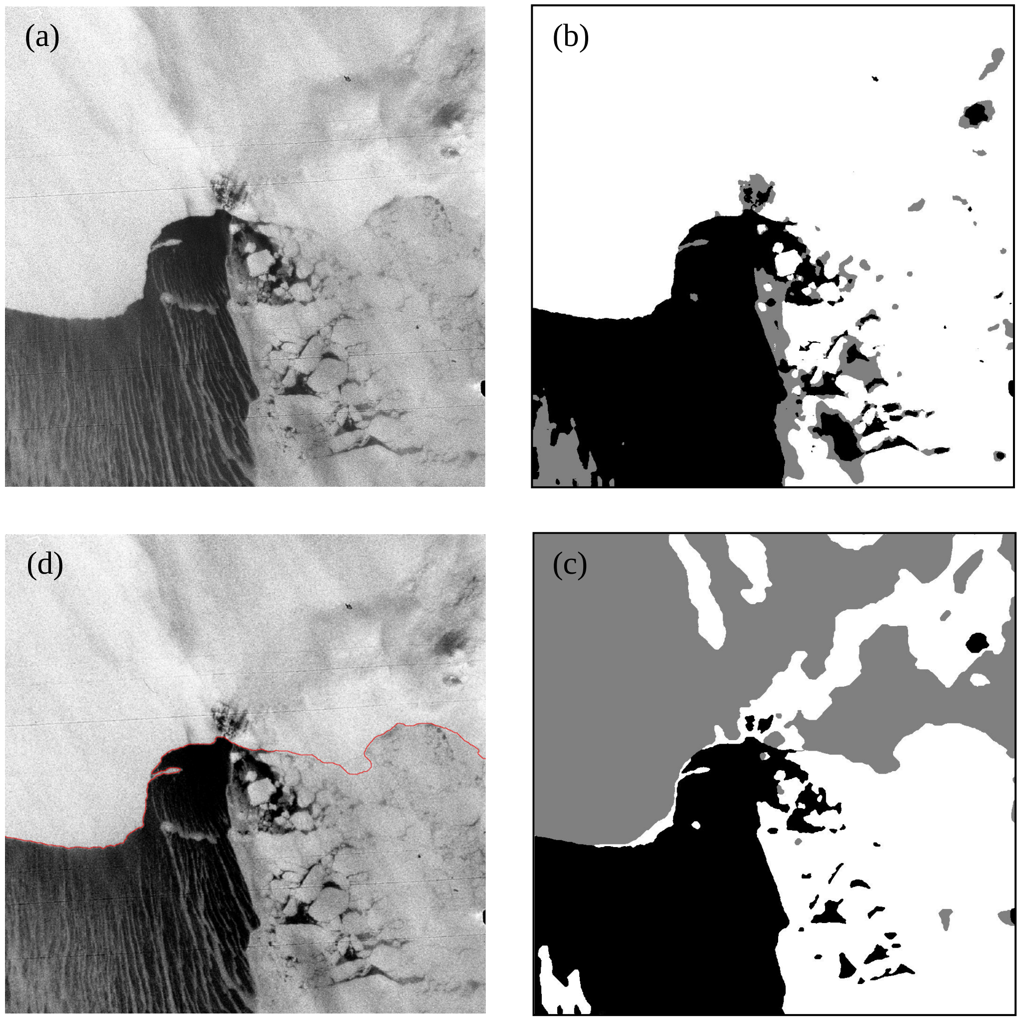

Figure 5.1 Comparison of trimodal LDT and adaptive Bayesian segmentation applied to DISP data: (a) original image; (b) trimodal LDT segmentation; (c) adaptive Bayesian segmentation; and (d) coastline extracted from (c).

In this study, the automated boundary detection software developed in Chapter 4 was applied to extract the entire coastline of Antarctica using the historical DISP image mosaic. In practice, there are also some difficulties in the use of the image mosaic. One of the major difficulties in trying to detect the Antarctic coastline is that more than 40% of the image mosaic contains significant cloud cover, especially in the west coastal areas of Antarctica. Another challenge is that much of cloud-free coastal areas are adjoined to fast ice. Fast ice is usually reformed and thickened yearly, so fast ice is similar to glacier ice in terms of the visible characteristics. Because of these similar characteristics between glacier and fast ice, it is not easy to differentiate the coastline from fast ice. Figure 5.2 illustrates a true-color Moderate-resolution Imaging Spectroradiometer (MODIS) image of the northwestern portion of the Ross Ice Shelf acquired on October 12, 2001. The image illustrates the difficulty in trying to differentiate the coastline from fast ice. Just to the left of center in this image there are several pieces of sea ice separating from the Ice Shelf. Beginning at the top of the image and running south are the Prince Albert Mountains, which mark the coastline with the Ross Sea, the body of water occupying the upper-right area of the image. Everything east of those mountains and south to Ross Island is fast ice. South and east of Ross Island is the Ross Ice Shelf.

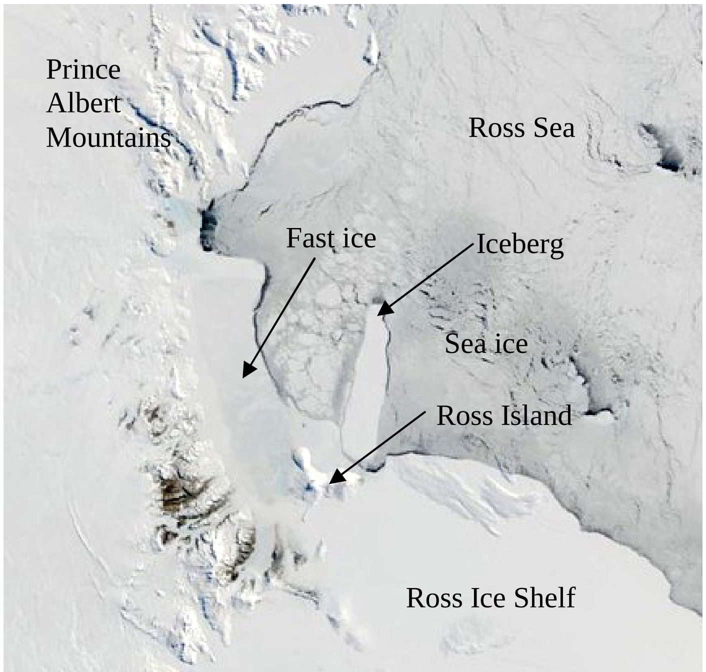

Figure 5.2 True-color MODIS image displaying the northwestern portion of the Ross Ice Shelf (Image courtesy Jacques Descloitres, MODIS Land Rapid Response Team at NASA GSFC at http://modis-land.gsfc.nasa.gov/)

To resolve some of these complexities, alternative criteria must be used in place of the automated boundary detection software. For example, if a scene is very complex due to combination of sea ice, fast ice, open water and glacier ice, then adaptive histogram equalization (AHE) may help enhancing details in the scene. AHE enhanced images may still not work with the boundary detection software because the AHE results in blob-like textures. AHE partitions an image into $N \times N$ subregions, and the histogram for each region is calculated. The histogram is used to perform local image enhancement.

For processing the entire image mosaic, the mosaic was first partitioned into a number of small image blocks (1024×1024) along the entire coast. Each small image block was then processed as described in Chapter 4. Five different examples of image scenes, such as glacier and open water, light cloud cover, glacier and fast ice, mountainous coastline, and mixed classes, are discussed in this chapter. In this manner, the entire coastline were extracted and assembled, and quality assessments of the extracted coastline were performed.

5.2 Case Studies

5.2.1 Glacier and Open Water

The coastline of large ice shelves, such as Ross Ice Shelf and Ronne-Filchner Ice Shelf, can be easily extracted by the automated boundary detection software, because the scenes normally have a simple combination of glacier, open water, and light cloud. Figure 5.3 shows the original image, ANF image, and corresponding histograms. The original image displays a part of Ross Ice Shelf $(177^{\circ}07'E, 77^{\circ}55'S)$. It was filtered by the ANF algorithm with parameters, $D = 3.3$, $\sigma_1 = 1$ and $\sigma_2 = 0$ described in Equation (4.9). Comparison of the two histograms shows that the ANF image provides effective noise suppression and retention of boundary sharpness.

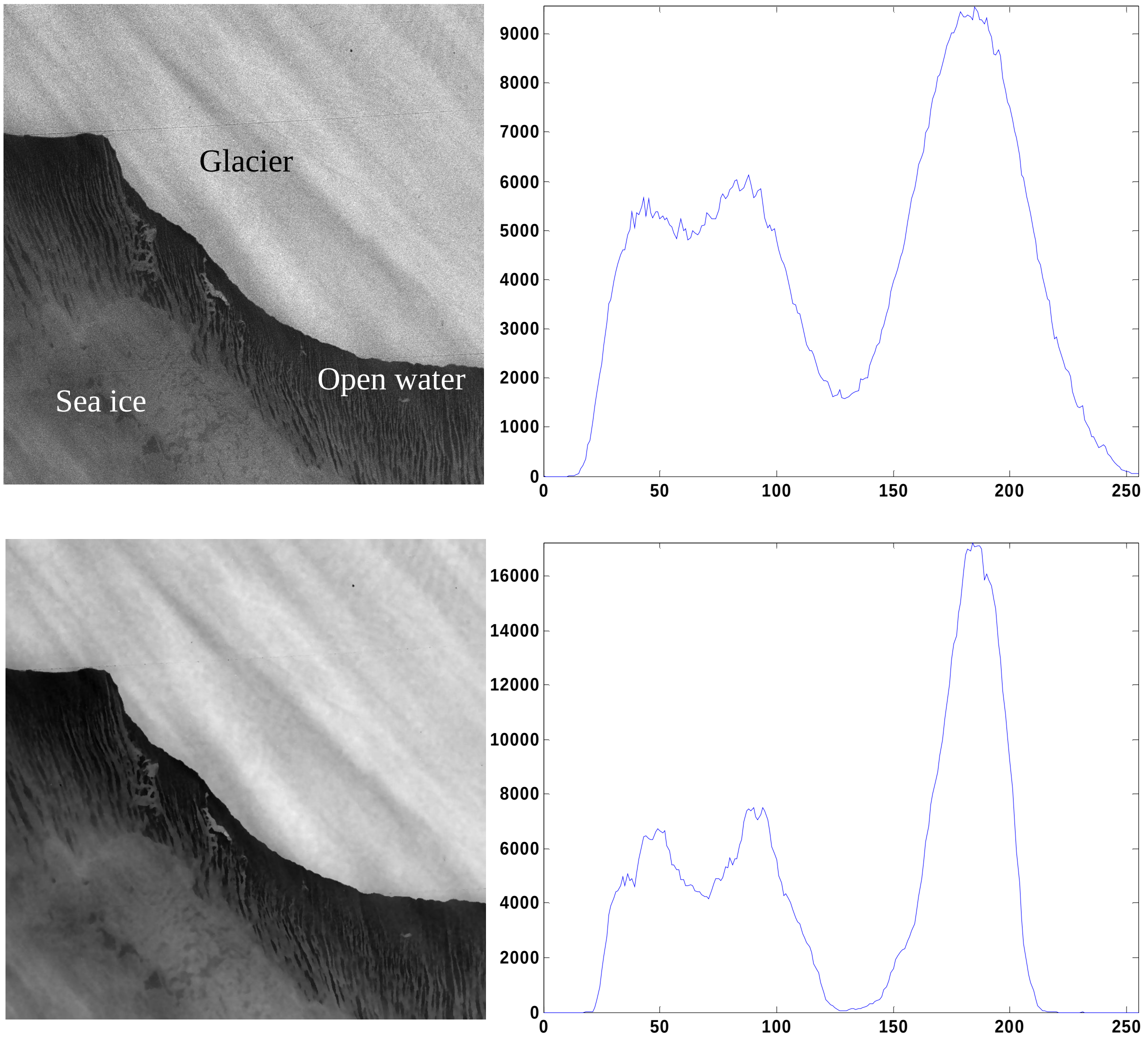

Figure 5.3 Original image (top), ANF image (bottom), and corresponding histograms

The original image clearly contains three different types of regions: glacier in white, open water in black, and sea ice and cloud in gray. So the number of classes was set to $k = 3$ for estimating the GMA of the ANF image. The estimated GMA and histogram of the ANF image are compared in Figure 5.4 The histograms were normalized by the maximum bin number of each histogram, so that they can be easily compared with each other.

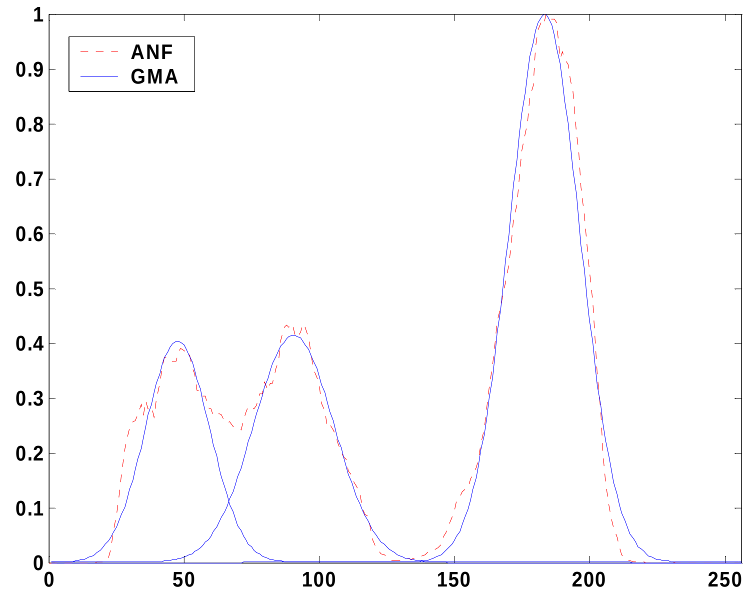

Figure 5.4 The GMA estimation (solid) and histogram (dashed) of the ANF image

Using the estimated GMA as initial values, the FCM was performed to compute the class-conditional energy function. As the minimization of FCM object functions shown in Figure 5.5, the minimization process with the GMA (solid) was almost flat and the processing time was drastically reduced, compared with the process with random initial values (dashed).

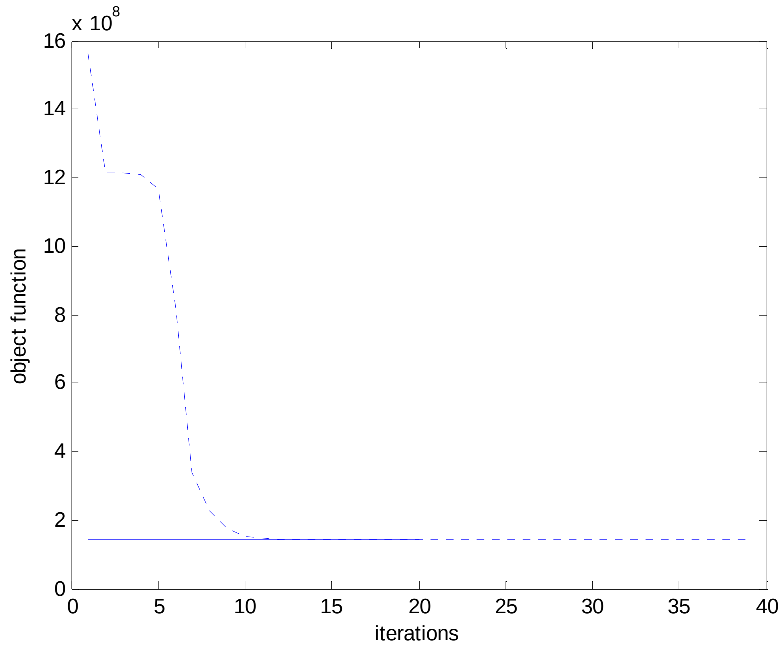

Figure 5.5 FCM Convergence rates of the GMA (solid) and random initial values

After estimating the FCM, the MPM procedure illustrated in Figure 4.11 was carried out with parameters, $k = 20$ and $n = 200$. The sequential procedures for extracting the coastline are shown in Figure 5.6. First, class 2 (gray) and 3 (white) were merged as object regions, and the others were merged as background regions. Second, background regions smaller than the maximum size (2) of background regions were eliminated (Figure 5.6 (b)), and object regions smaller than the maximum size (1) of object regions were eliminated (Figure 5.6 (c)). Figure 5.6 (d) shows the coastline extracted from Figure 5.6 (c).

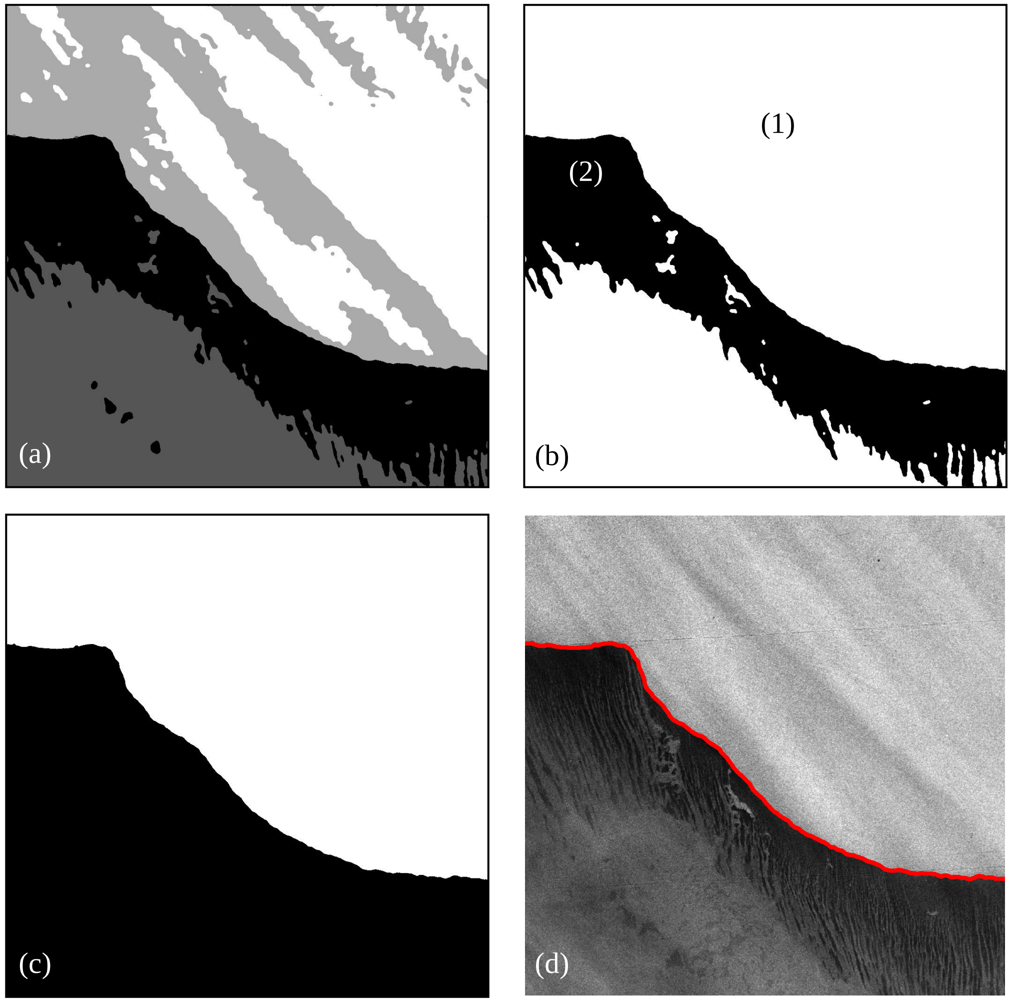

Figure 5.6 MPM segmentation and boundary detection: (a) MPM segmentation with three classes - glacier in white, cloudy glacier and sea ice in gray, and open water in black; (b) the binary image with a background region and all object regions; (c) the binary image with a object region and a background region; and (d) the original image overlaid with the boundary extracted from (c).

5.2.2 Light Cloud Cover

More than 40% of the image mosaic contains significant cloud cover, especially in the western sector of Antarctica. An example of light cloud-covered areas is shown in

Figure 5.7. The original image (top) displays a part of Jelbart Ice Shelf $(5^\circ 56' W, 70^\circ 16' S)$ and is completely covered by light cloud except the low-right corner. As the histogram shows, the statistics of the original image are nearly unimodal in shape, but three or four regions are recognized in the histogram of the ANF image (bottom), which was filtered with parameters, $D = 3.3$, $\sigma_1 = 1$ and $\sigma_2 = 0$.

In this case, two GMA estimations were carried out because the number of classes is ambiguous in the ANF image. The comparison between two GMA estimations and the histogram of the ANF image (Figure 5.8) shows that the GMA with three classes (blue) is systematically offset from the ANF histogram, but the GMA with four classes (black) is much close to the ANF histogram except for a very small bump at the bottom. Based on this interpretation, the FCM with four-class GMA was performed to compute the class-conditional energy function. During the process, the FCM was converged smoothly and the processing was terminated after 68 iterations. Figure 5.9 shows the comparison of the convergence rates between GMA and random initial values.

After the FCM processing of the ANF image, the MPM procedure was carried out with parameters, $k = 20$ and $n = 200$. The sequential procedures for extracting the coastline are shown in Figure 5.10. First, class 3 (bright gray) and 4 (white) were merged as object regions, and others were merged as background regions. Second, background regions smaller than the maximum size (2) of background regions were eliminated (Figure 5.10 (b)), and object regions smaller than the maximum size (1) of object regions were eliminated (Figure 5.110 (c)). Figure 5.10 (d) shows the original image overlaid with the boundary extracted from Figure 5.10 (c).

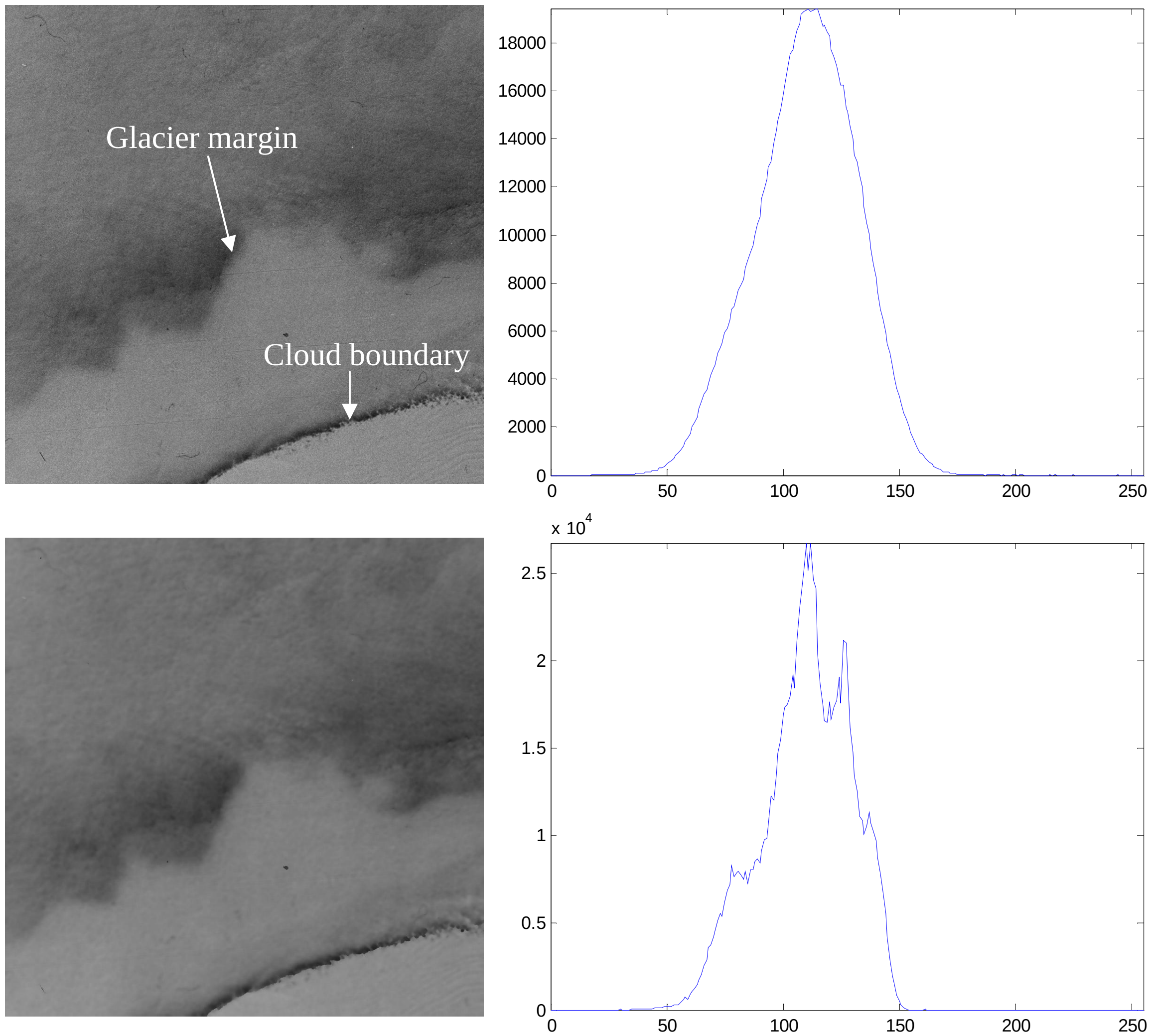

Figure 5.7 Original image (top), ANF image (bottom) and corresponding histograms

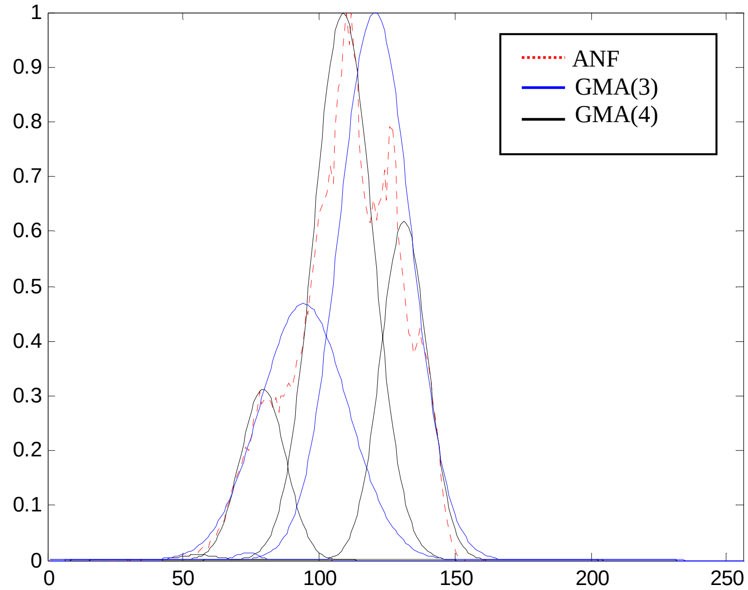

Figure 5.8 Two GMA estimations (blue and black) and histogram of the ANF image

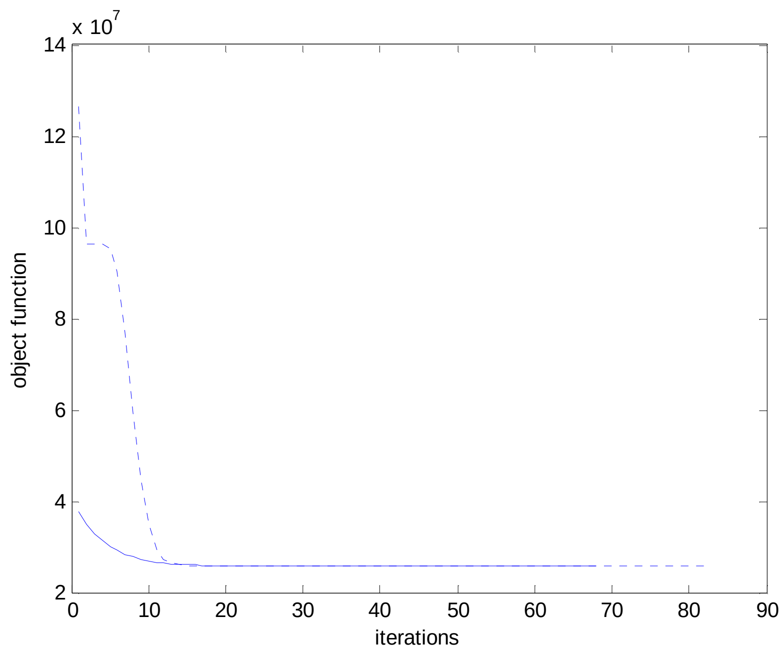

Figure 5.9 FCM Convergence rate of the GMA (solid) and random initial values (dashed)

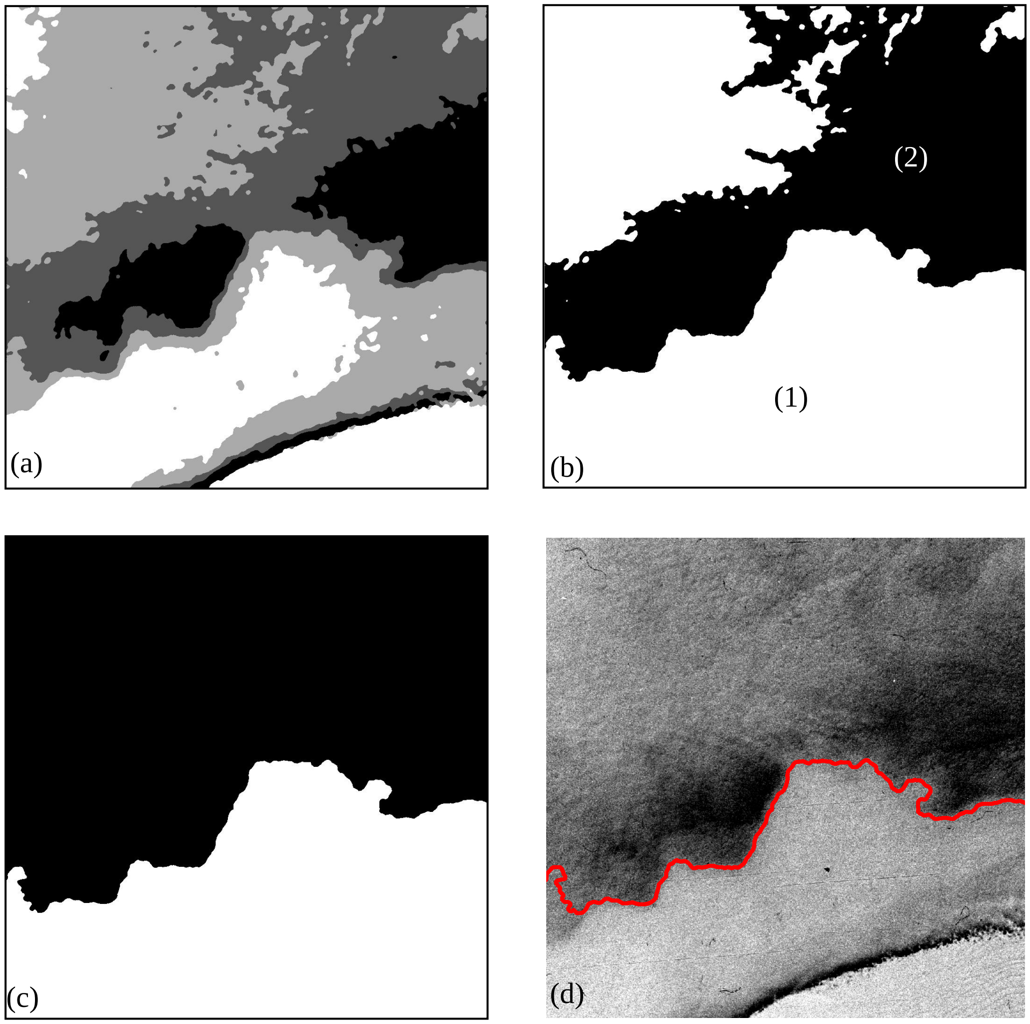

Figure 5.10 MPM segmentation and boundary detection: (a) MPM segmentation with four classes – cloudy glacier in white and bright gray, cloudy sea ice in bright and dark gray, and cloudy water in black; (b) the binary image with a background region and all object regions; (c) the binary image with an object region and a background region; and (d) the original image overlaid with the boundary extracted from (c).

5.2.3 Glacier and Fast Ice

Figure 5.11 (top) shows an example of the coastline obscured by fast ice, which is sea ice attached to the coastline. This image displays a part of Luitpold Coast $(32^{\circ}27'W, 77^{\circ}14'S)$. The coastline in the image is vertically located between glacier and fast ice. Because of more contrast between open water (dark) and fast ice than between glacier and fast ice, it is more difficult for the MPM algorithm to differentiate the coastline from fast ice. The histogram of the image (top) is a simple, bimodal distribution. However, the histogram of the ANF image (bottom) shows that the image is likely to have four different classes (i.e., glacier, water, sea ice, and fast ice) in the image. The estimated GMA is shown in Figure 5.12.

Based on the estimated Gaussian mixture approximations (GMA), the FCM computed the class-conditional energy function. Figure 5.13 shows that the initial values obtained from the Gaussian mixture estimation made the FCM algorithm converged smoothly and more rapidly than the random initial values. After the FCM process, the MPM procedure was carried out with parameters of $k = 20$ and $n = 200$. The sequential results are shown in Figure 5.14. First, class 4 (white) was labeled as object regions, and others were merged as background regions. Second, background regions smaller than the maximum size of background regions were eliminated (Figure 5.14 (b)), and object regions smaller than the maximum size of object regions were eliminated (Figure 5.14 (c)). Figure 5.14 (d) shows the original image overlaid with the boundary extracted from Figure 5.14 (c).

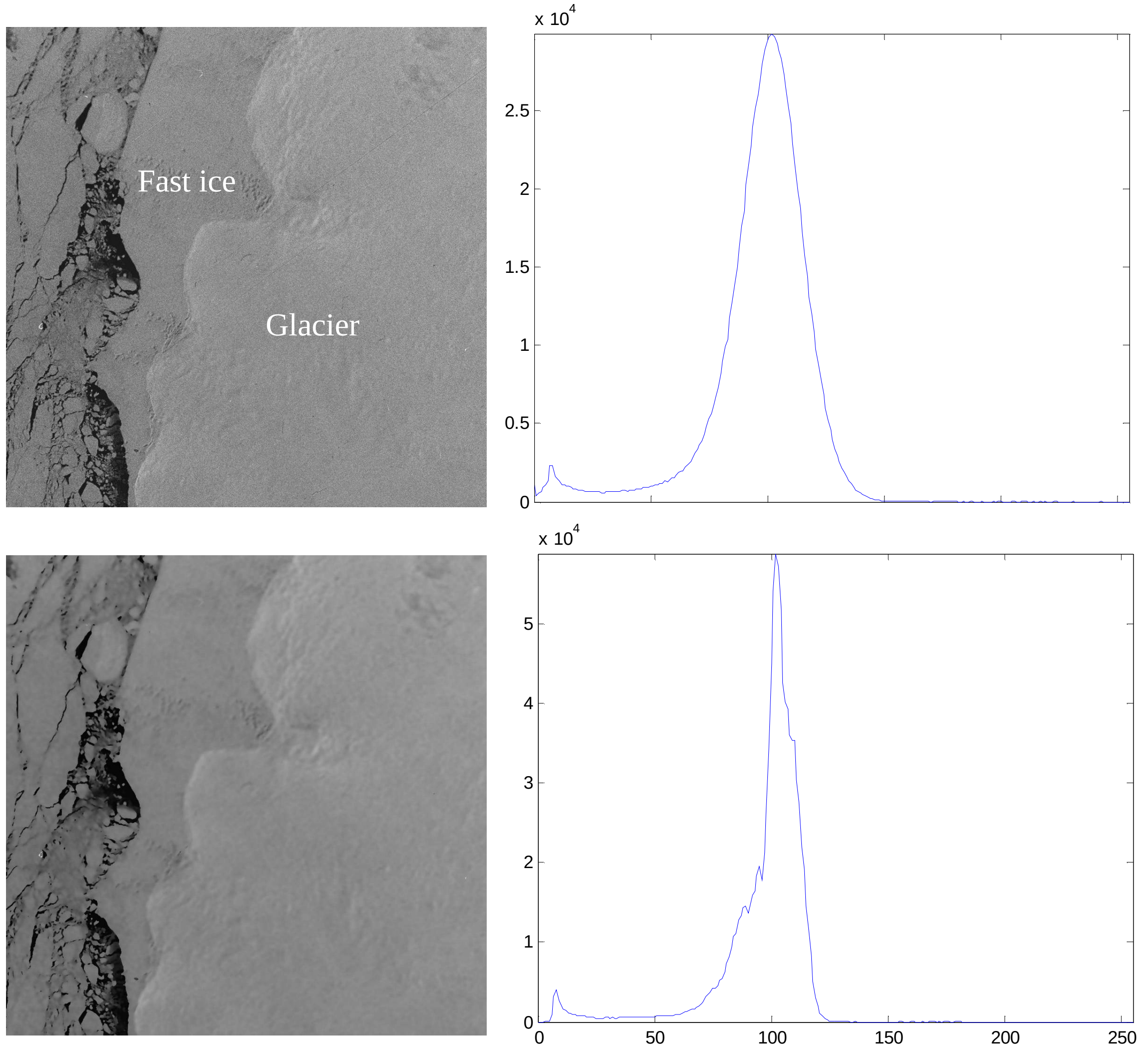

Figure 5.11 Original image (top), ANF image (bottom) and corresponding histograms

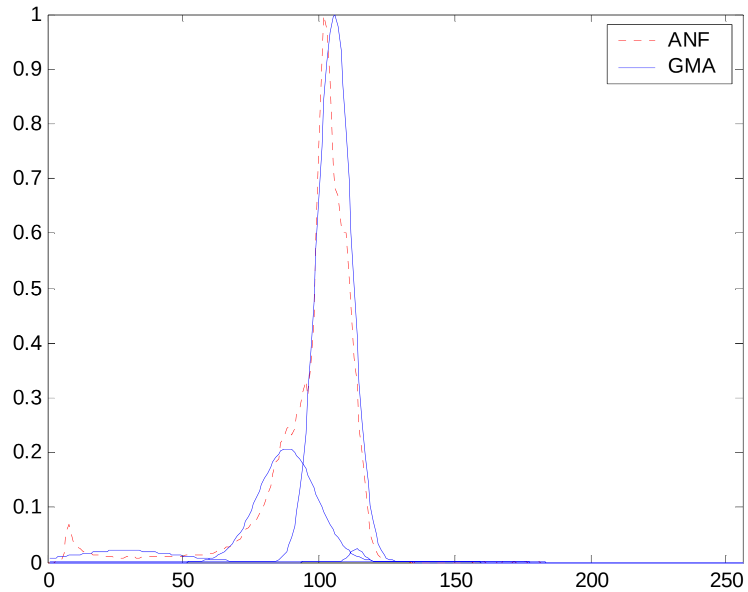

Figure 5.12 The GMA estimation (solid) and histogram of the ANF image (dashed)

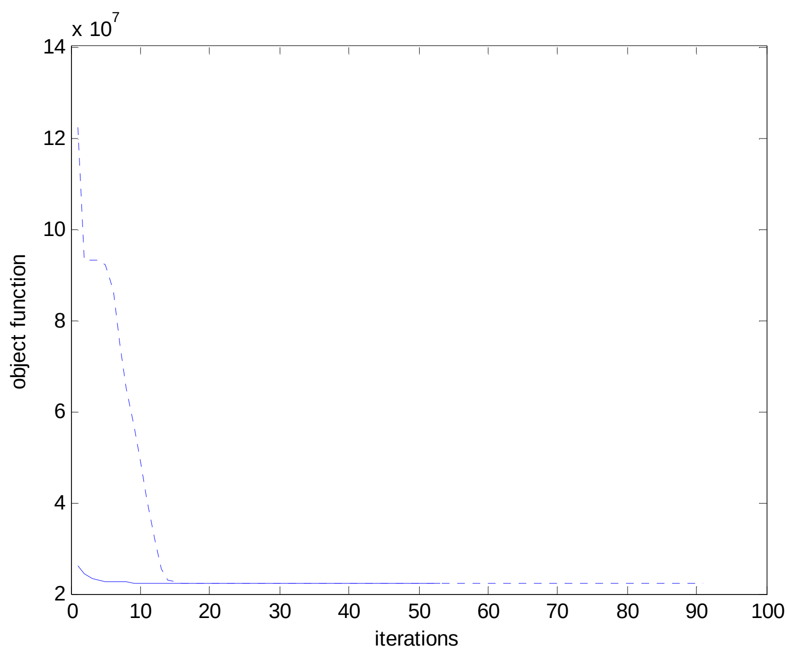

Figure 5.13 Convergence rates of the GMA (solid) and random initial values (dashed)

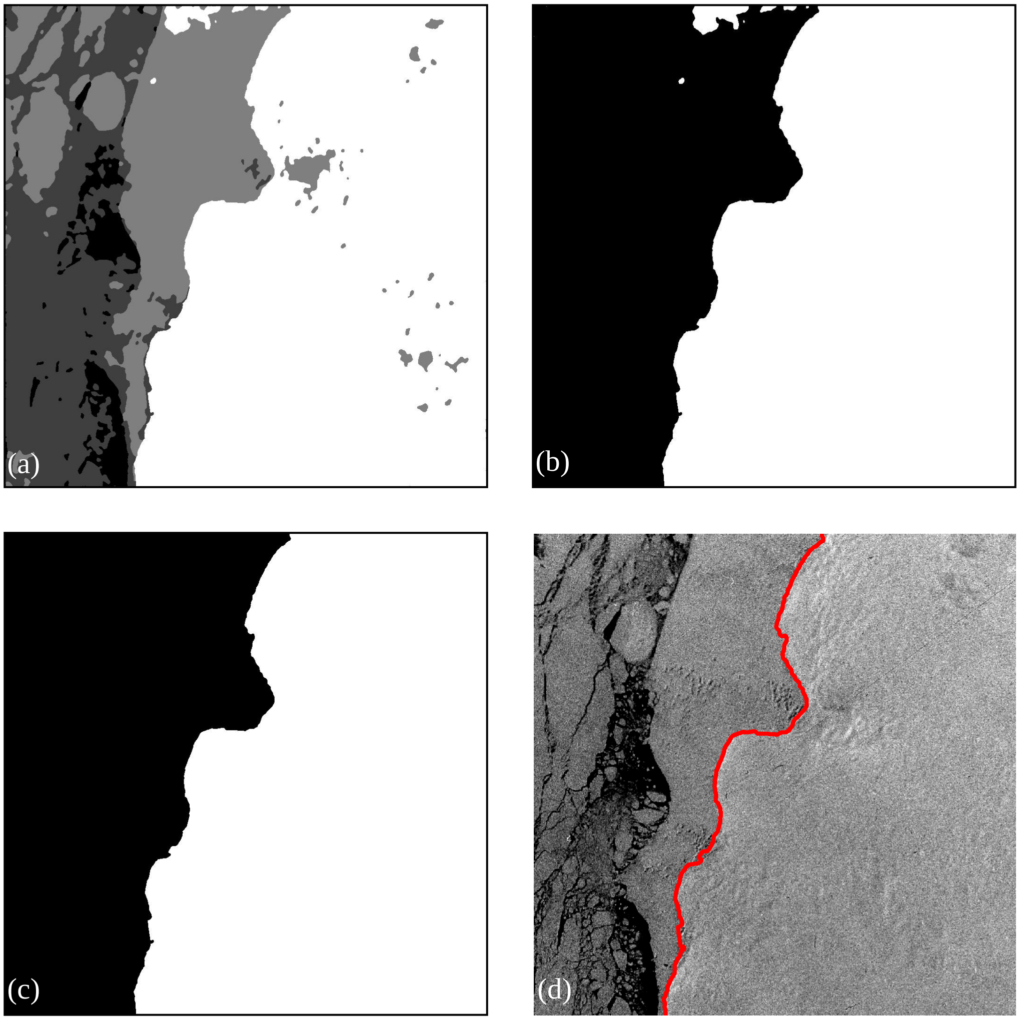

Figure 5.14 MPM segmentation and boundary detection: (a) MPM segmentation with four classes – glacier in white, fast ice in bright gray, sea ice in bright and dark gray, and water in black; (b) the binary image with a background region and all object regions; (c) the binary image with an object region and a background region; and (d) the original image overlaid with the boundary extracted from (c).

5.2.4 Mountainous Coastline

The original image in Figure 5.15 (top) displays the western part of the Antarctic Peninsula $(65^{\circ}03'W, 66^{\circ}16'S)$. In this image, the Peninsula is completely covered by an ice cap that drains over steep cliffs, giving origin to outlet glaciers extending onto the sea and partly covered by mountain shadows (black). The ocean is completely filled with sea ice. The ambiguous extremes of outlet glaciers and mountain shadows make it difficult to recognize the correct positions of the coastline because the sea ice is homogeneously gray. The histogram of the original image shows that it may consist of three different classes such as sea ice, glacier and mountain shadow. However, the histogram of the ANF image (bottom) indicates that the glaciers may be divided into two different ones in terms of gray levels (i.e., dark glacier and bright glacier). Based on this interpretation about the number of classes, the GMA estimation (Figure 5.16) was performed to verify the histogram interpretation. Using the estimated GMA as initial values, the FCM was performed to compute the class-conditional energy function, and the processing converged around 45 iterations (Figure 5.17).

After the FCM process, the MPM procedure was carried out with the same parameters of k and n in the previous case. The sequential results are shown in Figure 5.18. First, class 4 (white) was labeled as background regions, and others were merged as object regions. Second, background regions smaller than the maximum size of background regions were eliminated (Figure 5.18 (b)), and object regions smaller than the maximum size of object regions were eliminated (Figure 5.18 (c)). Figure 5.18 (d) shows the original image overlaid with the boundary extracted from Figure 5.18 (c).

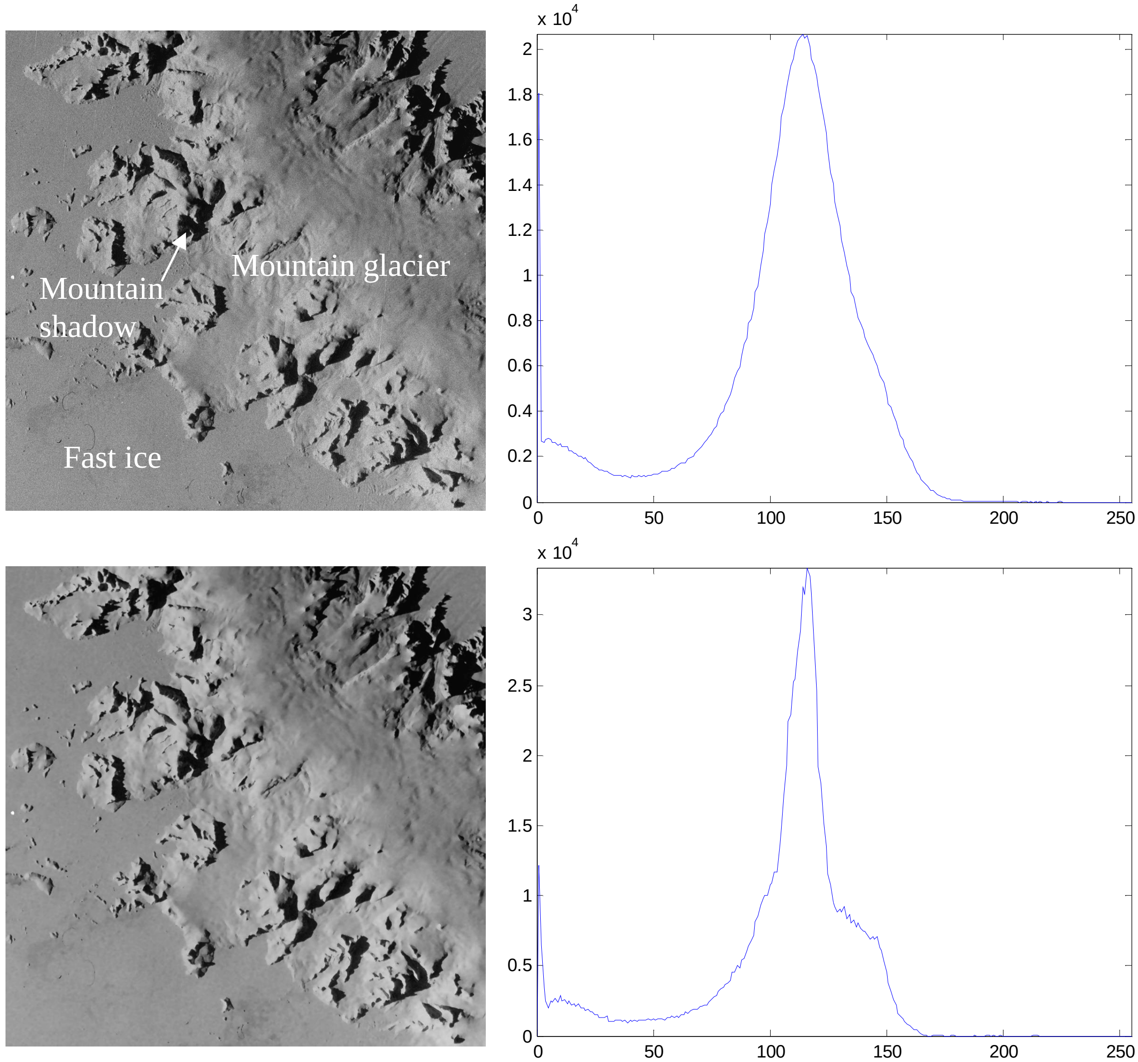

Figure 5.15 Original image (top), ANF image (bottom) and corresponding histograms

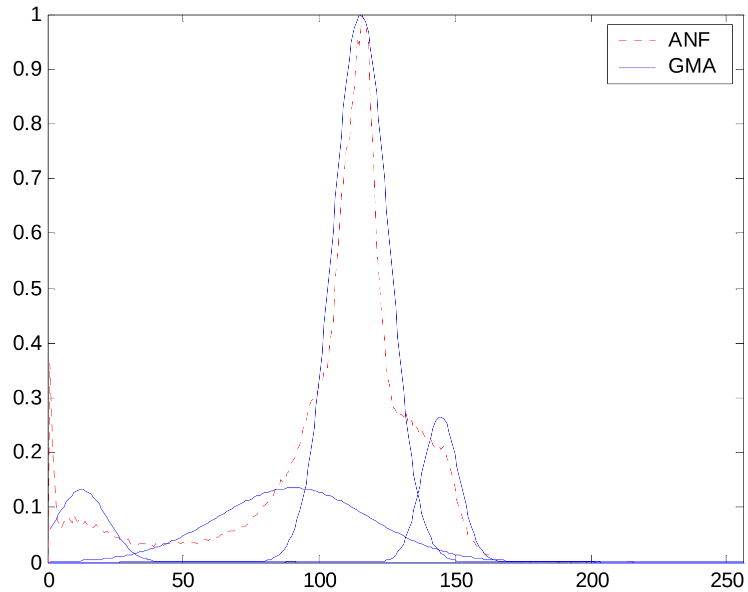

Figure 5.16 The GMA estimation (solid) and histogram of ANF image (dashed)

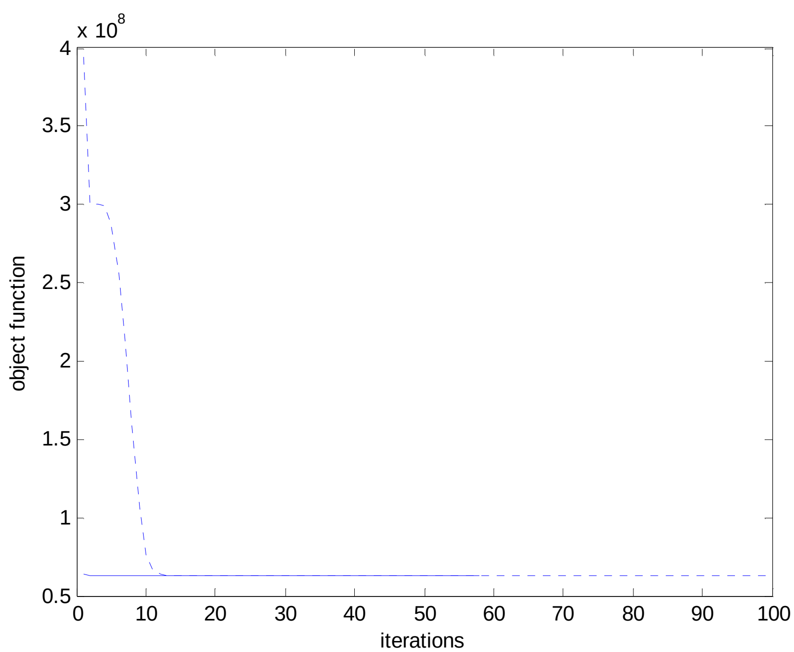

Figure 5.17 FCM convergence rate of the GMA (solid) and random initial values(dashed)

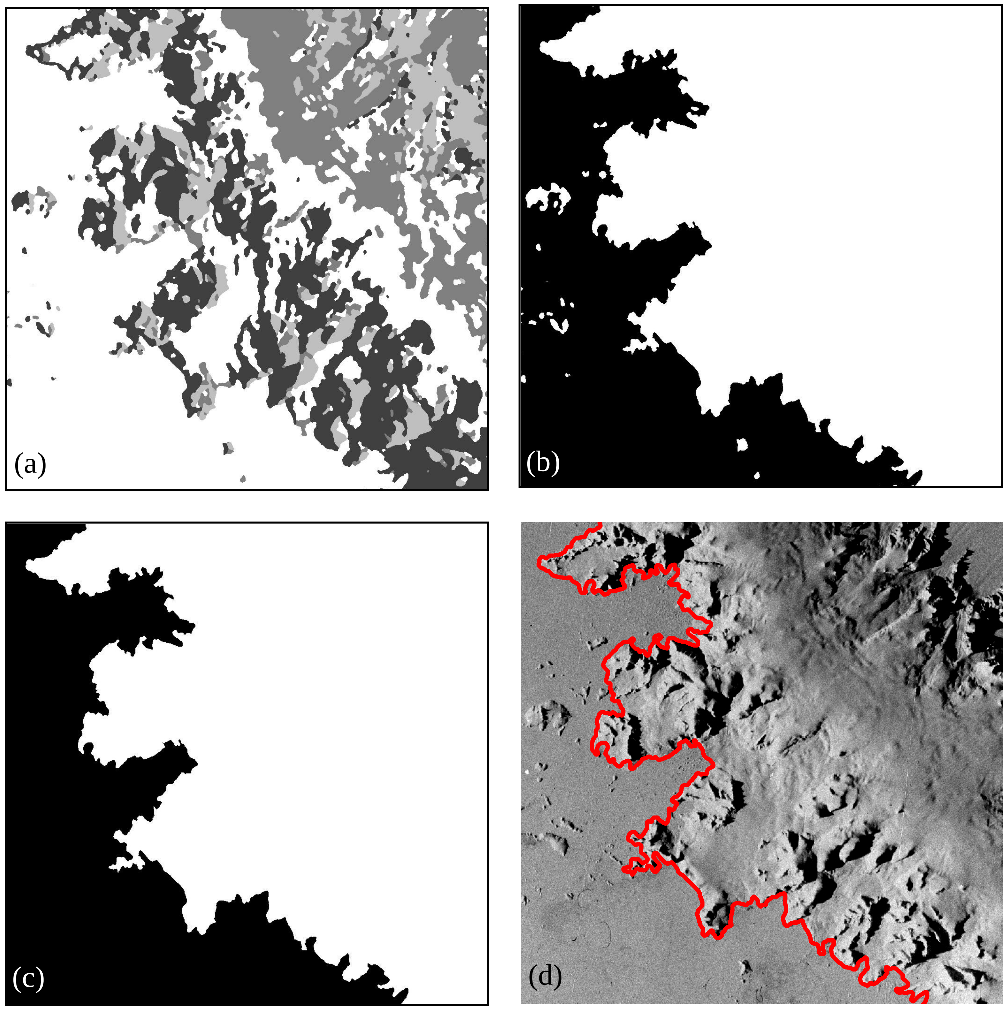

Figure 5.18 MPM segmentation and boundary detection: (a) MPM segmentation with four classes – bright glacier in black, mountain shadow in bright gray, dark glacier in gray, and fast ice in white; (b) the binary image with a background region and all object regions; (c) the binary image with an object region and a background region; and (d) the original image overlaid with the boundary extracted from (c).

Most of the coastline in this case was correctly extracted by the MPM algorithm, but there are several misclassified areas due to non-optimal parameter settings during the processing. Figure 5.19 shows an example of the misclassified areas where the coastline is located between the outlet glacier and the fast ice. For this case, a simple manual editing is required

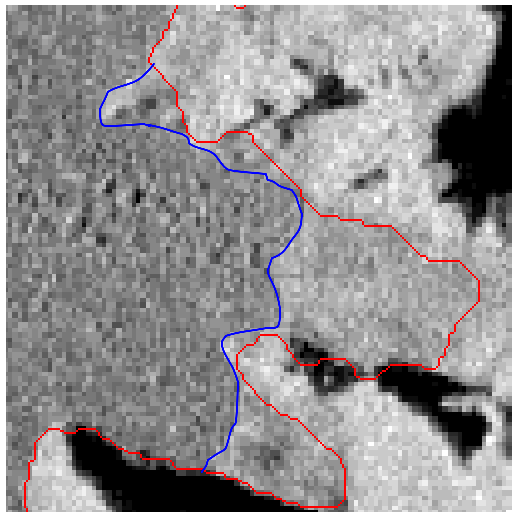

Figure 5.19 The misclassified area: automatically extracted coastline (red) and actual coastline (blue)

5.2.5 Mixture Classes

Figure 5.20 (top) shows a complete mixture area located in Lützow-Holm Bay $(35^{\circ}00'E, 68^{\circ}58'S)$. The region around this bay is the most difficult to correctly segment because of the combination of sea ice, fast ice, icebergs, open water, ice tongues and glacier. Although the ANF filtering slightly enhanced the details in the original image, as seen in Figure 5.20 (bottom), any boundary features were not improved enough for further processing.

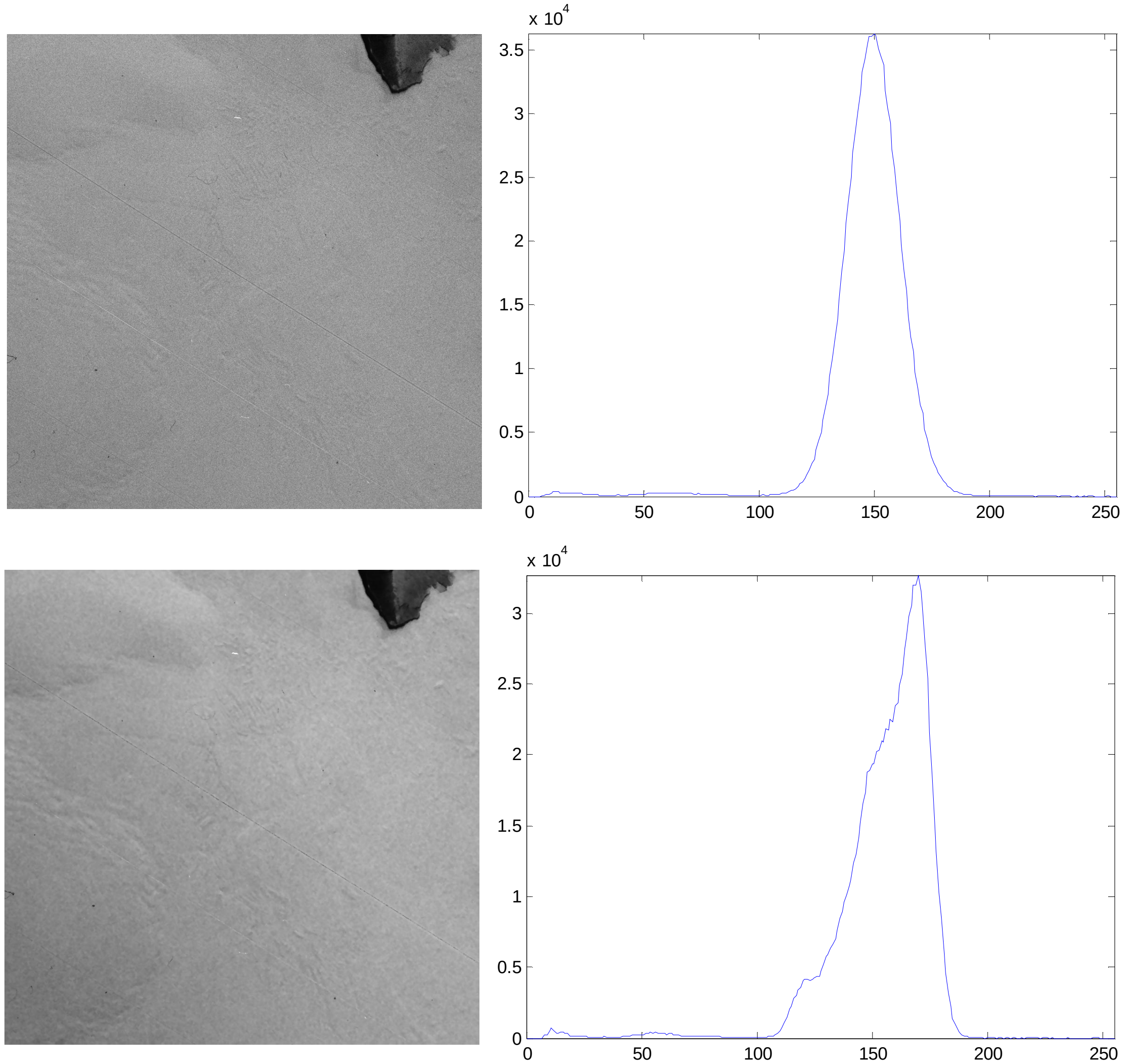

Figure 5.20 Original image (top), ANF image (bottom) and corresponding histograms

Two GMA estimations were then performed with three classes (black in Figure 5.21) and four classes (blue in Figure 5.21). In the case of three classes, the GMA was very close to the ANF histogram, but the smallest distribution of the GMA (left hand side) spread out widely. In the case of four classes, the GMA was totally offset from the ANF histogram.

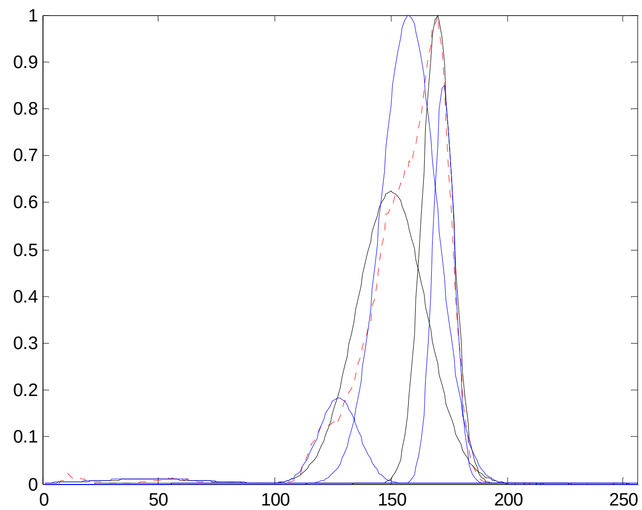

Figure 5.21 Two GMA estimations (three classes in black and four classes in blue) and ANF histogram (dashed)

Based on these two GMA estimations, the MPM algorithm was performed with both three- and four-class GMA estimations. The results are shown in Figure 5.22. Both results are far from the truth. This may originally stem from blob-like features (i.e., small icebergs and sea ices) and very little contrast between glacier ice and other classes. The small icebergs and sea ice act as noise during the processing, whereas the segmentation algorithm did not correctly recognize homogeneous regions in the scene.

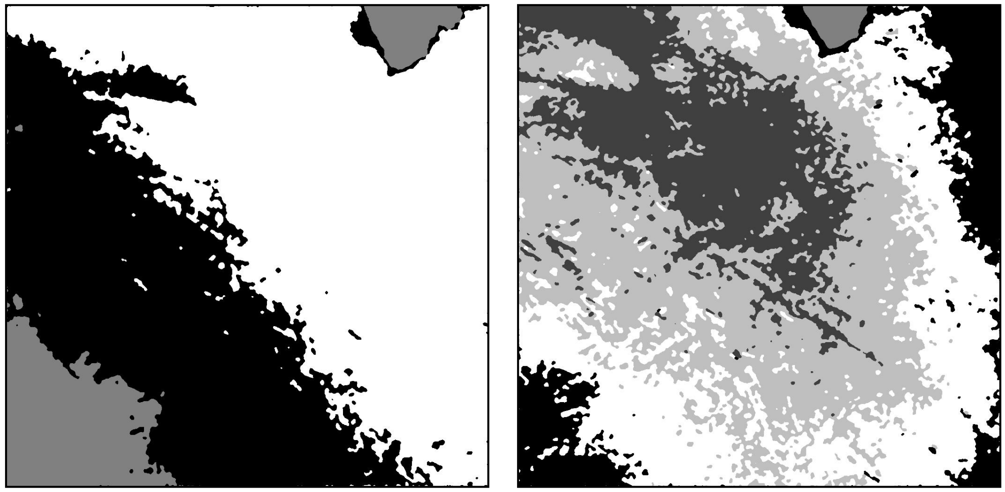

Figure 5.22 Three-class segmentation (left) and four-class segmentation (right)

In this case, manual digitizing was carried out based on intermediate image processing and visual inspection. An adaptive histogram equalization (AHE) technique was used as the intermediate image processing step during the manual delineation. It partitions an ANF image into $N \times N$ subregions, and the histogram for each region is calculated and used to perform local image enhancement. This technique is a useful tool for enhancing the details in very low contrast images, but still will not work with the boundary detection software because the AHE results in blob-like texture images. The comparison of the global and local histogram equalization is shown in Figure 5.23 (a) and (b).

Detailed enlargements of the fast ice-dominated AHE image were visually inspected. Subtle curvilinear shadows were taken to be the coastline. During the manual digitizing, characteristic features such as crevasses, rifts, and icebergs were used for distinguishing continuous coastline from fast ice. Coastline derived from the manual digitizing is shown in Figure 5.23 (c).

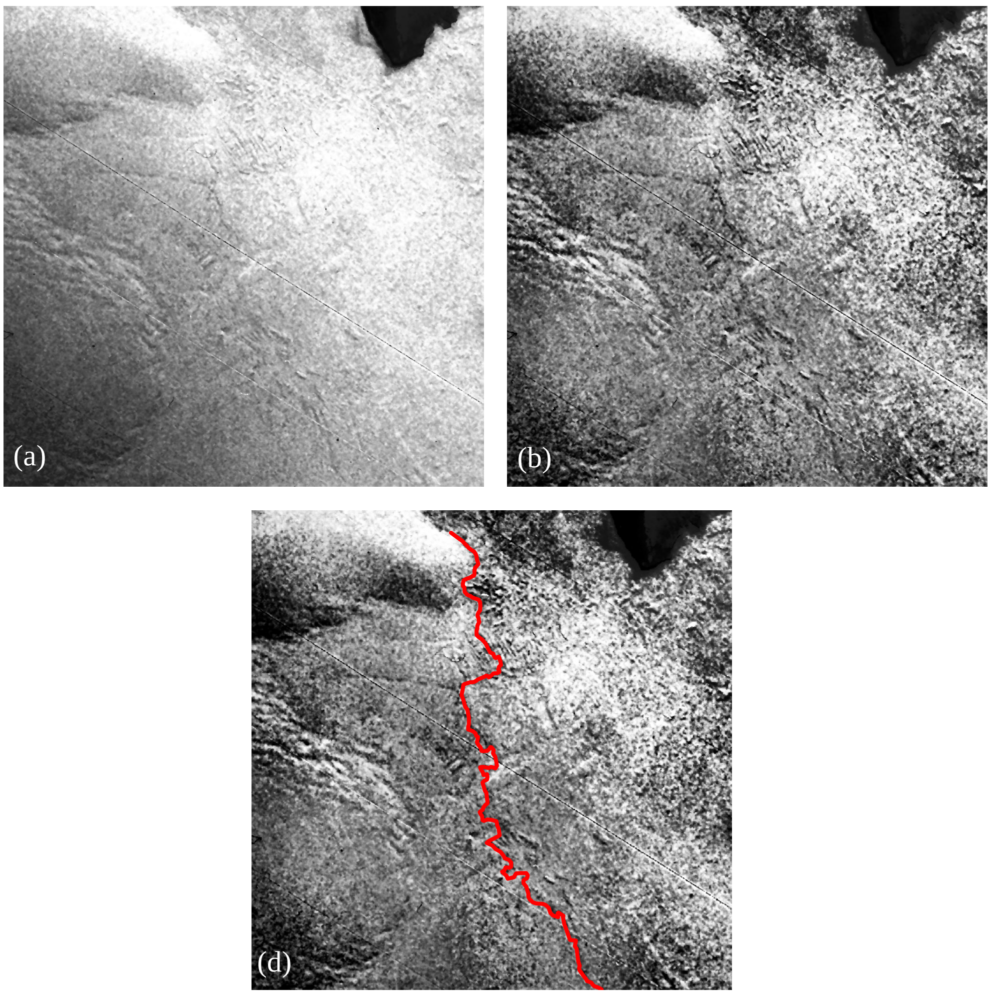

Figure 5.23 (a) Global histogram equalization, (b) adaptive histogram equalization, and (c) coastline derived from manual digitizing based on (b).

5.2.6 Antarctic Coastline

156 small image blocks (1024×1024) along the entire coast of Antarctica, except Lassiter Coast ($60^\circ W$ - $61^\circ W$), Bryan and Eights Coast ($100^\circ W$ - $144^\circ W$), Alexander Island ($72^\circ W$ - $85^\circ W$), Syowa Prince Olav Coast ($42^\circ E$ - $46^\circ E$), Mawson Coast ($58^\circ E$ - $62^\circ E$), and Wilhelm II Coast ($85^\circ E$ - $90^\circ E$) that are completely obscured by significant cloud cover, were processed with the segmentation and boundary detection software and mosaicked. Figure 5.24 shows the coastline automatically extracted through the manner described in Section 5.2.1 to 5.2.4.

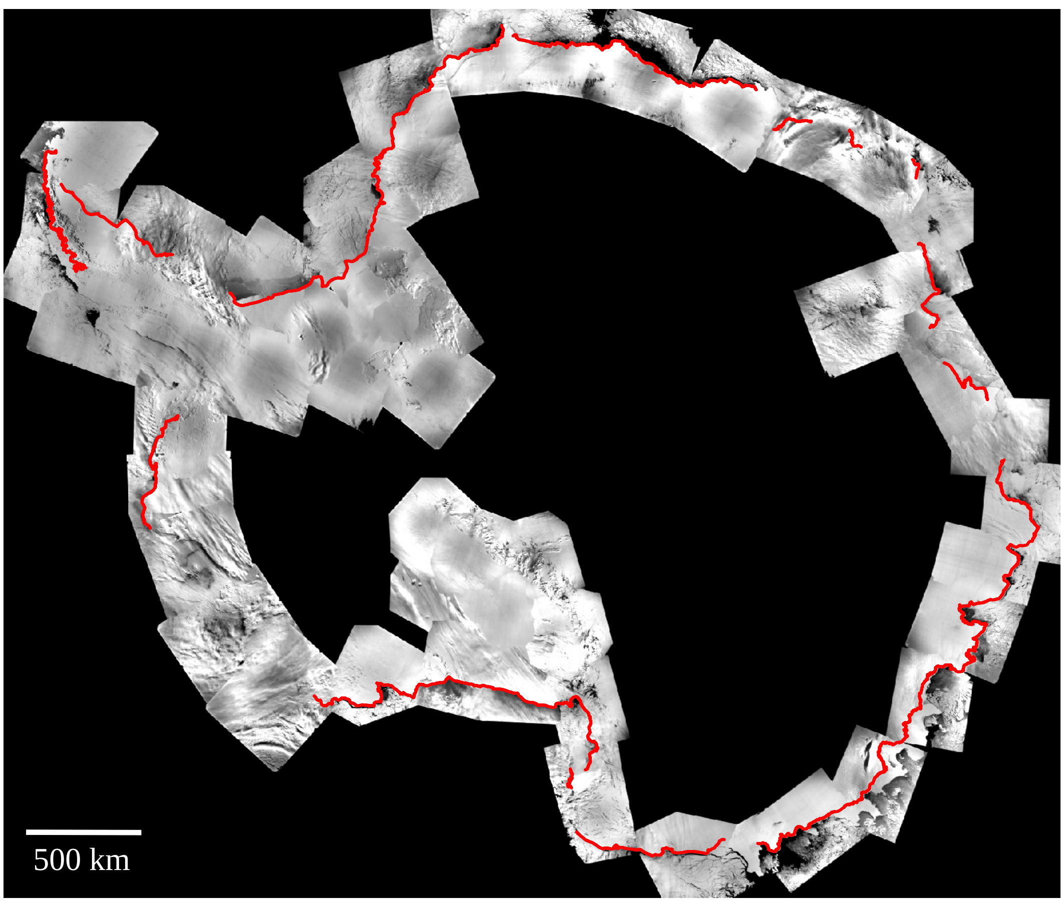

Figure 5.24 Coastline automatically detected from the DISP image mosaic of Antarctica

5.2.7 Coastline Refinements

During the automatic, systematic processing of the DISP image mosaic for Antarctica, the segmentation algorithm was occasionally confused by either non-optimal parameter setting for an image (i.e., the number of classes) or mainly the lack of consistent, sufficient contrast between glacier ice and other regions (Figure 5.15). In this case, a coastline refinement process is required to find more correct positions of the coastline. The AHE method described in Section 5.2.5 was incorporated for the refinement process. Figure 5.25 shows an example of how the segmentation algorithm could be confused between the actual coastline and the more distinctive boundary, which separates open water (black) and sea ice (gray). Figure 5.25 (c) shows that the actual position of the coastline (red) is placed inward from the detected boundary (blue). The area between the actual coastline and detected boundary is filled with fast ice. To correctly place the coastline, the AHE process was applied to the ANF image in Figure 5.25 (a). The resulting AHE image in Figure 5.25 (b) helps human operators to find more a correct coastline over the image. Based on the AHE image, manual editing was carried out in the same manner described in Section 5.2.5. It relied on feature characteristics (i.e., crevasses, rifts and icebergs) and other historical coastline map, such as that was published in Moscow by the Main Administration of Geodesy and Cartography, Ministry of Geology USSR (Tolstikov, 1966). Figure 5.25 (c) shows the automatically detected boundary and manually edited coastline over the AHE image.

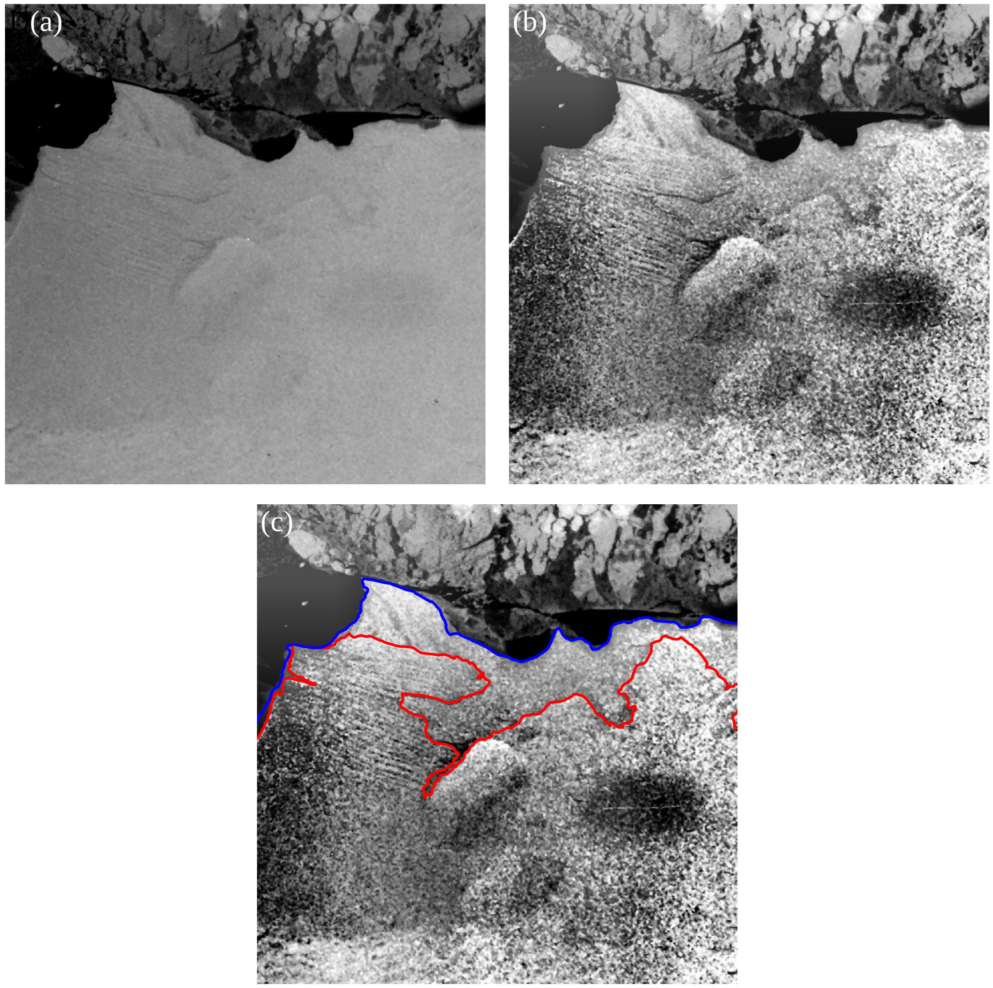

Figure 5.25 Coastline refinements: (a) ANF image; (b) AHE image; and (c) manually edited coastline (red) in comparison with the automatically detected boundary (blue).

Another example of a larger area along the Saunders Coast $(148^{\circ}38'W, 75^{\circ}56'S)$ is shown in Figure 5.26. In this case, large icebergs and sea ice floes beyond the ice shelves and ice caps are clearly seen in the AHE image (middle), and curvilinear shadows are also distinguished from the ice shelves and ice caps. Based on this visual interpretation, the correct positions of the coastline (red) were placed more landward from the automatically detected boundary (blue). The USSR coastlines are also much close to the refined coastline than the automatically detected boundary.

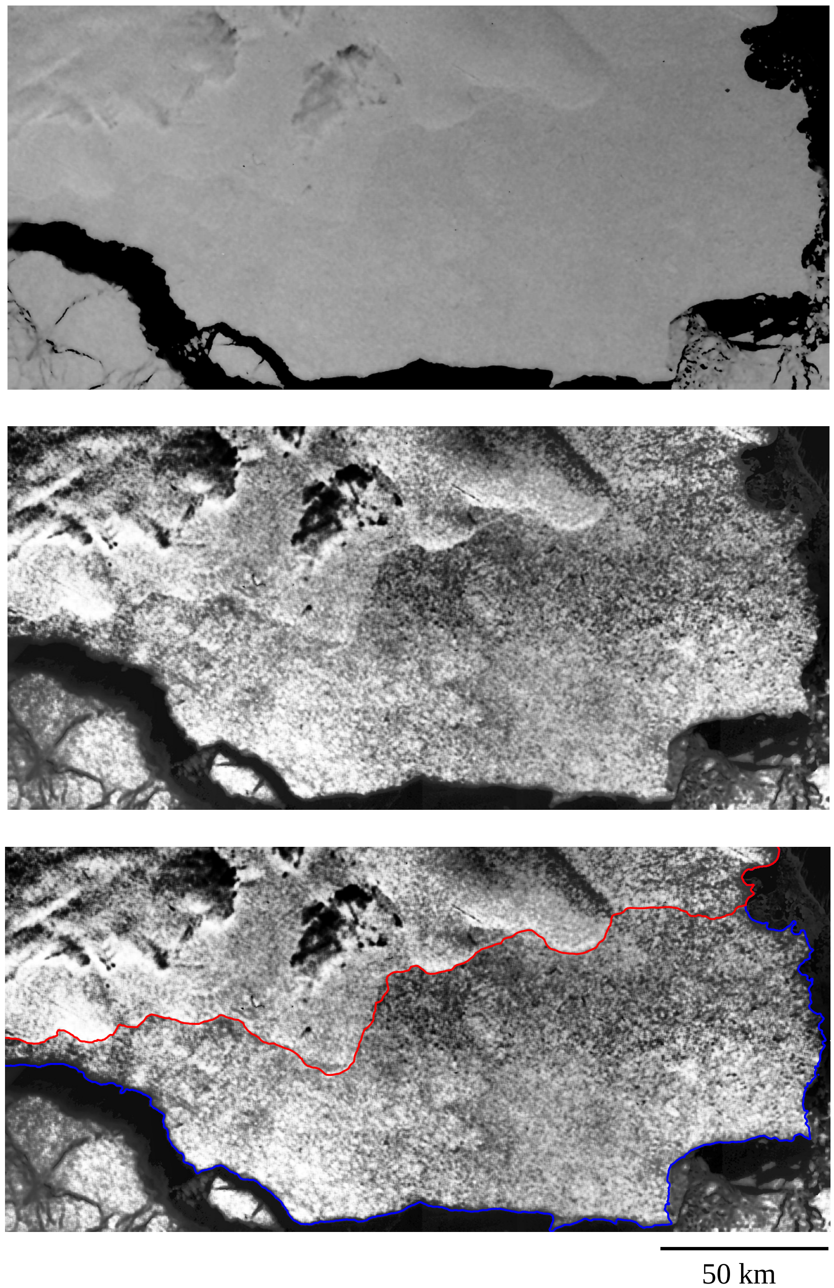

Figure 5.26 Coastline refinements: (a) ANF image; (b) AHE image; and (c) manually edited coastline (red) in comparison of the automatically detected boundary (blue)

There are some places, where it is almost impossible to correctly refine and place the coastline even through use of the intermediate image processing. Figure 5.27 shows such examples: (a) artificial straight-lines and (b) light blob-like clouds make the scene dirty and confused. Although some boundaries were successfully detected by the segmentation and boundary detection software, they are suspicious because (1) the comparison of the 1956 (a) and 1958 (b) USSR maps and the 1997 SAR coastline (red) shows that this is almost stable over time and (2) although the accuracy of the Soviet map may not be guaranteed, the difference between the automatically detected coastline (blue) and the Soviet coastline is beyond the possible changes in the Antarctic coastline. Consequently, the boundaries automatically detected from these cases cannot be guaranteed.

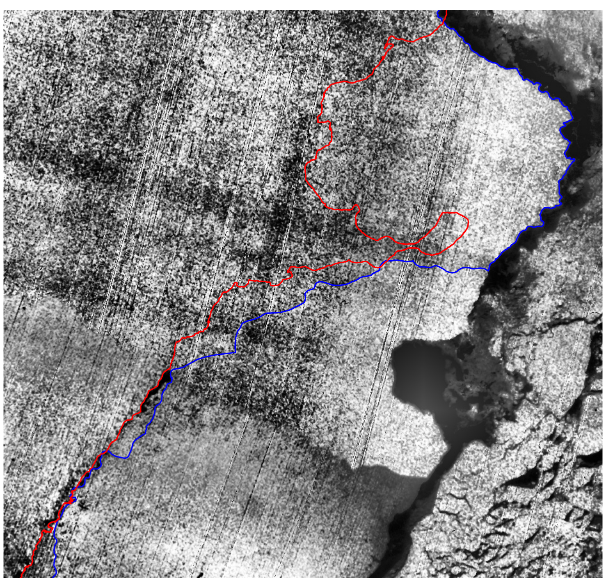

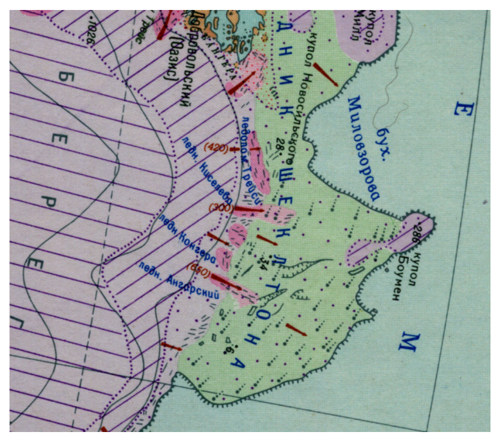

Figure 5.27 (a) Automatically detected coastline (blue), 1997 SAR coastline (red), and 1956 Soviet map (right) in Shackleton Ice Shelf $(103^{\circ}57'E, 65^{\circ}42'6S)$

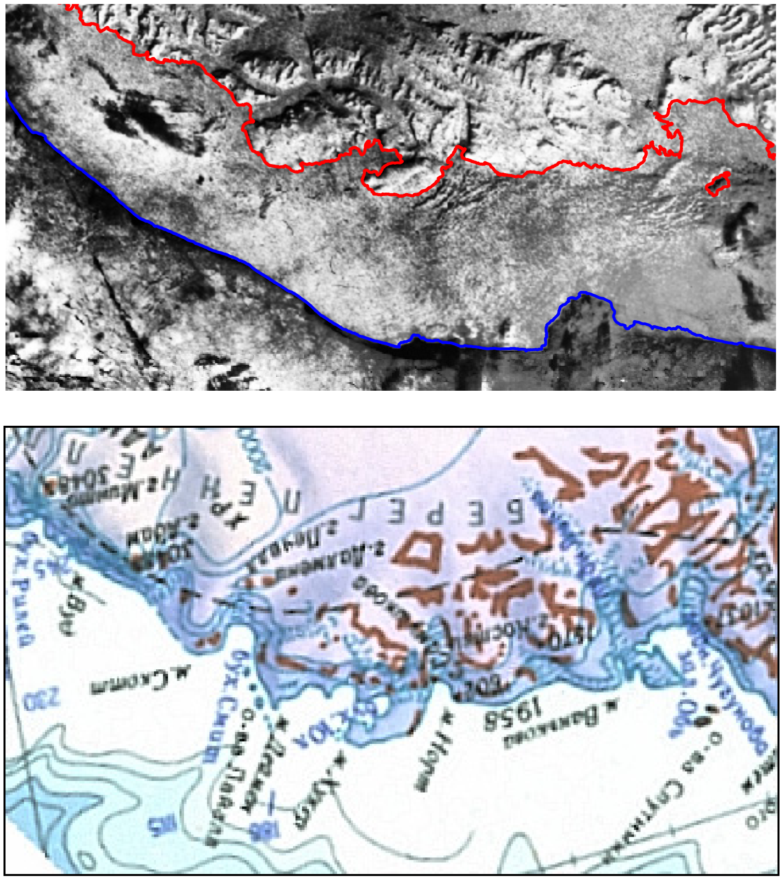

Figure 5.27 (b) Automatically detected coastline (blue), 1997 SAR coastline (red), and 1958 Soviet map (right) in Mountains Pennell Coast $(166^{\circ}08'E, 70^{\circ}35'6S)$

In this manner, approximately 30% of the automatically detected coastline was edited and replaced. The resulting coastline is shown in Figure 5.28. The automated coastline in Figure 5.24 is in blue, and the refined coastline is in red. The coastlines (green) around Shackleton Ice Shelf and Mountains Pennell Coast were the most difficult to interpret because of artificial features and blob-like clouds; consequently, we have less confidence in our results for these sectors.

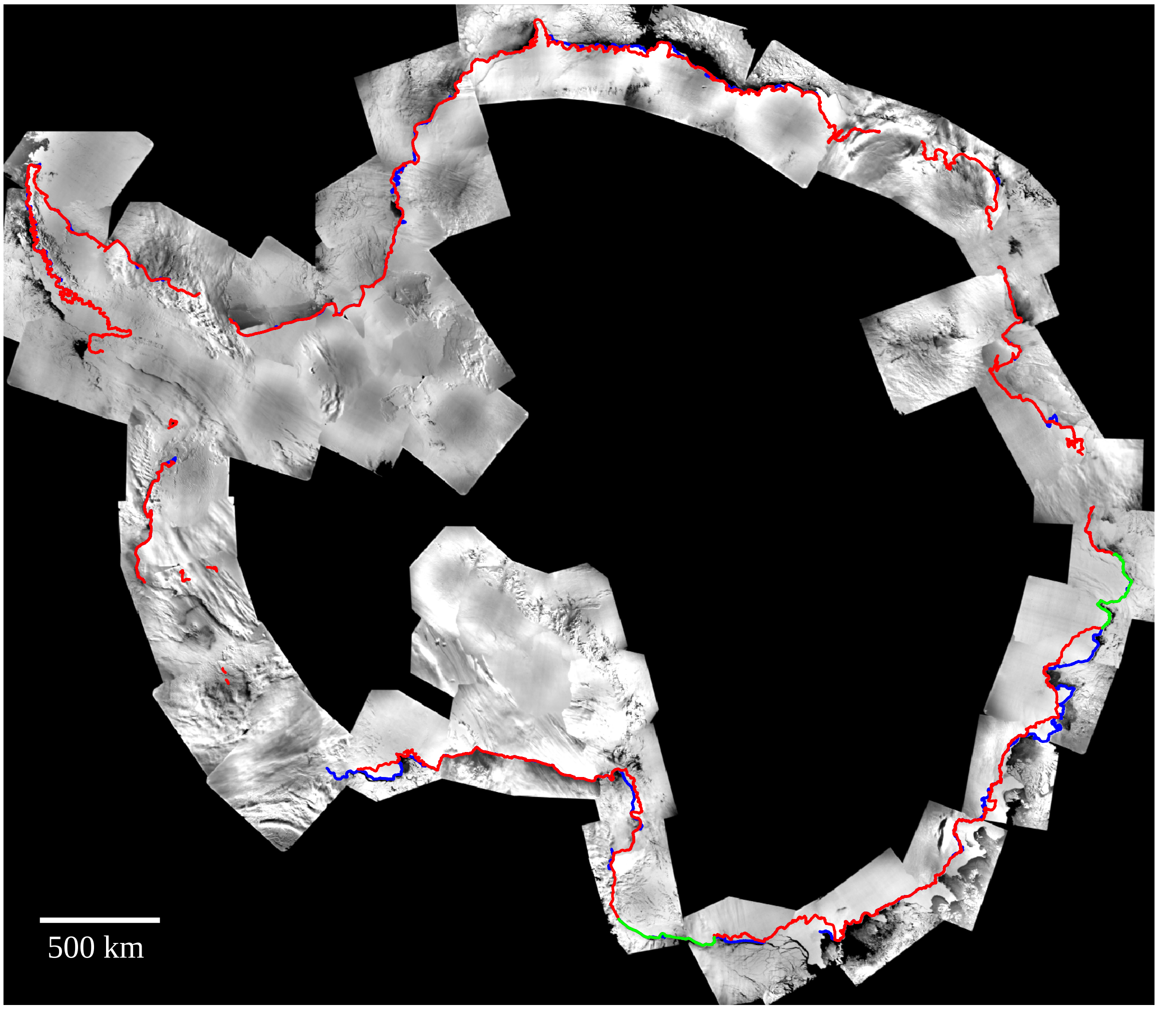

Figure 5.28 Automated coastline (blue) in Figure 5.24 and refined coastline (red) on the DISP image mosaic: the uncertain coastline is in green.

5.3 Accuracy Assessments

The quality of the coastline data must be known when analyzing changes in comparison with other time series data. Accuracy assessments were conducted by visual checking after the coastline had been extracted from the DISP image mosaic of Antarctica. The accuracy of the extracted coastline is influenced by the coastline extraction method and mainly by the geo-referencing accuracy of the source image; consequently, we approximately estimated position errors using $\sqrt{\sigma_i^2 + \sigma_c^2}$, where σ_i is the positional accuracy of the DISP image mosaic and σ_c is the error in identifying coastlines on the DISP image mosaic. By comparing between the algorithm-derived coastline and the coastline visually interpreted from the original images, we approximately estimated the positional accuracy of the DISP image mosaic to be less than 2 pixels in 100-m pixel resolution (see Chapter 3) and the extracted coastline on the DISP image mosaic to be less than 1 pixel, noting that the extracted coastline accuracy may be larger than 3 pixels where light cloud cover exists. Based on these accuracies, we estimated the overall accuracy of the extracted coastline to be between 200 to 500-m except the uncertain regions in Figure 5.28.

CHAPTER 6

CHANGE DETECTION OF THE ANTARCTIC COAST IN A GEOGRAPHIC INFORMATION ENVIRONMENT

6.1 Introduction

Change detection of Antarctic coastlines is a topic of great interest to glaciologists and climatologists. Detecting changing Antarctic coastal environments by using increasing amounts of time series data is done most efficiently in a geographic information system (GIS) environment. The DISP image mosaic is useful for capturing historic, geospatial information of the Antarctic coastline in 1963. Though a GIS, the 1963 data are integrated with earlier and later data to assess continental scale changes in ice margin advance or retreat.

Time series data presented in this chapter quantify changes in the Antarctic coastline using DISP, SCAR ADD, and SAR data. The SCAR ADD data are produced as a topographic database compiled from a variety of Antarctic map and satellite image sources originated between 1966 and 1991 for the entire Antarctic coast (ADD Consortium, 2000). The SAR data are used to extract a complete, Antarctic coastline from 1997 RADARSAT-1 SAR image mosaic (Liu and Jezek, 2003). Data sources and features obtained for the Antarctic coast are plotted along a timeline in Table 6.1. Additional EOS data are also used in local studies of particular glaciers.

<table>
<tr><th colspan="2">Data source</th><th>Source date</th><th colspan="2">Source scale or resolution</th><th>Features</th></tr>
<tr><td colspan="2">Declassified satellite photographs</td><td>1963</td><td>100-m</td><td>33-µm pixel</td><td>Coastline</td></tr>
<tr><td rowspan="14">ADD dada from map, aerial photographs, and LANDSAT images</td><td>Abbot</td><td>1968</td><td rowspan="14">1:1,000,000</td><td>1:500,000</td><td rowspan="14">Coastline and Grounding line</td></tr>
<tr><td>Amery</td><td>1971</td><td>1:1,000,000</td></tr>
<tr><td>Fimbul</td><td>1976/1983</td><td>1:1,000,000/6,000,000</td></tr>
<tr><td>Lazarev</td><td>1976</td><td>1:1,000,000</td></tr>
<tr><td>N.Larsen</td><td>1978</td><td>1:250,000</td></tr>
<tr><td>Ragnhild A</td><td>1983</td><td>1:6,000,000</td></tr>
<tr><td>Ragnhild B</td><td>1983</td><td>1:6,000,000</td></tr>
<tr><td>Ragnhild C</td><td>1983</td><td>1:6,000,000</td></tr>
<tr><td>Riiser Larsen</td><td>1988/1990</td><td>1:1,000,000</td></tr>
<tr><td>Ronne-Filchner</td><td>1978/1991</td><td>1:250,000/1,000,000</td></tr>
<tr><td>Ross</td><td>1983/1989</td><td>1:250,000/6,000,000</td></tr>
<tr><td>Shackleton</td><td>1969</td><td>1:1,000,000</td></tr>
<tr><td>S.Larsen</td><td>1978</td><td>1:250,000</td></tr>
<tr><td>West</td><td>1969</td><td>1:1,000,000</td></tr>
<tr><td colspan="2">RADARSAT-1 SAR images</td><td>1997</td><td colspan="2">25-m</td><td>Coastline</td></tr>
</table>

*According to National Map Accuracy Standards (Light, 1993): 130-m positional accuracy of 1:250,000, 260-m for 1:500,000; 520-m for 1:1,000,000; and 3120-m for 1:6,000,000

Table 6.1 Cartographic source data used to analyze changes in the Antarctic coastline

6.2 Antarctic Ice Shelves

Figure 6.1 shows the major ice shelves selected for measuring changes in the Antarctic coastline using the time series data in Table 6.1. Most Antarctic ice shelves were included in this analysis. The Getz Ice Shelf $(110^\circ W - 150^\circ W)$ was excluded because it is completely obscured by significant cloud cover on the DISP image mosaic.

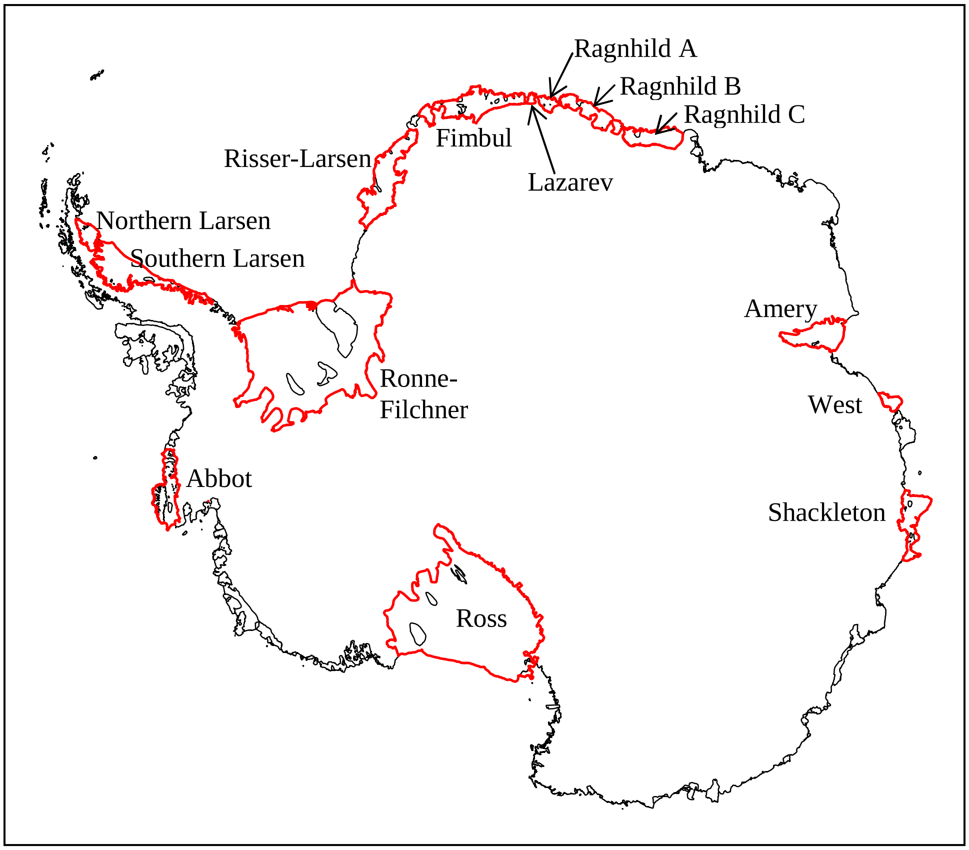

Figure 6.1 Major Antarctic ice shelves (red) used to measure changes in the Antarctic coastline using time series data between 1963 and 1997

Combined areal extents of the ice shelves and ice rises were produced on the basis of each coastline and the ADD grounding line positions. Table 6.2 show areas and changes in area of each ice shelf between 1963 and 1997. As described in Chapter 5, we have less confidence in our results for Shackleton Ice Shelf, so we removed this sector for subsequent analysis of ice shelf change. Calculating the area of the ice shelves at each time epoch, we find that the major Antarctic ice shelves covered approximately

1,425,883 ± 0.2~0.7 km^2 in 1963, 1,383,639 ± 0.2~4.4 km^2 between 1968 and 1991, and 1,413,784 ± 0.03 km^2 in 1997. Net ice shelf areal change is thus -42,243 ± 0.2~3.1 km^2 (2.9% loss) between 1963 and ADD, 30,144 ± 0.1~3.1 km^2 (2.1% gain) between ADD and 1997, and 12,099 ± 0.2~0.5 km^2 (0.8% loss) between 1963 and 1997. It notes that the ADD data is not synchronous at time (see Table 6.1). The more northerly ice shelves, such as Abbot Ice Shelf, Northern Larsen Ice Shelf and ice shelves along Princess Ragnhild Coast systematically retreated between 1963 and 1997. In contrast, Ronne-Filchner Ice Shelf not only systematically advanced, but also remained stable for three decades. Amery Ice Shelf experienced with the greatest fluctuations by retreating from 1963-1971 and advancing from 1971-1997.

Ice Shelf	DISP	ADD	SAR
Abbot	47137.4	46165.2	45978.9
Amery	51433.5	44129.8	47660.5
Fimbul	68562.8	62628.4	62824.9
Lazarev	2359.9	2583.1	2401.8
N. Larsen	15963.4	15223.7	10720.0
Ragnhild_A	7691.2	7557.9	7379.7
Ragnhild_B	31045.0	30433.1	31574.8
Ragnhild_C	37540.1	34030.7	33642.3
Riiser Larsen	83081.3	75940.5	78992.0
Ronne-Filchner	491150.8	493213.9	500692.6
Ross	498019.4	489987.5	509435.0
Shackleton	71669.9	37530.5	35441.5
S. Larsen	83939.3	73037.9	73964.1
West	7959.1	8707.7	8517.6
Total	1497553.7	1421170.3	1449226.4
Total (except Shackleton)	1425883.2	1383639.4	1413784.2

(a) Ice shelf areas measured from DISP, ADD, and SAR

Ice Shelf	DISP-ADD		(%)	ADD-SAR		(%)	DISP-SAR		(%)
Abbot	972.1	R	2.0	186.3	R	0.4	1158.5	R	2.4
Amery	7303.6	R	14.2	3530.6	A	8.0	3772.9	R	7.3
Fimbul	5934.4	R	8.6	196.5	A	0.3	5737.8	R	8.3
Lazarev	223.1	A	9.4	181.2	R	7.0	41.8	A	1.7
N. Larsen	739.6	R	4.6	4503.6	R	29.5	5243.3	R	32.8
Ragnhild_A	133.3	R	1.7	178.1	R	2.3	311.5	R	4.0
Ragnhild_B	611.9	R	1.9	1141.7	A	3.7	529.8	A	1.7
Ragnhild_C	3509.3	R	9.3	388.4	R	1.1	3897.8	R	10.3
Riiser Larsen	7140.8	R	8.5	3051.5	A	4.0	4089.3	R	4.9
Ronne-Filchner	2063.0	A	0.4	7478.6	A	1.5	9541.7	A	1.9
Ross	8031.9	R	1.6	19447.5	A	3.9	11415.6	A	2.2
Shackleton	34139.3	R	47.6	2089.0	R	5.5	36228.3	R	50.5
S. Larsen	10901.3	R	12.9	926.2	A	1.2	9975.1	R	11.8
West	748.5	R	9.4	190.0	R	2.1	558.4	R	7.0
Total	76383.4	R	5.1	28056.0	A	1.9	48327.3	R	3.2
Total (except Shackleton)	42243.8	R	2.9	30144.8	A	2.1	12099.0	R	0.8

(b) Changes in reference to 1947

R Retreat of the ice shelf
A Advance of the ice shelf

Table 6.2 Advance and retreat of major Antarctic ice shelves (in km^2) between 1963 and 1997

Figure 6.2 illustrates coastline positions between 1963 and 1997. Grounding line positions are not changed on this period. Regions of coastline retreat are shown in red and regions of advance are shown in blue. As demonstrated in Table 6.2, the more northerly ice shelves and large ice tongues retreated the most. To address partly the question of whether this observed pattern of advance and retreat are episodic or systematic, several comparisons were carried out. Figure 6.3 and Figure 6.4 show retreat and advance between DISP and ADD and between ADD and SAR coastlines, respectively.

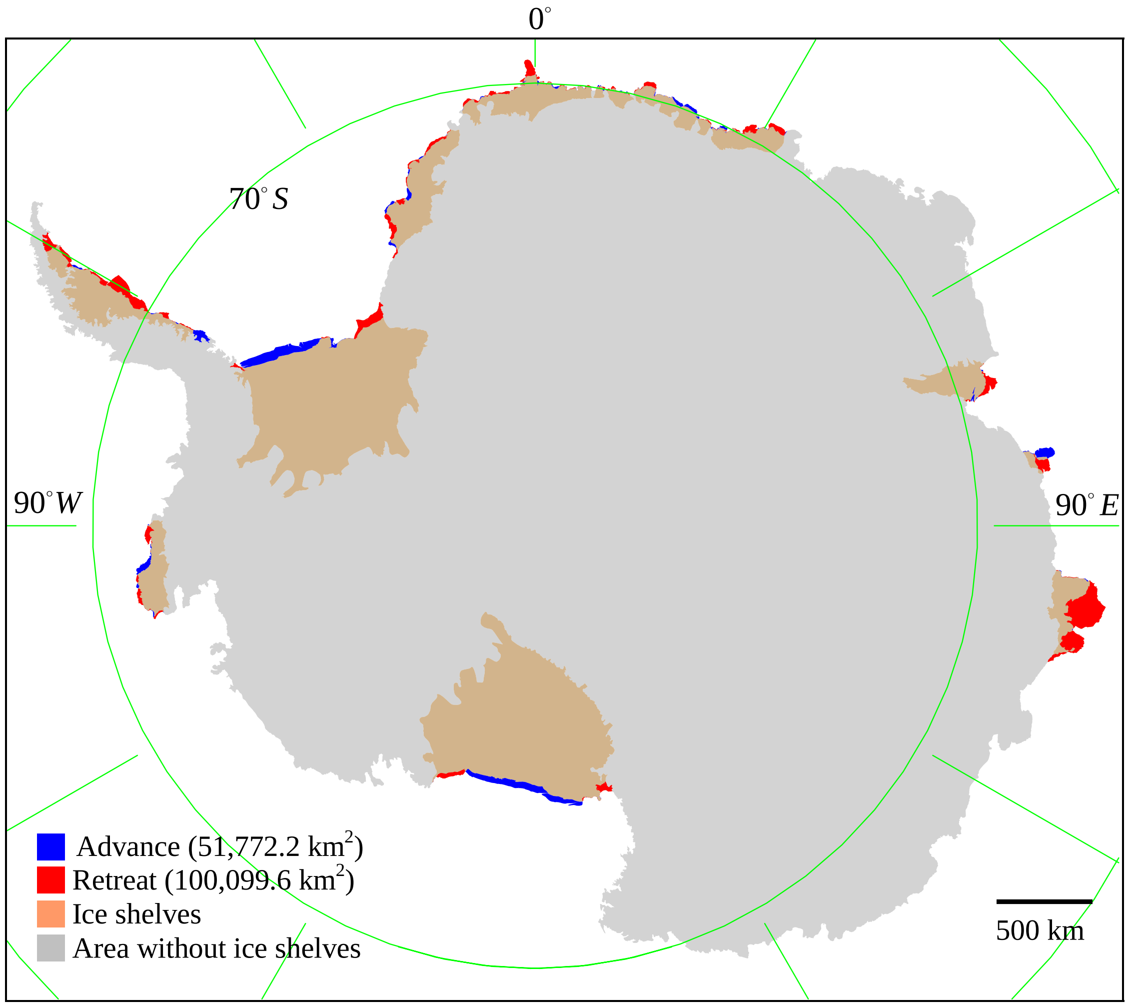

Figure 6.2 Antarctic ice shelf advance and retreat between 1963 and 1997

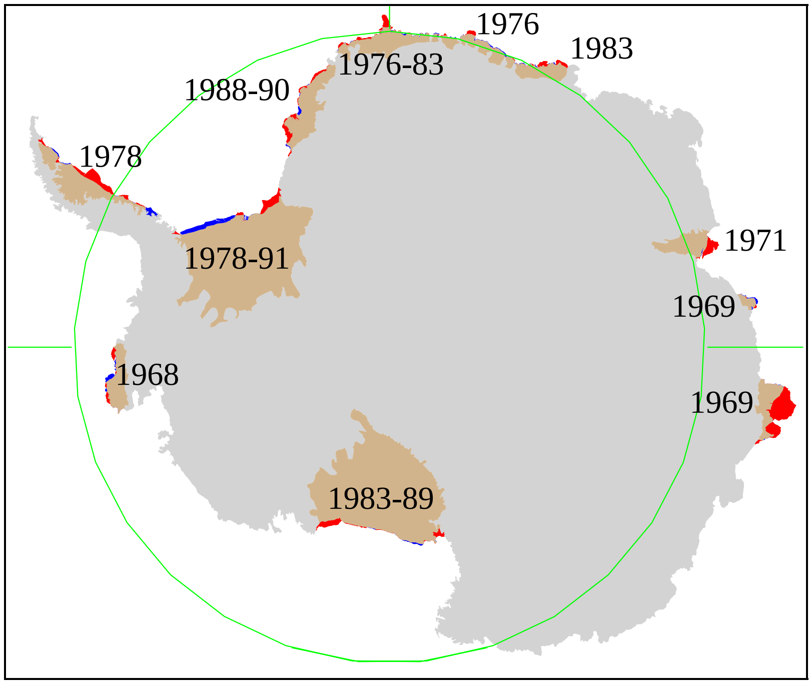

Figure 6.3 Antarctic ice shelf advance and retreat between DISP and ADD

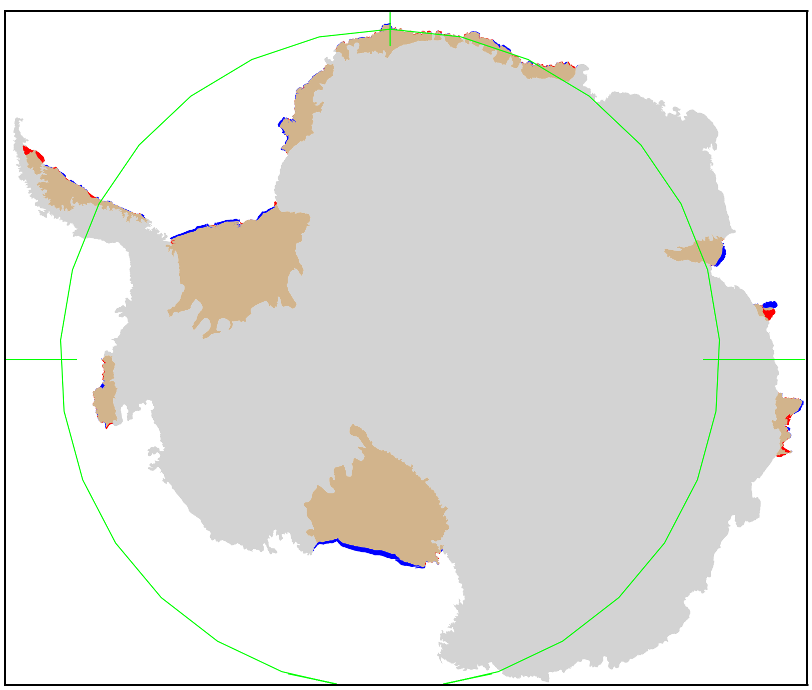

Figure 6.4 Antarctic ice shelf advance and retreat between ADD and SAR

Two facts are revealed by these comparisons. First, ice shelves retreated mostly between DISP and ADD time periods. Second, while Ronne-Filchner Ice Shelf showed a consistent trend between three observations of DISP, ADD, and SAR, Ross Ice Shelf advanced mostly between ADD and SAR time periods.

6.3 Glaciers

Pine Island Glacier was selected for a detailed, local study of ice margin fluctuations. This glacier is one of the largest glaciers in West Antarctica. The glacier speed increased by 18 ± 2 % between 1992 and 2000 (Rignot et al., 2002), and the basin feeding the glacier thinned at 11.7 ± 1.0 cm/yr between 1992 and 1996 (Wingham, 1998). The thinning rate near the grounding line was estimated at 1.6 ± 0.2 m/yr between 1992 and 1999 (Shepherd et al., 2001). This region is believed to be susceptible to ice sheet collapse (Bentley, 1997; Bindschadler, 1997), and therefore the evolution of this glacier is of great interest to scientific community.

DISP, SAR (Jezek, 1999 and 2003), and ASTER (Advanced Spaceborne Thermal Emission and Reflection Radiometer: Abrams and Hook, 2002) data from October 1963, December 1975, September 1997, September 2000 and December 2003 were used in this study. All data were processed in same manner as the Argon DISP data. Results shown in Figure 6.5 are more accurate than Argon-derived results because the source data have better resolution, ranging from 15 to 25-m. Four estimates of the Pine Island Glacier terminus and adjacent coastal regions were overlaid on the 1963 DISP image and its coastline in black (e). They consisted of coastline positions estimated from 1963 DISP, 1975 DISP (25-m resolution), 1997 and 2000 RADARSAT-1 SAR (25-m resolution), and 2003 ASTER data (15-m resolution).

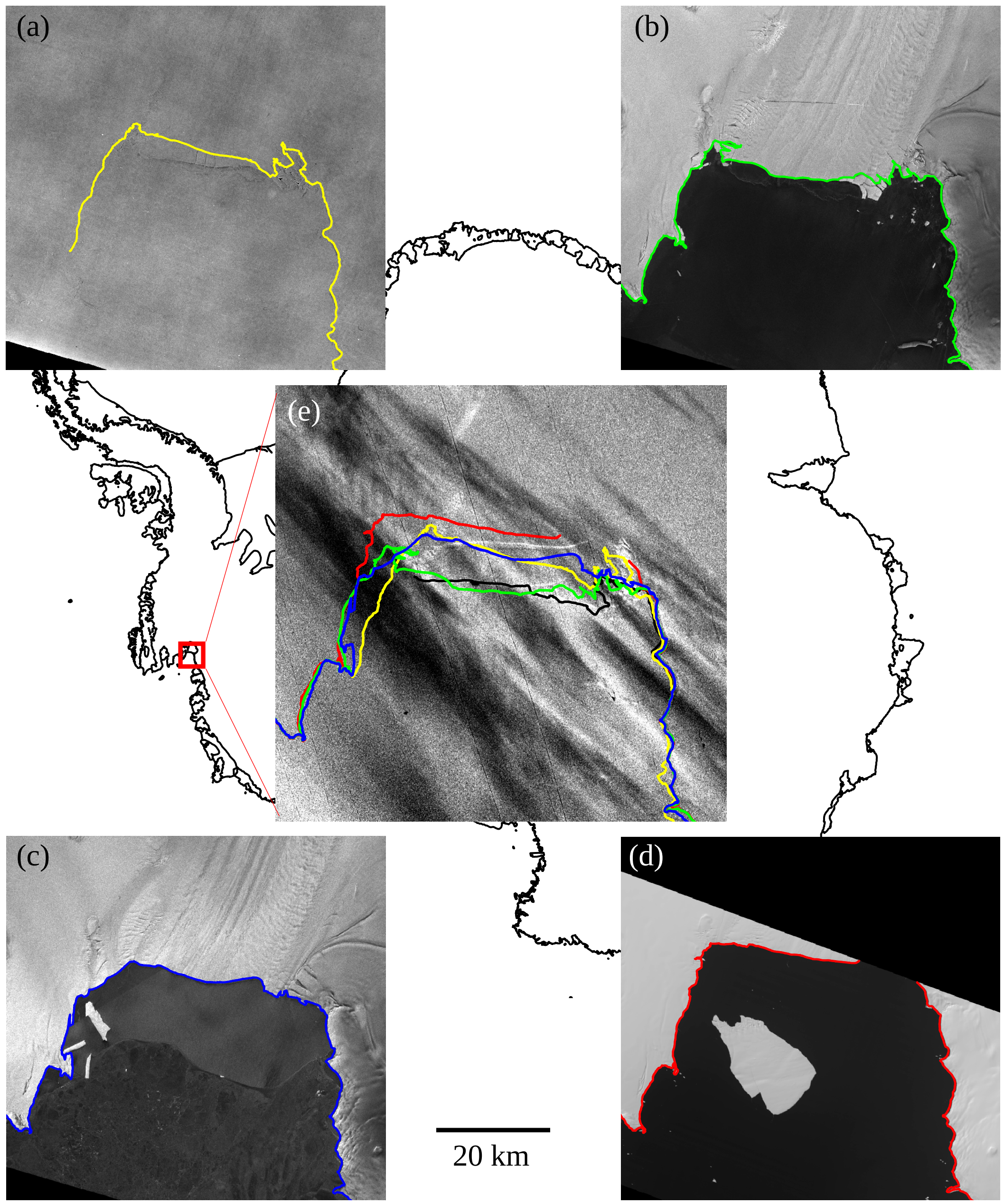

Figure 6.5 Observations of coastline positions of Pine Island Glacier from: (a) 1975 DISP image (b) 1997 RADARSAT-1 SAR image; (c) 2000 RADARSAT-1 SAR image; (d) 2003 ASTER image; and (e) 1963 DISP image.

Glacier terminus position does not change smoothly with time. Rather periods of advance are punctuated by calving events which result in abrupt retreat. Consequently, one must carefully compare images captured at about the same phase of this cycle in order to reliably estimate a retreat and advance rate of the glacier terminus position. For example, an advance rate of approximately 125 m/yr is estimated when measuring from 1947 margin position to 2000 pre-calving margin position, while a retreat rate of approximately 76 m/yr when measuring from 1947 margin position to 2003 post-calving margin position. To avoid this bias in the data, it is necessary to have sufficient data available to reliably estimate a long-term trend of the glacier terminus position.

Rignot's observations derived from aerial and satellite imagery between 1947 and 2000 (Rignot, 2002) and the SCAR ADD data were added to our estimates. All data sources used for this interpretation, acquisition dates, and accuracies are plotted along a timeline in

Table 6.3.

Data source	Source date	Accuracy (m)
Cartographic map	1947	1000-2000*
DISP	09/1963	200
Aerial photography	01/1966	500*
ADD	1968	260**
LANDSAT MSS	01/1973	100*
DISP	12/1975	25
AVHRR	01/1980	1000*
ERS-1	1992	50*
ERS-1	11/1995	50*
ERS-1	01/1996	50*
RADARSAT-1	09/1997	25
ERS-1	05/2000	50*
RADARSAT-1	09/2000	25
ASTER	12/2003	15

Table 6.3 Information of source data for Pine Island Glacier (* from Rignot (2002) and ** from ADD Consortium, 2000)

Rignot's map (Figure 6.6) was scanned using a portable scanner at a resolution of 600 dots per inch (dpi). A linear transformation (e.g., affine transformation) function was used to georeference the scanned map using 12 well-distributed longitude-latitude points in the map, and then our five estimates in Figure 6.5 were overlaid on the georeferenced map.

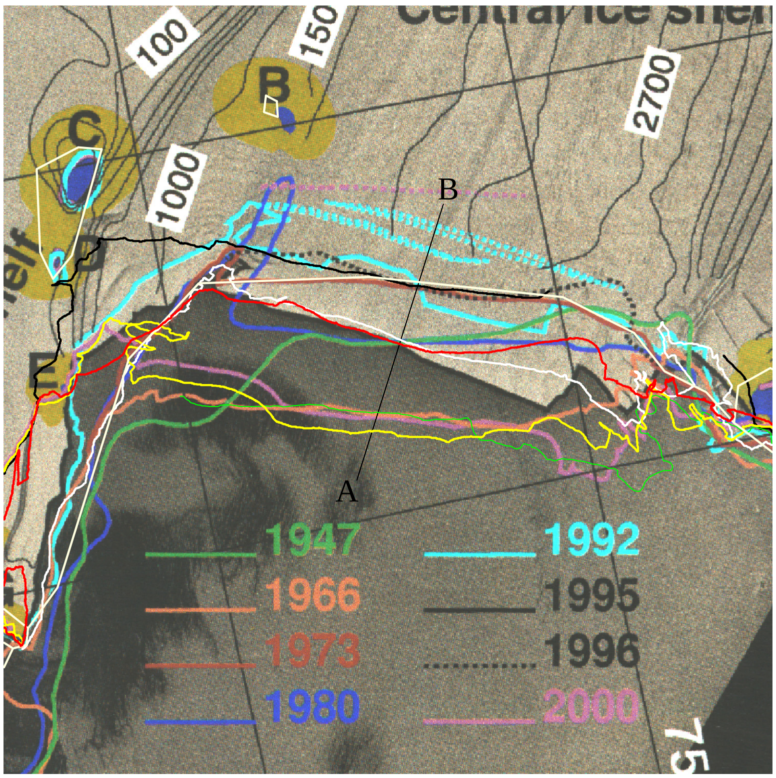

Figure 6.6 Fourteen glacier terminus positions of Pine Island Glacier between 1947 and 2003 (Rignot, 2002): September 1963 (bright green), 1968 (bright yellow), December 1975 (white), September 1997 (red), November 2000 (yellow), and September 2003 (black) ice front margins are added on Rignot's map (2002)

The glacier terminus positions were measured along the line $\overline{AB}$ in Figure 6.6, and changes in the positions were calculated in reference to 1947 (Table 6.4). Over these 56-years of observations, we found that ice terminus positions along the line $\overline{AB}$ have oscillated between -4.6-km and 6.6-km in reference to 1947 mainly due to large calving events occurred between 1947 and 2003, and the glacier has calved with approximately 4 to18-km of the glacier length in direction of the glacier velocity. In addition, the glacier terminus position was at its most advanced stage in the RADARSAT-1 SAR image of September, 2000 before a 18-km iceberg calved in November, 2001 (http://photojournal.jpl.nasa.gov/catalog/PIA03431) and was at its most retreated stage in the SCAR ADD data of 1968 after the similar size of iceberg calved between 1966 and 1968.

Year	x-position (m)	y-position (m)	Change (m)
1947	-1616894	-331511	Reference
09/1963	-1618467	-336506	5236.862
01/1966	-1618497	-336588	5324.052
1968	-1615501	-327108	-4618.101
01/1973	-1615642	-327538	-4165.601
12/1975	-1616827	-331292	-229.019
01/1980	-1616861	-331429	-88.391
1992	-1615561	-327307	-4410.272
11/1995	-1616951	-331714	210.850
01/1996	-1615626	-327515	-4192.354
09/1997	-1616905	-331571	61.000
05/2000	-1618559	-336847	5589.733
09/2000	-1618876	-337853	6644.493
12/2003	-1615600	-327417	-4293.631

Table 6.4 Pine Island Glacier terminus changes along the line $\overline{AB}$ in Figure 6.4

Figure 6.7 shows changes in the glacier terminus position of the Pine Island Glacier between 1947 and present. Using a weighted, linear least-squares adjustment in Equation (3.11), a retreat rate of the glacier terminus position was estimated of approximately 10 ± 65 m/yr. Each terminus change was calculated in reference to the 1947 terminus position, and its error was then inversely weighted during the linear least-squares adjustment. For example, an error of $\sqrt{\sigma^2{}_{1963} + \sigma^2{}_{1975}}$ was estimated for the change between 1963 and 1975 and then inversely weighted during the linear least-squares adjustment.

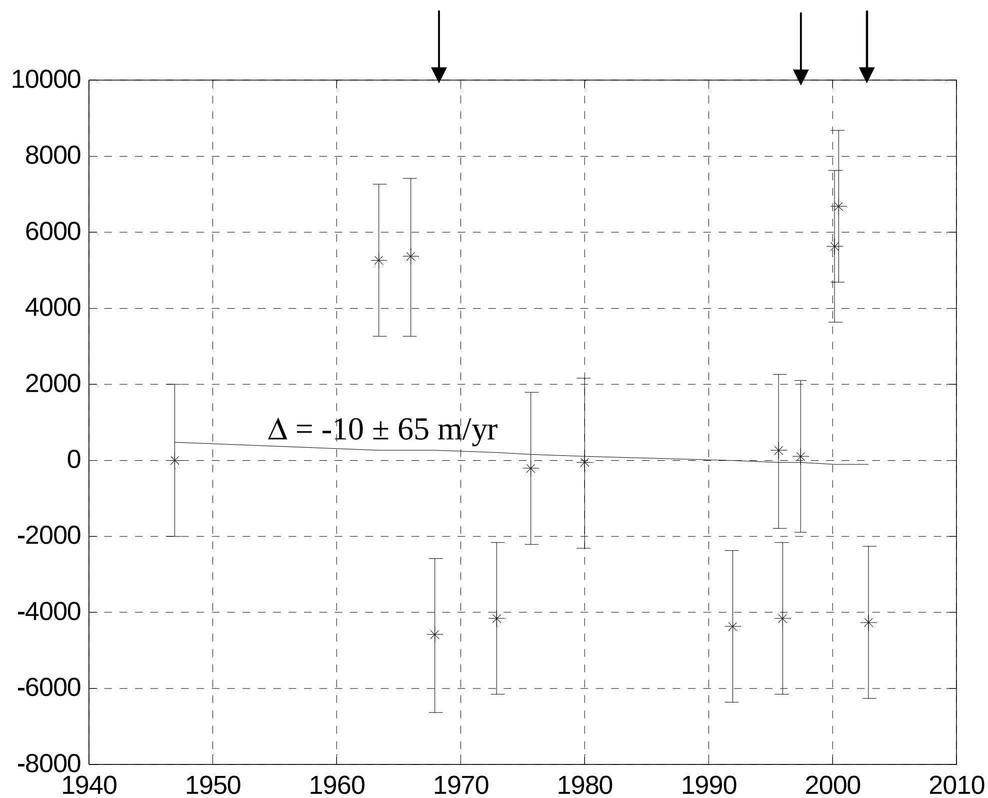

Figure 6.7 An estimated retreat rate of the Pine Island Glacier terminus position between1947 and present: the trend was calculated using an weighted, linear least-squares adjustment; and down arrows (↓) indicate the calving events observed between 1966 and 1968, in January 1995 (Rignot, 2002), and in November 2003 (http://photojournal.jpl.nasa.gov/catalog/PIA03431)

The glacier terminus position of the Pine Island Glacier has changed with a retreat rate of approximately -10 ± 65 m/yr from 1947 to present. This numerically supports previous results (Lucchitta et al., 1995; Jenkins et al., 1997; Rignot, 1998; Bindschadler and Rignot, 2001; Vaughan et al., 2001; and Reginot, 2002), which suggested that there was no discernible change in the mean position of the glacier terminus over the last three or four decades.

A glacier terminus position is approximately determined on a balance between the glacier velocity and calving rate at the glacier terminus position. This can be expressed as $M = V - C$, where M is the retreat or advance rate and V and C are the velocity and calving rate, respectively. Using a retreat rate of -10 ± 65 m/yr and a flow speed of 2.5 ± 0.4 km/yr at the terminus (Crabtree and Doake, 1982; Lucchitta et al., 1995; and Rignot, 1998) between 1973 and 1996, the calving rate of approximately 2.51 ± 0.4 km/yr was obtained.

We note that ice shelves in Antarctica catastrophically retreat (e.g., Larsen Ice Shelf in Figure 6.2). That is, ice shelves, which appear to have stable terminus positions, can disintegrate over a period of days to weeks. While other scientists have observed large changes in thinning rate, increasing velocity, and retreating grounding line of the Pine Island Glacier, we observed little change in the glacier terminus positions. This leads us to speculate that the glacier terminus change is not always a good indicator of the glacier health. Moreover we cannot explain how the calving rate of the Pine Island Glacier can change almost synchronously with the glacier velocity, so that the change of the glacier terminus position is small.

CHAPTER 7

CONCLUSION

The individual DISP photographs are important resources for measuring the geometry of the coastline of Antarctica. By using the state-of-art digitizing technology, bundle block triangulation based on tie points and control points derived from the RADARSAT-1 SAR image mosaic, and OSU Antarctic DEM, we accurately assembled the individual images into a map quality mosaic of Antarctica as it appeared in 1963. The positional accuracy depends upon the quality of source data used for orthorectifying the DISP photographs and the number and distribution of tie and control points selected from the source data. The standard deviation of the resulting image block was within two-pixel accuracy (200-m). This satisfied our mapping requirement on detecting Antarctic coastal change. The new map is another important benchmark for gauging the response of the Antarctic coastline to changing climate.

The development of image segmentation algorithms based on an adaptive Bayesian approach is the second theme of this dissertation. The adaptive Bayesian framework to image segmentation developed in Chapter 4 relied upon the use of the prior and conditional probability density functions. The Markov random field (MRF) model was successfully replaced by the fuzzy c-means clustering (FCM) technique, which avoids the difficulty in estimating the conditional probability $\Pr(y \mid x)$ of the observed intensity values y given the labels x. Initial values derived from the Gaussian mixture model (GMM) made another contribution to the Bayesian framework, resulting in more reliable results than randomly chosen initial values. A simple synthetic image has been used for verifying the algorithm. Results have been presented that demonstrate the effectiveness of the algorithm in segmenting the synthetic image, resulting in more than 99.8% accuracy when noise characteristics are correctly modeled.

The third theme of this dissertation is to automatically extract the entire coastline from the 1963 DISP image mosaic created in Chapter 3, so that the derived, historical coastline can be compared with other time series data over continental scales. Automated coastline extraction software developed in Chapter 4 was applied to the entire DISP image mosaic, but more than 40 % significant cloud cover and very low contrast of the historical imagery made it difficult to correctly extract the coastline everywhere. In these cases, manual editing was carried out based on intermediate image processing and visual inspection. The quality of the extracted coastline must be known when analyzing changes in comparison with other time series data. By visual checking the source image, the accuracy of the extracted coastline was estimated to be less than one pixel, noting that the extracted coastline accuracy may be larger than three pixels where light cloud cover exists. The accuracy of the extracted coastline is also influenced by the geo-referencing accuracy of the source image; consequently we estimated the overall accuracy to be approximately 200 to 500-m using the error propagation raw.

Through a geographic information system (GIS), the derived, refined 1963 DISP data were integrated with earlier and later data to assess continental scale changes in ice margin advance or retreat. Calculating the area of the major Antarctic ice shelves between 1963 and 1997, we found that net loss was approximately 0.8 % and that ice shelves retreated mostly between DISP and ADD. In addition, over the 56-years observations on Pine Island Glacier, we found that the retreat rate since 1947 has been approximately -10 ± 65 m/yr. We also note that ice shelves in the Antarctica catastrophically retreated. While other scientists have observed large changes in thinning rate, increasing velocity, and retreating grounding line of the Pine Island Glacier, we observed little change in the glacier terminus positions. This leads us to speculate that the glacier terminus change is not always a good indicator of the glacier health. Moreover we cannot explain how the calving rate of the Pine Island Glacier can change almost synchronously with the glacier velocity, so that the change of the glacier terminus position is small.

BIBLIOGRAPHY

Abrams, M. and S. Hook, 2002, ASTER user handbook version 2, Jet Propulsion Laboratory, Pasadena, 136 pp.

ADD Consortium, 2000, Antarctic digital database version 3.0 database, manual and bibliography, Scientific Committee on Antarctic Research (SCAR), Cambridge, Manual and bibliography, 93 pp.

Altmaier, A. and C. Kany, 2002, Digital surface model generation from CORONA satellite images, ISPRS Journal of Photogrammetry & Remote Sensing, Vol. 56, pp. 221-235.

Barker, S. A., 1998, Image segmentation using Markov random field models, A Ph.D. Dissertation, University of Cambridge, Cambridge, 156 pp.

Bertro, M., T.A. Poggio, and V. Torre, 1988, Ill-posed problems in early vision, Proceedings of the IEEE, Vol. 78, No. 8, pp. 869-889.

Besag, J., 1974, Spatial interaction and the statistical analysis of lattice systems, Journal of the Royal Statistical Society, Series B, Vol. 36, No. 2, pp. 192-236.

Besag, J., 1986, On the statistical analysis of dirty pictures, Journal of the Royal Statistical Society, Series B, Vol. 48, No. 3, pp. 259-302.

Bezdek, J., R. Ehrlich, and W. Full, 1984, FCM: The fuzzy c-means clustering algorithm, Computers & Geosciences, Vol. 10, No. 2-3, pp. 191-203.

Binschadler, R.A. and E. Rignot, 2001, Crack! in the polar night, EOS, Vol. 82, No. 43, pp. 497–505.

Binschadler, R.A. and W. Seider, 1998, Declassified intelligence satellite photography (DISP) coverage of Antarctica, NASA Technical Memorandum-1998-206879, Greenbelt, Maryland, 37 pp.

Cannon, R.L., J.V. Dave, J.C. Bezdek, and M.M. Trivedi, 1986, Segmentation of a Thematic Mapper image using the fuzzy c-means clustering algorithm, IEEE Transactions on Geoscience and Remote Sensing, Vol. GE-24, pp. 400-408.

Chellappa, R., 1985, Two-dimensional discrete Gaussian Markov random filed models for image processing, edited by L.N. Kanal and A. Rosenfield, Progress in Pattern Recognition, Vol. 2, pp. 79-112.

Chow, C.K. and T. Kaneko, 1972, Automatic boundary detection of the left ventricle from cineangiograms, Computers and Biomedical Research, Vol. 5, pp. 388-410.

Dempster, A.P., N.M. Laird, and D.B. Bubin, 1977, Maximum likelihood from incomplete data via EM algorithm, Journal of Royal Statistical Society, Series B, Vol. 39, No. 1, pp. 1-38.

Derin, H. and H. Elliott, 1987, Modeling and segmentation of noisy and textured images using Gibbs random fields, IEEE Transaction on Pattern Analysis and Machine Intelligence, Vol. PAMI-9, No. 1, pp. 39-55.

Derin, H. and W.S. Cole, 1986, Segmentation of textured images using Gibbs random fields, Computer visions, Graphs, and Image Processing, Vol. 35, pp. 72-98.

Dubes, R.C. and A.K. Jain, 1989, Random field models in image analysis, Journal of Applied Statistics, Vol. 16, No. 2, pp. 131-164.

Froehlich, G.K., J.F. Walkup, and T.F. Krile, 1981, Estimation in signal-dependent film-grain noise, Applied Optics, Vol. 20, pp. 3619-3626.

Geman, S. and D. Geman, 1984, Stochastic relaxation, Gibbs distributions, and the Bayesian restoration of images, IEEE Transaction on Pattern Analysis and Machine Intelligence, Vol. PAMI-6, No. 6, pp. 721-741.

Geman, S. and G. Reynolds, 1992, Constrained restoration and the recovery of discontinuities, IEEE Transaction on Pattern Analysis and Machine Intelligence, Vol. 43, No. 3, pp. 767-783.

Haverkamp, R.M., L.K. Soh, and C. Tsatsoulis, 1995, A comprehensive, automated approach to determining sea ice thickness from SAR data, IEEE Transaction on Geoscience and Remote Sensing, Vol. 33, No. 1, pp. 46-57.

Jenkins, A., D.G. Vaughan, S.S. Jacobs, H.H. Hellmer, and J.R. Keys, 1997, Glaciological and oceanographic evidence of high melt rates beneath Pine Island Glacier, West Antarctica, Journal of Glaciology, Vol. 43, No. 143, pp. 114-121.

Jezek, K.C., 1999, Glaciological properties of the Antarctic Ice Sheet from RADARSAT-1 synthetic aperture radar imagery, Annals of Glaciology, Vol. 29, pp. 286-290.

Jezek, K.C., K. Farness, R. Carande, X. Wu, and N. Labelle-Hamer, 2003, RADARSAT-1 synthetic aperture radar observations of Antarctica: Modified Antarctic Mapping Mission, 2000, Radio Science, Vol. 38, No. 4, pp. MAR32-1-MAR32-7.

Kim, K, K.C. Jezek, and H. Sohn, 2001, Ice shelf advance and retreat rates along the coast of Queen Maud Land, Antarctica, Journal of Geophysical Research, Vol. 106, No. C4, pp. 7097-7106.

Koch, K.R., 1988, Parameter estimation and hypothesis testing in linear models, Springer-Verlag, Telos, 333 pp.

Kraus, K., 1993, Photogrammetry, volum1: fundamentals and standard process (4th Ed), Fred. Dümmlers Verlag, Bonn, Germany, 397 pp.

Kuan, D.T., A.A. Sawchuk, T.C. Strand, and P. Chavel, 1985, Adaptive noise smoothing filter for images with signal-dependent noise, IEEE Transactions on Pattern Analysis and Machine Intelligence, Vol. PAMI-7, pp. 165-177.

Lakshmanan, S. and H. Derin, 1989, Simultaneous parameter estimation and segmentation of Gibbs random fields using simulated annealing, IEEE Transactions on Pattern Analysis and Machine Intelligence, Vol. 11, pp. 799-813.

Lee, J.S., 1980, Digital image enhancement and noise filtering by use of local statistics, IEEE Transaction on Pattern Analysis and Machine Intelligence, Vol. PAMI-2, pp. 165-168.

Li, S.Z, 1995, Markov random field modeling in computer vision, Springer-Verlag, Tokyo, 263 pp.

Light, D.L., 1993, The national aerial photography program as a geographic information system resource, Photogrammetric Engineering and Remote Sensing, Vol. 59, No. 1, pp. 61-65.

Liu, H, K.C. Jezek, and B. Li, 1999, Development of an Antarctic digital elevation model by integrating cartographic and remotely sensed data: A geographic information system based approach, Journal of Geophysical Research, Vol. 104, No. B10, pp. 23,199-23,213.

Liu, H. and K.C. Jezek, 2003, Automated extraction of coastline from satellite imagery by integrating Canny edge detection and locally adaptive thresholding methods, International Journal of Remote Sensing, Vol. 24, No. 00, pp. 1-22.

Lucchitta, B.K., C.E. Rosannova, and K.F. Mullins, 1995, Velocities of Pine Island Glacier, West Antarctica, from ERS-1 SAR images, Annals of Glaciology, Vol. 21, pp. 277-283.

Manjunath, B.S. and R. Chellappa, 1991, Unsupervised texture segmentation using Markov random field models, IEEE Transaction on Pattern Analysis and Machine Intelligence, Vol. 13, No. 5, pp. 478-482.

Marroquin, J., S. Mitter, and T. Poggio, 1987, Probabilistic solution of ill-posed problems in computational vision, Journal of American Statistical Association, Vol. 82, No. 397, pp. 76-89.

McDonald, R.A., 1995, Corona: Success for space reconnaissance, A look into the cold war and a revolution in intelligence, Photogrammetric Engineering & Remote Sensing, Vol. 61, No. 6, pp. 689-720.

McDonald, R.A., 1997, Corona, Argon, and Lanyard: A revolution for US overhead reconnaissance, CORONA: Between the Sun and the Earth, The American Society for Photogrammetry and Remote Sensing, Bethesda, pp.61-74.

Mercer, J.H., 1978, West Antarctic ice sheet and CO_2 greenhouse effect: a threat of disaster, Nature, Vol. 271, No. 5643, pp. 321-325.

Naderi, F. and A.A. Sawchuk, 1978, Estimation of images degraded by film-grain noise, Applied Optics, Vol. 17, pp. 1228-1237.

Noltimier, K.F., K.C. Jezek, H. Sohn, B. Li, H. Li, F. Baumgartner, V. Kaupp, J.C. Curlander, B. Wilson, and R. Onstott, 1999, RADARSAT Antarctic mapping project – mosaic construction, in IGASS'99 Proceedings: Remote Sensing of the System Earth – A challenge for the 21st Century, IEEE, New York, pp. 2349-2351.

Peebles, C., 1997, The Corona project: America's first spy satellites, Naval Institute Press, Annapolis, 351 pp.

Pitas, I. and A.N. Venetsanopoulos, 1992, Order statistics in digital image processing, Proceedings of IEEE, Vol. 80, pp. 1893-1923.

Poggio, T., V. Torre, and C. Koch, 1985, Computational vision and regularization theory, Nature, Vol. 343, pp. 263-266.

Rangayyan, R.M., M. Ciuc, and F. Faghih, 1998, Adaptive-neighborhood filtering of images corrupted by signal-dependent noise, Applied Optics, Vol. 37, No. 20, pp. 4477-4487.

Rencz, A.N. and R.A. Ryerson (ed), 1998, Manual of remote sensing, 3rd Ed, volume 3: remote sensing for the Earth science, John Wiley & Sons Inc., New York, 728 pp.

Rignot, E., 1998, Fast recession of a west Antarctic glacier, Science, Vol. 281, pp. 549-551.

Rignot, E., 2002, Ice-shelf changes in Pine Island Bay, Antarctica, 1947-2000, Journal of Glaciology, Vol. 48, No. 161, pp. 247-256.

Ruffner, K.C., 1995, CORONA: America's first satellite program, Washington, DC: Center for the Study of Intelligence, Central Intelligence Agency.

Schaffrin, B., 1998, GS 762: course packet, The Ohio State University, Columbus.

Shepherd, A., D.J. Wingham, J.A.D. Mansley, and H.F.J. Corr, 2001, Inland thinning of Pine Island Glacier, West Antarctica, Science, Vol. 291, pp. 862-864.

Shin, S., 2003, Rigorous model of panoramic cameras, A Ph.D. Dissertation, The Ohio State University, Columbus, 120 pp.

Slama, C.C, C. Theurer, and S.W. Henriksen (ed), 1980, Manual of photogrammetry, 4th Ed, American Society of Photogrammetry, Falls Church, 1056 pp.

Sohn, H., 1996, Boundary detection using multispectral imagery: application to ice sheet margin detection, A Ph.D Disseration, The Ohio State University, Columbus, 186 pp.

Swithinbank, C. and B.K. Lucchitta, 1986, Multispectral digital image mapping of Antarctic ice features, Annals of Glaciology, Vol. 8, pp. 159-163.

Swithinbank, C., 1973, Higher resolution satellite pictures, Polar Record, Vol. 16, No. 104, pp. 739-751.

Tolstikov, Y.I. (ed), 1966, Atlas Antarctiki, Volume I, Main Adminstration of Geodesy and Cartography of the Ministry of Geology USSR, Moscow, 255 pp.

Tso, B. and P.M. Mather, 2001, Classification methods for remotely sensed data, Tayleor & Francis, London and New York, 332 pp.

Vaughan, D.G., A.M. Smith, H.F.J. Corr, A. Jenkins, C.R. Bentley, M.D. Stenoien, S.S. Jacobs, E. Rignot, and B.K. Lucchitta, 2001, A review of Pine Island Glacier, West Antarctica: Hypothesis of instability vs. observations of change, The Antarctic Research Series published by the American Geophysical Union, Washington, D.C., pp. 237-256.

Vaughan, D.G. and C.S.M. Doake, Recent atmospheric warming and retreat of ice shelves on the Antarctic Peninsula, Nature, Vol. 379, pp. 328-331.

Wheelon, A.D., 1997, Corona: The first reconnaissance satellites, Physics Today, February, pp. 24-30.

Williams, Jr., R.W., J.G. Ferrigno, C. Swithinbank, B.K. Lucchitta, and B.A. Seekins, 1995, Coastal-change and glaciological maps of Antarctica, Annals of Glaciology, Vol. 21, pp. 284-290.

Wingham, D.J., A.J. Ridout, R. Scharroo, R.J. Arthern, and C.K. Shum, 1998, Antarctic elevation change from 1992 to 1996, Science, Vol. 282, pp. 456-458.

Zhou, G., K.C. Jezek, W. Wright, and J. Granger, 2002, Orthorectificatoin of 1960s satellite photographs covering Greenland, IEEE Transaction on Geoscience and Remote Sensing, Vol. 40, No. 6, pp. 1247-1259.

APPENDIX A

GROUND CONTROL POINTS OF ANTARCTICA

Table A shows the x and y coordinates of the entire ground control points (GCP), which were depicted in Figure 3.10, selected from 1997 RADARSAT-1 SAR image mosaic (100-m pixel resolution), and used for bundle block triangulations in Chapter 3. The coordinates are in a polar stereographic projection with a standard parallel of 71° S on the WGS 84 ellipsoid.

GCPs	x (meters)	y (meters)
001	891012.5	1786362.5
002	965537.5	1919387.5
003	1006275.0	1651925
004	675612.5	1830637.5
005	802612.5	2015162.5
006	-9362.5	1964237.5
007	236212.5	1977637.5
008	435137.5	2039737.5
009	446125.0	1951875
010	279137.5	2161812.5
011	214962.5	2159762.5
012	401925.0	2156325
013	714712.5	2047712.5
014	825306.25	1785706.2
015	489837.5	2134337.5
016	432662.5	1919112.5

Continued

Table A Ground control points of Antarctica

017	503675.0	1905825.0
018	337425.0	1946525.0
019	675637.5	1830712.5
020	594725.0	2131675.0
021	1413762.5	1724362.5
022	1516237.5	1778312.5
023	1813812.5	1599712.5
024	1829262.5	1691537.5
025	1824112.5	1697087.5
026	1372212.5	1740787.5
027	1291212.5	1956212.5
028	970137.5	1960212.5
029	2294125.0	859525.0
030	2376050.0	430950.0
031	2185562.5	987512.5
032	1811062.5	482187.5
033	1960637.5	907087.5
034	1811362.5	779712.5
035	1581671.1	877022.5
036	2331862.5	-1107787.5
037	2069412.5	-1545287.5
038	2156487.5	-1342962.5
039	2230475.0	-1176475.0
040	2397875.0	-825425.0
041	2490737.5	-741412.5
042	2354800.0	-1079300.0
043	1477837.5	-2055212.5
044	1695362.5	-1946687.5
045	1311337.5	-2006712.5
046	1002525.0	-2122125.0
047	963409.8	-2097500.2
048	850987.5	-2084537.5
049	1190712.5	-2049787.5
050	1190712.5	-2049787.5
051	1713412.5	-1936337.5
052	1879475.0	-1824475.0
053	1921837.5	-1791937.5
054	1056992.2	-2139769.2
055	965278.5	-2104638.4
056	844012.5	-2118762.5
057	1160212.5	-2076412.5
058	1348801.7	-2039833.4
059	1190512.5	-2050937.5

Continued

Table A Ground control points of Antarctica

060	1039025.0	-2084925.0
061	597137.5	-2017862.5
062	381712.5	-2005212.5
063	559175	-1847575.0
064	397062.5	-1803562.5
065	516166.7	-1485921.8
066	424212.5	-1797962.5
067	495875.0	-1648425.0
068	359387.5	-1994487.5
069	570475.0	-1453025.0
070	472587.5	-1319912.5
071	471025.0	-1079275.0
072	303175.0	-1289825.0
073	344225.0	-736325.0
074	153825.0	-718275.0
075	316237.5	-905412.5
076	432275.5	-962056.9
077	450325.0	-1168025.0
079	288063.7	-1267041.3
080	256175.0	-1344875.0
081	-77937.5	-783937.5
082	276275.0	-764225.0
083	157825.0	-747075.0
084	207750.0	-790375.0
085	273800.0	-663100.0
086	24837.5	-468412.5
087	204112.5	-588637.0
088	352212.5	-780262.5
089	-337762.5	-370312.5
090	-516587.5	-253337.5
091	-452175	-142175.0
092	-109162.5	-351737.5
093	-102350.0	-535400.0
094	-210587.5	-422787.5
095	-77962.5	-783937.5
096	43637.5	-455312.5
097	-375487.5	-278437.5
098	-101871.6	-768877.1
099	164412.5	-645412.5
100	-289525.0	-678475.0
101	-90362.5	-568862.5
102	-810461.7	-1095005.4
103	-614182.3	-1232421.6

Continued

Table A Ground control points of Antarctica

104	-880984.0	-1311240.7
105	-692839.9	-1122133.6
106	-799743.7	-1251307.2
107	-323127.1	-1156259.1
108	-394293.5	-1035407.9
109	-305625.0	-506925.0
110	-289675.0	-678475.0
111	-433500.0	-862400.0
112	-223487.5	2136587.5
113	-115300.0	1888700.0
114	-438387.5	1785087.5
115	-6287.5	1959462.5
116	97962.5	1984487.5
117	-103087.5	2146012.0
118	96300.0	2133400.0
119	-704973.5	1323109.1
120	-736461.1	1226877.5
121	-766086.1	1082102.5
122	-552961.1	353527.5
123	-542636.1	611627.5
124	-221448.6	563140.1
125	-500161.1	918952.5
126	-568036.1	1037527.5
127	-732836.1	1250752.5
128	-767961.1	1115302.5
129	-966986.1	915377.5
130	-464950.0	970350.0
131	-800387.5	850387.5
132	-548123.6	1093215.0
133	-929225.0	463425.0
134	-809300.0	582700.0
135	-661800.0	569300.0
136	-618625.0	430225.0
137	-482860.0	228096.0
138	-542333.0	611623.0
139	-532314.0	376865.0
140	-442127.0	173315.0
141	-1435162.5	552787.5
142	-1460837.5	689262.5
143	-1410112.5	520537.5
144	-1340775.0	218725.0
145	-1138125.0	409475.0
146	-855825.0	634475.0

Continued

Table A Ground control points of Antarctica

147	-1004575.0	861125.0
148	-793075.0	597275.0
149	-908275.0	437125.0
150	-929225.0	463425.0
151	-809300.0	582700.0
152	-661800.0	569300.0
153	-661800.0	569300.0
154	-618625.0	430225.0
155	-482860.0	228096.0
156	-542333.0	611623.0
157	-532314.0	376865.0
158	-442127.0	173315.0
159	-855825.0	634475.0
160	-1004575.0	861125.0
161	-793075.0	597275.0
162	-908275.0	437125.0
163	-1432007.0	559548.0
164	-1470270.0	688593.0
165	-1138125.0	409475.0
166	-1340775.0	218725.0
167	-2432022.9	1694241.5
168	-2382427.7	1530406.2
169	-2497046.4	1498500.0
170	-2493346.4	1598800.0
171	-1757722.9	960516.5
172	-1578627.7	861193.7
173	-1665346.4	931125.0
174	-1563996.4	796400.0
175	-1522479.1	793935.2
176	-1006921.4	870175.0
177	-2499512.5	1478012.5
178	-2199193.7	1010793.7
179	-2427262.5	1086062.5
180	-2406387.5	1301737.5
181	-2306787.5	1303412.5
182	-2374887.5	976787.5
183	-2423112.5	1088612.5
184	-2319362.5	1177987.5
185	-2278512.5	894587.5
186	-2176787.5	780912.5
187	-1828387.5	982037.5
188	-2031860.4	1011229.0
189	-2191212.5	759737.5

Continued

Table A Ground control points of Antarctica

190	-2205912.5	936462.5
191	-1970462.5	823312.5
192	-1892237.5	659462.5
193	-1745612.5	569537.5
194	1174685.3	1641189.5
195	1371606.7	1753607.2
196	1281865.7	1961027.1
197	980281.1	1951118.0
198	928068.4	1758745.4
199	2171001.6	1532398.4
200	-1970592.3	243525.3
201	-1909777.5	-96701.0
202	-1939790.0	-41730.8
203	-1869971.5	120336.6
204	-1970258.5	-244046.4
205	-1955321.5	-197051.5
206	-1967959.2	-276631.9
207	-1949876.3	-365401.2
208	-1630440.5	-280507.9
209	-1573509.1	-585690.9
210	-1392275.6	-667158.4
211	-1748167.3	-402824.7
212	-1751911.8	-352963.1
213	-1588779.1	-349367.0
214	-1783386.5	-462213.8
215	-1509801.3	-637069.5
216	-328175.1	1623419.7
217	-631620.2	1641827.1
218	-315636.0	1648848.9

Table A Ground control points of Antarctica

APPENDIX B

PARTIAL DERIVATIVES OF COLLINEARITY EQUATIONS

The collinearity equations in Equation (3.5) can be rewritten by:

$$x = -f\,\frac{N_x}{D} = f\,(X_c, Y_c, Z_c, \omega, \varphi, \kappa, X_p, Y_p, Z_p)$$
$$y = -f\,\frac{N_y}{D} = f\,(X_c, Y_c, Z_c, \omega, \varphi, \kappa, X_p, Y_p, Z_p)$$

where,

$$\begin{aligned} N_x &= r_{11}(X_p - X_c) + r_{21}(Y_p - Y_c) + r_{31}(Z_p - Z_c) \\ N_y &= r_{12}(X_p - X_c) + r_{22}(Y_p - Y_c) + r_{23}(Z_p - Z_c) \\ D &= r_{13}(X_p - X_c) + r_{23}(Y_p - Y_c) + r_{33}(Z_p - Z_c) \end{aligned}$$

The partial derivatives of x and y with respect to the unknown parameters are then as follows:

$$\frac{\partial x}{\partial X_c} = -\frac{f}{D^2}\left(r_{13}N_x - r_{11}D\right) \qquad \frac{\partial y}{\partial X_c} = -\frac{f}{D^2}\left(r_{13}N_y - r_{12}D\right)$$

$$\frac{\partial x}{\partial Y_c} = -\frac{f}{D^2}\left(r_{23}N_x - r_{21}D\right) \qquad \frac{\partial y}{\partial Y_c} = -\frac{f}{D^2}\left(r_{23}N_y - r_{22}D\right)$$

$$\frac{\partial x}{\partial Z_c} = -\frac{f}{D^2}\left(r_{33}N_x - r_{31}D\right) \qquad \frac{\partial y}{\partial Z_c} = -\frac{f}{D^2}\left(r_{33}N_y - r_{32}D\right)$$

$$\frac{\partial x}{\partial \omega} = -\frac{f}{D}\left\{\left[(Y_p - Y_c)r_{33} - (Z_p - Z_c)r_{23}\right]\frac{N_x}{D} - (Y_p - Y_c)r_{31} + (Z_p - Z_c)r_{21}\right\}$$

$$\frac{\partial y}{\partial \omega} = -\frac{f}{D}\left\{\left[(Y_p - Y_c)r_{33} - (Z_p - Z_c)r_{23}\right]\frac{N_y}{D} - (Y_p - Y_c)r_{32} + (Z_p - Z_c)r_{22}\right\}$$

$$\frac{\partial x}{\partial \varphi} = \frac{f}{D}\left\{\left[N_x \cos\kappa - N_y \sin\kappa\right]\frac{N_x}{D} + D\cos\kappa\right\}$$

$$\frac{\partial y}{\partial \varphi} = \frac{f}{D}\left\{\left[N_x \cos\kappa - N_y \sin\kappa\right]\frac{N_y}{D} + D\sin\kappa\right\}$$

$$\frac{\partial x}{\partial \kappa} = -\frac{f}{D}N_y \qquad \frac{\partial y}{\partial \kappa} = \frac{f}{D}N_x$$

$$\frac{\partial x}{\partial X_p} = \frac{f}{D^2}\left(r_{13}N_x - r_{11}D\right) \qquad \frac{\partial y}{\partial X_p} = \frac{f}{D^2}\left(r_{13}N_y - r_{12}D\right)$$

$$\frac{\partial x}{\partial Y_p} = \frac{f}{D^2}\left(r_{23}N_x - r_{21}D\right) \qquad \frac{\partial y}{\partial Y_p} = \frac{f}{D^2}\left(r_{23}N_y - r_{22}D\right)$$

$$\frac{\partial x}{\partial Z_p} = \frac{f}{D^2}\left(r_{33}N_x - r_{31}D\right) \qquad \frac{\partial y}{\partial Z_p} = \frac{f}{D^2}\left(r_{33}N_y - r_{32}D\right)$$

Using these partial derivatives, Equations (3.5) can be expressed as the linearized observation equations for the least squares adjustment.

$$
\begin{aligned}
x = x^o &+ \left(\frac{\partial x}{\partial X_c}\right)^o dX_c + \left(\frac{\partial x}{\partial Y_c}\right)^o dY_c + \left(\frac{\partial x}{\partial Z_c}\right)^o dZ_c \\
&+ \left(\frac{\partial x}{\partial \omega}\right)^o d\omega + \left(\frac{\partial x}{\partial \varphi}\right)^o d\varphi + \left(\frac{\partial x}{\partial \kappa}\right)^o d\varphi \\
&+ \left(\frac{\partial x}{\partial X_p}\right)^o dX_p + \left(\frac{\partial x}{\partial Y_p}\right)^o dY_p + \left(\frac{\partial x}{\partial Z_p}\right)^o dZ_p
\end{aligned}
$$

$y = \text{similar}$

where,

(x, y) are the observed image coordinates;

$$x^o = f(X_c{}^o, Y_c{}^o, Z_c{}^o, \omega^o, \varphi^o, \kappa^o, X_p{}^o, Y_p{}^o, Z_p{}^o)$$
$$y^o = f(X_c{}^o, Y_c{}^o, Z_c{}^o, \omega^o, \varphi^o, \kappa^o, X_p{}^o, Y_p{}^o, Z_p{}^o)$$

$dX_c = (X_c - X_c{}^o)$, etc.